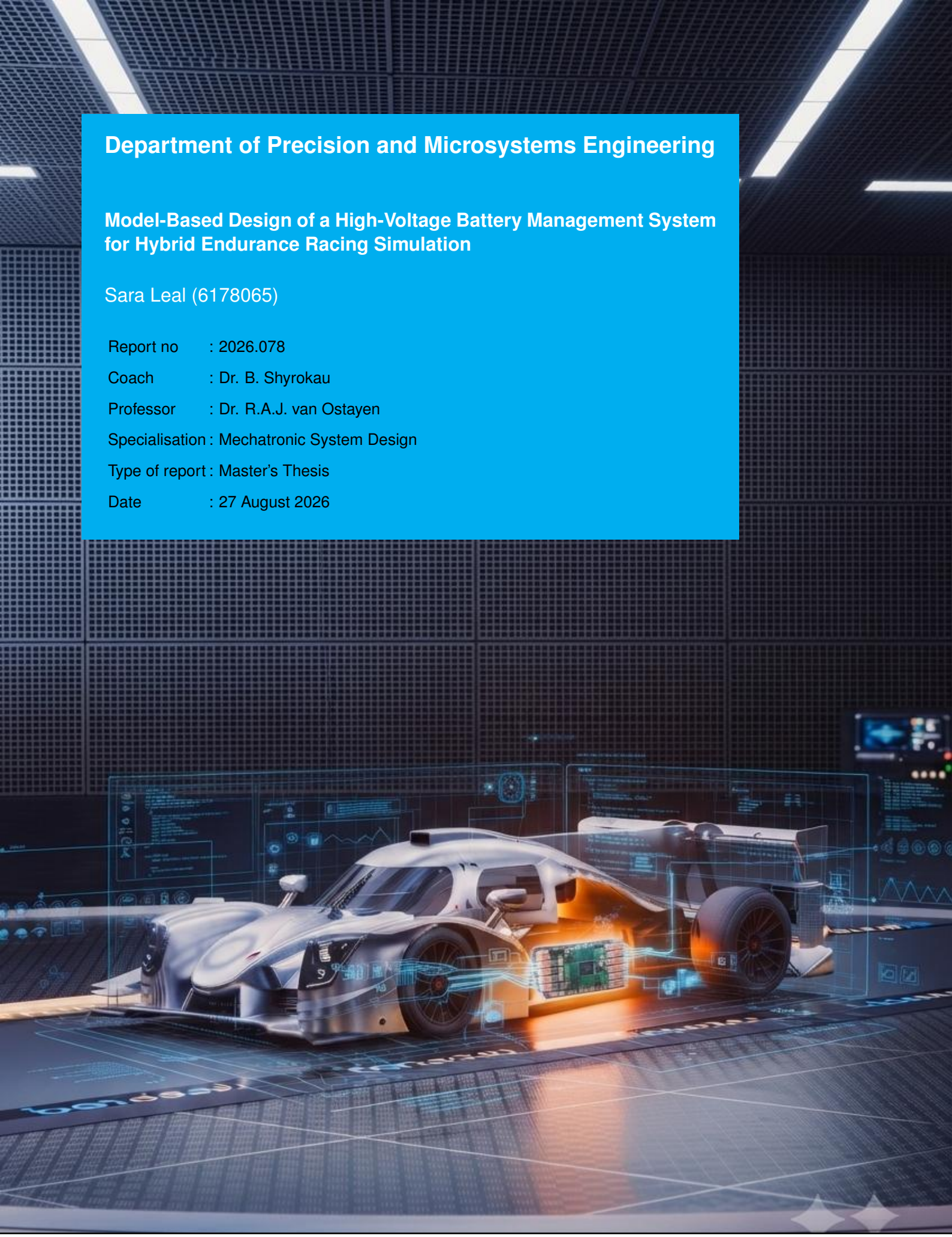
Department of Precision and Microsystems Engineering

Model-Based Design of a High-Voltage Battery Management System for Hybrid Endurance Racing Simulation

Sara Leal (6178065)

Report no	: 2026.078
Coach	: Dr. B. Shyrokau
Professor	: Dr. R.A.J. van Ostayen
Specialisation	: Mechatronic System Design
Type of report	: Master's Thesis
Date	: 27 August 2026



TU Delft Delft University of Technology

Cover image generated with Gemini AI Tool

Abstract

Hybrid endurance racing powertrains, such as those deployed in Le Mans Daytona Hybrid (LMDh) applications, operate under severe electrical and thermal stresses characterised by aggressive high-power transients and repetitive drive cycles. Since much of the available knowledge surrounding these complex system dynamics remains proprietary, this study develops a fully coupled, state-dependent high-voltage (HV) battery power supply model and a coordinated model-based battery management architecture. An advanced 2nd Order Equivalent Circuit Model (ECM) is formulated in MATLAB/Simulink to capture the nonlinear electrochemical dynamics and thermal behaviour of the battery pack and is validated against the baseline Chen battery model within the IPG CarMaker vehicle simulation environment. The battery model serves as the foundation from which advanced state estimation, thermal management algorithms and powertrain energy management strategies are implemented to optimise the overall hybrid vehicle performance. To ensure robust online state tracking, a four-state Extended Kalman Filter (EKF) is integrated into the Battery Control Unit (BCU) to mitigate open-loop coulomb counting drift, bounding State of Charge (SOC) estimation errors within ± 0.02 and core temperature tracking discrepancies below $\pm 0.15\,^{\circ}\mathrm{C}$. Additionally, a Linear Parameter-Varying Model Predictive Control (LPV-MPC) strategy actively regulates the core battery temperature around an optimal $35\,^{\circ}\mathrm{C}$ threshold, preventing overheating under peak electrical transients of $\pm 200\,\mathrm{A}$ and $\pm 60\,\mathrm{kW}$. The complete closed-loop architecture is deployed within a full-vehicle co-simulation environment using IPG CarMaker for Simulink, and is evaluated across both the ARTEMIS driving cycle and a representative one-hour endurance racing stint on the Hockenheimring circuit. The hybrid electric powertrain, which integrates the HV battery management system, is governed by a rule-based Finite-State Machine (FSM) supervisory energy management strategy that dynamically exploits a usable SOC window of 54% to 80% to achieve strict charge-neutral operation, completing the full stint with approximately 10% fuel remaining, whereas an engine-only baseline suffers fuel starvation under identical racing demands. The coordination of powertrain subsystems, namely battery modelling, state estimation, thermal regulation and energy management, within a single real-time architecture delivers repeatable charge-sustaining performance and an openly documented framework for an area of research dominated by proprietary knowledge.

Contents

List of Acronyms . . . vi
Nomenclature . . . vii

1 Introduction 1
1.1 Background and Motivation of Study . . . 1
1.2 Purpose of Study . . . 2
1.3 Research Objective . . . 2
1.4 Main Contributions . . . 2

2 Literature Review 3
2.1 Hybrid Powertrains in Endurance Racing . . . 3
2.1.1 Endurance Racing Powertrain Architecture . . . 3
2.2 Battery Modelling Approaches . . . 4
2.2.1 Electrochemical Model of Battery System . . . 4
2.2.2 Equivalent Circuit Modelling of Battery System . . . 6
2.2.3 Empirical and Data-Driven Modelling Approaches . . . 7
2.3 Battery Management Strategies . . . 7
2.3.1 State of Charge Estimation . . . 7
2.3.2 State of Health Estimation . . . 9
2.3.3 Thermal Modelling and Management . . . 10
2.3.4 Coordinated Controller Strategy . . . 12
2.3.5 Metric for Performance Evaluations . . . 12
2.4 Conclusion of Literature Review . . . 13

3 Enhanced Battery Modelling Approach 14
3.1 IPG CarMaker Simulation Environment . . . 14
3.1.1 Co-Simulation Architecture and Simulink Coder Plug-In Integration . . . 14
3.1.2 CarMaker Baseline Architecture . . . 14
3.2 CarMaker Chen Battery Model . . . 15
3.2.1 Mathematical Description of Chen Battery Terminal Voltage . . . 16
3.3 State Dependent 2^{nd} Order Equivalent Circuit Model . . . 16
3.3.1 Mathematical Description of Battery State Behaviour . . . 17
3.4 Extended Battery Modelling Simulink Coder Plug-In Model . . . 19
3.5 Battery Modelling Conclusion . . . 19

4 Controller Strategy Development 20
4.1 State Estimation . . . 20
4.1.1 Recursive State Estimation Algorithm Framework . . . 20
4.1.2 State Estimation Algorithm . . . 21
4.1.3 Covariance Matrix Parametrization . . . 23

4.1.4 Implementation of State Estimation in Coordinated Framework . . . 23
4.2 State of Health Estimation . . . 23
4.2.1 State Estimation using Power Fade . . . 24
4.2.2 Parameter Correction Filter Implementation . . . 24
4.2.3 Implementation of Degradation in Coordinated Framework . . . 24
4.3 Battery Thermal Management System . . . 25
4.3.1 Battery Thermal Representations . . . 25
4.3.2 Coolant Mass Flow Rate Properties . . . 25
4.3.3 Thermal Management Controller Implementation . . . 26
4.4 Powertrain Energy Management Strategy . . . 28
4.4.1 Endurance Powertrain Control Architecture . . . 28

5 Simulations and Results 29
5.1 Battery Model Integration and Validation in IPG CarMaker . . . 29
5.1.1 Battery Model Baseline Response without SOC Dependence . . . 30
5.1.2 Battery Model Baseline Response with SOC Dependence . . . 31
5.1.3 Battery Model Baseline Response Discussion . . . 32
5.2 Extended State-Dependent High-Voltage Battery Model . . . 32
5.3 Battery Management Strategy for Battery State Tracking . . . 34
5.4 Preliminary Validation in ARTEMIS Driving Cycle . . . 34
5.4.1 Conventional Energy Management Strategy Performance . . . 35
5.4.2 Proposed Hybrid Control Strategy Performance . . . 35
5.5 Endurance Racing Driving Scenario Evaluation . . . 36
5.5.1 Conventional Control Long-Term Performance Assessment . . . 37
5.5.2 Hybrid Racing Control Long-Term Performance Assessment . . . 37
5.5.3 HV Battery Dynamics . . . 38
5.5.4 Thermal Management . . . 40
5.6 Discussion of Results . . . 41
5.6.1 Evaluation . . . 41
5.6.2 Limitations . . . 42

6 Conclusion and Recommendations 43
6.1 Conclusion . . . 43
6.2 Recommendations for Future Works . . . 44

Appendix 45
A.1 Battery Modelling Approach Implementation in MATLAB & Simulink . . . 45
A.1.1 State-Depended Model-Parameter 3D Lookup Tables . . . 45
A.1.2 Simulink Coder Plug-In Model for CarMaker Power Supply . . . 47
A.2 Controller Strategy Development in CarMaker for Simulink . . . 48
A.2.1 State Estimation implementation in CM4SL . . . 48
A.2.2 Single-move LPV-MPC for Battery Thermal Management . . . 51
A.2.3 Mechanical Energy Management Strategy Modes . . . 52
A.3 Chen Battery Model . . . 53

References 54

List of Figures

2.1 Configurations of parallel hybrid electric powertrain architectures [1] 4
2.2 Lithium-ion battery charge and discharge mechanism [2]. 5
2.3 Doyle-Fuller-Newman Framework [3] 6
2.4 Battery Model described by their 1st Order Thévenin Model [4] 6
2.5 General Nonlinear 2^{nd} Order Thevenin Model [5] 6
2.6 Temperature evolution and distribution for spatially distributed nodal modelling approach [6] . 10
2.7 Classification of coordinated EMS control architectures [7] 12
2.8 Lap time simulation indicating racing car's performance with motor control algorithm [8] 13

3.1 CarMaker Office Parallel Hybrid Configuration Overview with Rear Drive 15
3.2 IPG CarMaker Battery Model "Chen" 15
3.3 SOC non-linear correction factor applied to the Battery's OCV. 16
3.4 Higher Fidelity 2^{nd} Order Thévenin ECM 16

4.1 Schematic of Extended Kalman Filter Operation 21
4.2 Hybrid endurance parallel P2 powertrain PTControl strategy modes 28

5.1 CarMaker vehicle driving profile for the mountain driving cycle. 29
5.2 Chen battery dynamic response of developed 2nd Order ECM without SOC dependence 30
5.3 Powertrain modes and energy source contributions for Chen battery model without SOC dependence 30
5.4 Chen battery dynamic response of developed 2nd Order ECM with SOC dependence 31
5.5 Powertrain modes and energy source contributions for Chen battery model with SOC dependence 31
5.6 Extended 2nd Order ECM dynamic response with state dependence 32
5.7 Powertrain modes and energy source contributions for extended 2nd Order ECM with state dependence 33
5.8 Electro-thermal response of extended 2nd Order ECM 33
5.9 Extended 2nd Order ECM internal state tracking using EKF 34
5.10 Extended 2nd Order ECM internal state difference evaluation 34
5.11 CarMaker vehicle driving profile for ARTEMIS driving cycle 34
5.12 Powertrain modes and energy source contributions for extended 2nd Order ECM for ARTEMIS . 35
5.13 Extended 2nd Order ECM dynamic response with state dependence for ARTEMIS 35
5.14 Evaluation of battery internal states for ARTEMIS 36
5.15 CarMaker vehicle driving profile for Hockenheim racing driving cycle 36
5.16 Powertrain modes and energy source contributions for active racing EMS 37
5.17 Lap-profile showing charge-sustaining behaviour for 2nd Order ECM dynamic response with state dependence 38
5.18 Evaluation of SOH Degradation for 2nd Order ECM dynamic response with state dependence . . 39
5.19 SOC Dynamic Swing over racing profile stint 39

5.20 SOC and SOH drop per lap over the entire 1 hour simulation 40
5.21 Battery temperature tracking over the racing profile stint 40
5.22 Cooling circuit actuator response over the racing profile stint 41

1 State-dependent R_0 model-parameter 3D lookup table across charging and discharging operating conditions 45
1 State-dependent R_1 model-parameter 3D lookup table across charging and discharging operating conditions 45
1 State-dependent R_2 model-parameter 3D lookup table across charging and discharging operating conditions 45
1 State-dependent C_1 model-parameter 3D lookup table across charging and discharging operating conditions 46
1 State-dependent C_2 model-parameter 3D lookup table across charging and discharging operating conditions 46
1 State-dependent OCV model-parameter 3D lookup table across charging and discharging operating conditions 46
2 Simulink plug-in model for IPG CarMaker of HV battery power supply system 47
3 CarMaker execution chain and Battery Control Unit (BCU) state estimation architecture across the CM4SL model hierarchy 50
4 Battery dynamic response of developed 2^{nd} Order ECM with SOC dependence 53
5 Battery dynamic response of developed 2^{nd} Order ECM with SOC dependence 53

List of Tables

2.1 Battery Performance Evaluation Metrics for Hybrid Endurance Racing 13

List of Acronyms

AOC	Amount of Charge
ARTEMIS	Assessment and Reliability of Transport Emission Models and Inventory Systems
BCU	Battery Control Unit
BMS	Battery Management System
BTMS	Battery Thermal Management System
CC	Coulomb Counting
CM4SL	CarMaker for Simulink
DP	Dynamic Programming
ECM	Equivalent Circuit Model
EKF	Extended Kalman Filter
EM	Electric Motor
EMS	Energy Management Strategy
EV	Electric Vehicle
FMU	Functional Mock-up Unit
FSM	Finite-State Machine
HEV	Hybrid Electric Vehicle
HiL	Hardware in the Loop
HPPC	Hybrid Pulse Power Characterisation
HV	High-Voltage
I	Current
ICE	Internal Combustion Engine
ISG	Integrated Starter Generator
KF	Kalman Filter
Li-ion	Lithium-ion
LMDh	Le Mans Daytona Hybrid
LPV	Linear Parameter-Varying
LTI	Linear Time-Invariant
LV	Low-Voltage
MIMO	Multi-Input Multi-Output
MPC	Model Predictive Control
NTU	Number of Transfer Units
OCV	Open-Circuit Voltage
PI	Proportional-Integrator
PID	Proportional-Integral-Derivative
PMP	Pontryagin's Minimum Principle
QP	Quadratic Programming
RC	Resistor-Capacitor
RMSE	Root Mean Square Error
SEI	Solid Electrolyte Interphase
SOC	State of Charge
SOH	State of Health
T	Temperature
V-I	Voltage-Current
WEC	World Endurance Championship

Nomenclature

Symbol	Description	Unit
A_t	Heat transfer surface area	m^2
c	Specific heat capacity	$\mathrm{J\,kg^{-1}\,K^{-1}}$
C_1	Capacitance of the first RC branch	F
C_2	Capacitance of the second RC branch	F
C_p	Specific heat capacity	$\mathrm{J\,kg^{-1}\,K^{-1}}$
C_{th}	Thermal capacitance of the battery pack	$\mathrm{J\,K^{-1}}$
D_h	Hydraulic diameter	m
η_c	Coulombic charge and discharge efficiency	–
F_k	State transition matrix at time step k	–
G_k	Input (control) matrix at time step k	–
h	Convective heat transfer coefficient	$\mathrm{W\,m^{-2}\,K^{-1}}$
H_c	Cell height	m
i_{ECM}	Battery current from the ECM	A
I	Battery current (positive for discharge)	A
L_c	Cell length	m
m_c	Mass of a single battery cell	kg
$\dot{m}_{\mathrm{cool}}$	Coolant mass flow rate	$\mathrm{kg\,s^{-1}}$
n_p	Number of parallel cell connections	–
n_s	Number of series cell connections	–
Q	Process noise covariance	–
q_c	Nominal battery cell capacity	Ah
Q_C	Nominal battery pack capacity	Ah
$\dot{Q}_{\mathrm{gen}}$	Heat generation rate	W
$\dot{Q}_{\mathrm{in}}$	Convective and conductive heat transfer rate into system	W
$\dot{Q}_{\mathrm{out}}$	Convective and conductive heat transfer rate out of system	W
R	Measurement noise covariance	–
R_0	Internal ohmic resistance	Ω
R_1	Resistance of the first RC branch	Ω
R_2	Resistance of the second RC branch	Ω
P_0	Initial error covariance	–
ρ	Mass density	$\mathrm{kg\,m^{-3}}$
R_{th}	Thermal resistance of the battery pack	$\mathrm{K\,W^{-1}}$
SOC	State of charge	–
t	Time	s
t_c	Cell thickness	m

Symbol	Description	Unit
T_{amb}	Ambient temperature	°C
T_{batt}	Battery temperature	°C
u_k	Input (control) vector at time step k	–
U_{Battery}	Terminal voltage of the battery	V
U_{oc}	Open-circuit voltage	V
V	Volume of the battery	m^3
V_{batt}	State-dependent terminal voltage	V
v_k	Measurement noise vector at time step k	–
w_k	Process noise vector at time step k	–
$\hat{x}_{k,k}$	Estimated (corrected) state vector at time step k	–
$\hat{x}_{k+1,k}$	Predicted state vector at time step $k+1$ given step k	–

1

Introduction

1.1. Background and Motivation of Study

Hybrid powertrains, particularly in motorsport, rely heavily on the Electric Motor (EM) to deliver additional power and to recover energy through regenerative braking, with the High-Voltage (HV) battery system acting as the central energy buffer that alternates between a load and a generator to govern both capabilities [8]. The performance of the overall hybrid system is therefore tightly coupled to how accurately the battery's behaviour can be represented, since the control strategies that manage power flow between the Internal Combustion Engine (ICE) and EM depend on a reliable estimation of the battery's available power, State of Charge (SOC), and thermal limits to operate effectively under real-time driving conditions.

The HV Lithium-ion (Li-ion) battery is a highly complex system, that is both nonlinear and non-stationary, incorporating coupled electrical, thermal, and electrochemical dynamics [6]. The demand for this knowledge in motorsport makes battery modelling and system management a crucial research area. However, despite rapid advancements in hybrid motorsport technologies, publicly available research capturing the full complexity of hybrid race vehicles remains limited, as much of the knowledge is proprietary. Battery modelling is critical to understanding battery behaviour in order to improve system performance and increase efficiency [9]. By modelling the Li-ion battery as a dynamic model described by discrete electrical elements [10], the resulting knowledge can be applied to real-world systems. An accurate and computationally efficient Li-ion battery model is beneficial for developing SOC and State of Health (SOH) algorithms for a Battery Management System (BMS) [11] as well as estimating the thermal behaviour to implement an efficient thermal management system that can regulate pack temperature to improve overall performance [12].

Hybrid endurance racing presents an extreme operating environment characterised by continuous, high-rate energy and severe transient loading. The battery system undergoes intense electro-thermal fatigue that is driven by repetitive, bidirectional current surges during peak acceleration and high-power regenerative braking [13, 14]. Accurately capturing these non-linear internal dynamics through robust modelling techniques is critical for supervisory energy management, otherwise unmanaged transient loading leads to thermal accumulation, accelerated degradation and power limitations [15] which compromise not only the performance of the racing vehicle but also system safety under continuous racing conditions.

1.2. Purpose of Study

The primary objectives of this study comprise three main components:

1. **Battery Modelling:** To develop an accurate representation of a HV Li-ion battery based on a 2nd-order Equivalent Circuit Model (ECM) incorporating state-dependent Resistor-Capacitor (RC) and Open-Circuit Voltage (OCV) parameters.
2. **Battery State Tracking:** To implement advanced internal state monitoring and control algorithms for robust SOC estimation and an active thermal management strategy to regulate core battery temperatures.
3. **Powertrain Energy Management System:** To integrate a supervisory control strategy that optimises power distribution between the ICE and EM, maximising overall hybrid powertrain efficiency and performance in endurance racing applications.

The primary objectives are intended to be coordinated into a single, integrated battery management system architecture, in which the battery model, state and thermal estimation algorithms, and powertrain energy management strategy operate as a unified framework rather than as separate subsystems. This architecture is to be developed in MATLAB/Simulink with real-time application in mind, and integrated into a co-simulation environment with IPG CarMaker for system-level validation against representative driving conditions.

1.3. Research Objective

This study aims to extend a validated battery model to accurately characterise its electrochemical behaviour, thermal dynamics, and nonlinear SOC dependencies for hybrid endurance racing applications by developing a state-dependent 2^{nd} order ECM coupled with advanced battery controller strategies for state estimation and thermal management as well as an energy management control unit to optimise energy deployment and recuperation, ensuring safe, efficient, and reliable battery operation within the hybrid powertrain.

1.4. Main Contributions

The key contributions of this study are summarized as follows:

- **State-Dependent Equivalent Circuit Modelling:** Extend a validated baseline battery model into a state-dependent 2nd Order ECM within MATLAB/Simulink to accurately capture non-linear electro-thermal battery dynamics for a Le Mans Daytona Hybrid (LMDh) parallel powertrain.
- **Online Internal State Tracking and Thermal Management:** Extend an existing three-state formulation to develop a four-state Extended Kalman Filter (EKF) for accurate, real-time monitoring of internal battery states, coupling state estimation directly with active thermal control to proactively enforce temperature constraints and prevent overheating during sustained high-power driving profiles.
- **Coordinated Real-Time Control Architecture:** Formulate a unified, multi-objective control strategy that seamlessly integrates battery state estimation, thermal regulation, and powertrain energy management into a computationally efficient architecture designed for real-time simulation.
- **Full-Vehicle Co-Simulation and Endurance Evaluation:** Integrate the extended battery model and control algorithms into a closed-loop IPG CarMaker for Simulink environment, executing full-lap and multi-lap simulations to evaluate charge-sustaining operation, fuel consumption, and dynamic state tracking under extreme endurance racing conditions.

2

Literature Review

This chapter conducts a comprehensive review of related work for mathematically quantifying the nonlinear dynamics of a battery pack system, together with baseline battery control algorithms for state estimation, thermal management, and energy management strategies. Hybrid endurance racing defines the application context, with the battery system and its associated control algorithms evaluated under real-time, high-power demand simulations representative of an endurance race stint. Battery performance is assessed over a representative drive cycle to capture the electrochemical, thermal, and degradation dynamics relevant to both battery management and the broader powertrain energy management and driving-mode strategy. While the research question addressed in this thesis lies in a niche area not specifically covered in available literature, owing to the proprietary nature of hybrid endurance knowledge in motorsport applications, a substantial content of related work related to battery modelling, control algorithms, and battery management strategies is evaluated and discussed in terms of its real-time implementation feasibility and modelling complexity.

2.1. Hybrid Powertrains in Endurance Racing

Endurance racing represents a fundamentally different and more demanding operating environment than conventional or long-duration driving applications, and is characterised by cyclic, high-power loading over an extended period of time, ranging from 4 to 24 hours. Vehicle performance is governed not only by the peak power output of the propulsion components [16, 17], but by the optimisation of energy management strategies aimed at lap-time minimisation while respecting the strict energy usage constraints imposed by technical regulations [18].

2.1.1. Endurance Racing Powertrain Architecture

Review of the literature found that parallel hybrid powertrain architectures are the most well suited to motorsport applications, as the ICE and EM can contribute to wheel torque either independently or simultaneously [8, 16, 19, 20, 21]. The parallel layout offers structural simplicity, requiring only the integration of an EM, inverter, and battery, together with minimal added weight compared to other hybrid architectures [8]. Depending on the specific placement of the EM relative to the ICE and the drivetrain, parallel hybrid architectures are classified into distinct configurations [22] listed below and shown in Figure 2.1:

- **P0:** Connected to the engine crankshaft by a belt or gear system.
- **P1:** Connected directly to the crankshaft.
- **P2:** Connected between the crankshaft and transmission, after the clutch.
- **P3:** Connected between the transmission and differential.
- **P4:** Connected to an axle separate from the engine.

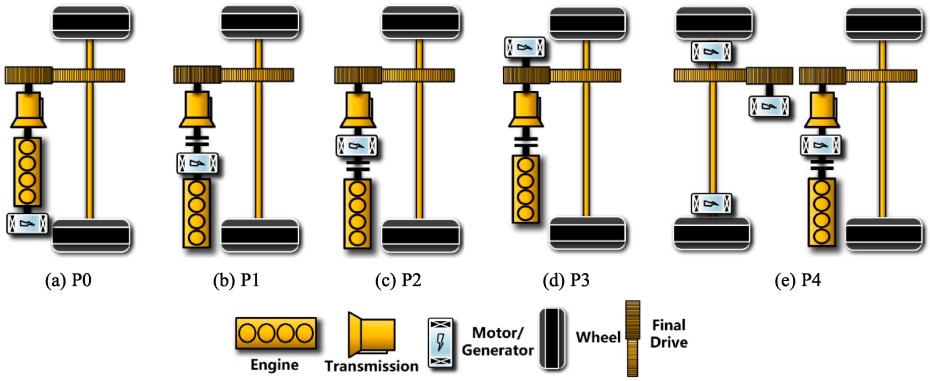


Figure 2.1: Configurations of parallel hybrid electric powertrain architectures [1]

The most widely adopted configuration in racing applications comprises an ICE alongside an EM capable of operating as either a motor or a generator [16, 17]. While consumer vehicle and racing parallel hybrid powertrains are structurally similar, their power flow management strategies differ significantly due to differing performance objectives and operational constraints. In racing applications, parallel configurations are shown to reduce overall energy consumption while maintaining competitive performance when governed by an advanced Energy Management Strategy (EMS) [19]. Effective control is therefore central to realising these benefits, ensuring that the ICE operates close to its peak efficiency region, or is switched off entirely, to avoid unnecessary fuel consumption and inefficient power output [16]. Regenerative braking and strategic power management offer further opportunities for energy conservation and emission reduction [8, 17, 20, 23]. As a result, parallel Hybrid Electric Vehicle (HEV) technology is regarded as one of the most effective solutions for improving fuel efficiency while maintaining high vehicle performance. However, this results in increased system complexity, since the power management strategy must coordinate the interaction of nonlinear components across mechanical, electrical, thermal, and control domains [20, 23].

2.2. Battery Modelling Approaches

Battery modelling refers to the mathematical and computational representation of the physical behaviour of the powertrain's power supply, allowing its performance to be evaluated in a virtual simulation environment under specified conditions. Li-ion batteries are the predominant energy storage technology in both Electric Vehicle (EV) and HEV applications due to their high energy density, extended cycle life, low self-discharge rates, and high efficiency [5, 23, 24, 25, 26]. Battery models are broadly classified into four categories: electrochemical, ECMs, empirical and data-driven [3, 5, 27] and are discussed in this section.

2.2.1. Electrochemical Model of Battery System

A lithium-ion battery converts chemical energy into electrical energy during discharge, a process reversed during charging. Each cell within a battery pack consists of a positive electrode, a negative electrode, an electrolyte, and a separator, a thin, micro-perforated membrane that separates the electrodes while allowing ions to pass through [2]. The negative electrode is composed of graphitic carbon, the positive electrode is typically a lithium metal oxide, and the electrolyte solution provides the ionic pathway between them [28].

During discharge, lithium ions are released from the negative electrode and travel through the electrolyte to the positive electrode, while electrons simultaneously flow through the external circuit, producing electrical energy. Charging reverses this process, driving lithium ions back to the negative electrode and this entire mechanism can be visualised in Figure 2.2.

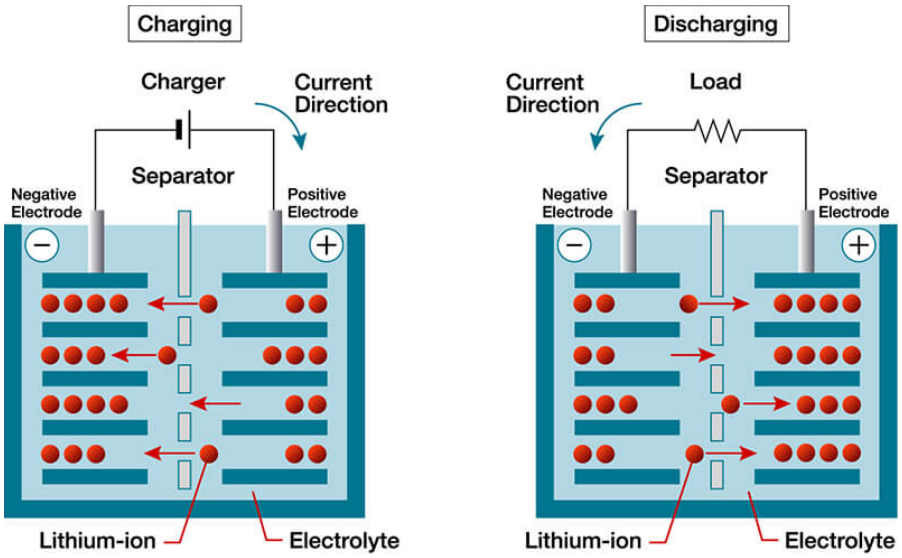


Figure 2.2: Lithium-ion battery charge and discharge mechanism [2].

The electrochemical processes governing battery operation exhibit several coupled, nonlinear loss mechanisms that directly determine the terminal voltage under a given load. An instantaneous ohmic voltage drop occurs as a result of the resistance of the electrodes and electrolyte solution, while slower polarisation losses arise from two distinct mechanisms, namely the charge double-layer effect and solid-state diffusion dynamics [6]. The charge double-layer effect occurs when current flows and ions in the electrolyte and electrons in the electrode accumulate at the electrode-electrolyte interface, forming two opposing charge layers that behave similarly to a capacitor which builds up and dissipates quickly when the current changes, producing a fast short-term transient voltage response [29]. Solid-state diffusion and concentration polarisation arise because lithium ions do not instantly distribute uniformly through the electrode particle during intercalation, but instead diffuse slowly through the solid material from the surface inward during charging and outward during discharging, creating a concentration gradient that takes considerably longer to equalise and produces a slower long-term transient voltage response [6, 30].

The nonlinear loss mechanisms, described by the instantaneous voltage drop and slow polarisation losses, are strongly state-dependent since the internal resistance, diffusion coefficients, and reaction rates vary non-linearly with temperature, SOC, and applied load [6]. Physics-based models, such as the Doyle-Fuller-Newman framework shown in Figure 2.3, offer high-fidelity by capturing these mechanisms from first principles by solving coupled partial differential equations governing ion transport, reaction kinetics, and heat generation across the electrode and electrolyte [3, 27]. Repeated charge-discharge cycling progressively degrades these electrochemical properties through a series of coupled physicochemical mechanisms caused by operating stressors acting on the battery system [24, 31, 32]. The propagation of these inherent physicochemical mechanisms such as Solid Electrolyte Interphase (SEI) layer formation, electrolyte decomposition and lithium plating which cause battery degradation, effectively causes the available power and capacity to diminish over time. Temperature, current load and high cell voltage are the most significant contributors to accelerating the effects of degradation, making these states critical variables to monitor and regulate in real-time [24].

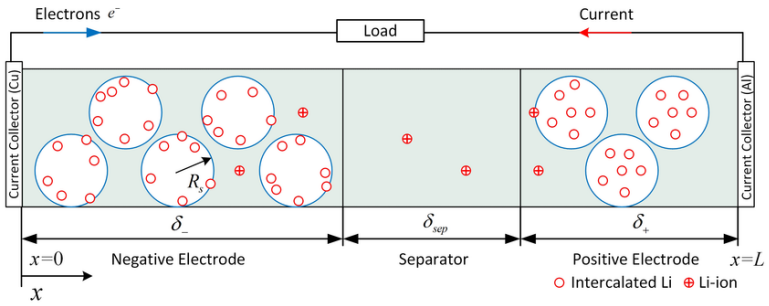


Figure 2.3: Doyle-Fuller-Newman Framework [3]

2.2.2. Equivalent Circuit Modelling of Battery System

An ECM represents the electrochemical behaviour of the battery using discrete electrical elements, without solving the underlying partial differential equations governing ion transport and reaction kinetics [33]. This provides a computationally efficient yet physically meaningful representation well suited to real-time battery management applications [3, 27]. The simplest representation, the internal resistance model, captures only instantaneous ohmic losses and cannot reflect polarisation voltage behaviour. The first-order Thévenin model, shown in Figure 2.4 extends this with a single RC branch to characterise ohmic and concentration polarisation. However, its accuracy diminishes with variations in battery ageing and operating conditions [4, 5].

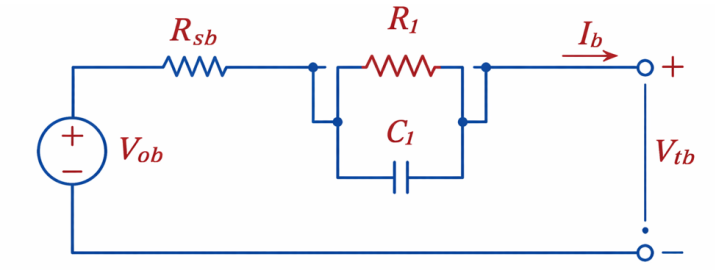


Figure 2.4: Battery Model described by their 1st Order Thévenin Model [4]

The 2^{nd} Order Thevenin ECM, illustrated in Figure 2.5, extends the first-order model by introducing two RC branches in series with the internal resistance R_0 and OCV source, capturing both the fast charge-transfer and slower diffusion polarisation dynamics of the battery [5]. The 2^{nd} Order Thevenin ECM is an effective balance between model complexity and accuracy, making it computationally efficient, straightforward to implement and calibrate, and physically interpretable [29, 34]. It remains a predominant and well-validated foundation for a wide range of state estimation algorithms and BMS implementations [34].

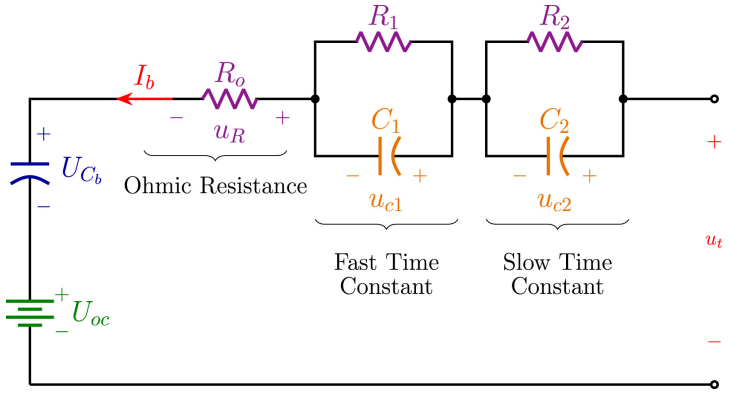


Figure 2.5: General Nonlinear 2^{nd} Order Thevenin Model [5]

The 2^{nd} Order ECM captures two RC branches that directly correspond to the distinct polarisation mechanisms described in Section 2.2.1 for the electrochemical behaviour of the battery system. The first branch (R_1, C_1) captures the fast short-term transient arising from the charge double-layer effect at the electrode-electrolyte interface, while the second branch (R_2, C_2) captures the slower long-term transient produced by solid-state diffusion and concentration polarisation within the electrode particles [29, 30]. The two RC effectively capture the electrochemical polarisation dynamics, ensuring the model accurately reproduces the full transient voltage response of the battery. The ECM is capable of correlating the electrochemical phenomena with circuit elements that offer a reduced computational demand while capturing the nonlinear behaviours making them computationally feasible and practical for system-level applications [35].

2.2.3. Empirical and Data-Driven Modelling Approaches

The accuracy of the 2^{nd} Order ECM is determined not only by its circuit topology, but critically by whether its parameters are treated as fixed constants or allowed to vary with the battery's internal states. The parameters R_0, R_1, C_1, R_2, C_2, and OCV are each sensitive to temperature, SOC, and applied current [29, 30, 34]. Most ECM-based approaches rely on parameters identified at fixed temperatures, limiting their accuracy under the fluctuating thermal and loading conditions of real-world operation [34], where temperature plays the most significant role in driving parameter variation, followed by SOC [24, 30]. State-dependent parameters are commonly identified empirically through the Hybrid Pulse Power Characterisation (HPPC) test, a standardised characterisation procedure that discharges the battery at a constant current, allows it to rest, and applies a charge pulse, repeated across a range of SOC and temperature values [11]. The measured voltage and current response allows the dynamic behaviour of the battery's internal parameters to be identified and implemented as state-dependent lookup tables, ensuring the ECM accurately reflects battery behaviour across the full operating range [11, 36, 37]. Machine learning approaches extend this further, with Qi et al. 2025 building on a second-order RC ECM with a back-propagation neural network to compensate for terminal voltage errors introduced by temperature variations and dynamic discharge rates, improving SOC estimation accuracy while retaining computational efficiency. This offers improved accuracy, though such approaches remain dependent on training datasets and often lack physical interpretability.

2.3. Battery Management Strategies

The BCU is a central control unit that optimises battery operation and safeguards the system against critical electrical and thermal faults [38]. To maximise performance and extend service life, the BMS relies on the accurate estimation of internal battery states, specifically SOC and SOH, using representative battery models [5]. However, these states cannot be directly measured due to the battery's inherent nonlinearity, electrochemical complexity, and sensitivity to operational uncertainties such as sensor noise and current fluctuations [30].

2.3.1. State of Charge Estimation

Accurate state estimation is fundamental to the BMS, governing charging and discharging protocols, safety mechanisms, and energy management strategies. The SOC cannot be directly measured and is directly influenced by temperature, ageing, and operating conditions, therefore accurate real-time estimation is essential to prevent hazardous overcharge and over-discharge, extend battery lifespan, and enable energy-optimised control [34]. The presence of operational uncertainties, including sensor noise, temperature variation, and current fluctuations, introduces estimation errors that must be actively managed [5, 30].

Coulomb Counting

Coulomb Counting (CC), also referred to as ampere-hour integration, estimates SOC by integrating the battery current over time relative to the nominal capacity. The SOC is shown mathematically in Equation 2.1 as described by [11, 34]. The algorithm is simple and computationally inexpensive. However, CC is an open-loop state estimation strategy that assumes no measurement error is present.

$$\mathrm{SOC}(t) = \mathrm{SOC}(0) - \frac{1}{3600 Q_C} \int_0^t I \, dt \tag{2.1}$$

Kalman Filter-Based State Estimation

The Kalman Filter (KF) is widely adopted for state estimation due to its high computational efficiency and low memory overhead, operating recursively on current and previous state data without storing full historical datasets [37]. It relies on a standard prediction-correction architecture and maps system input-output relationships through state-space equations to effectively suppress noise interference and update unobservable internal state estimates via terminal error feedback [39]. The EKF extends this to nonlinear systems and is widely used for SOC estimation to improve accuracy by accounting for nonlinear electrochemical behaviour and ageing effects [35]. Abdelkhalek and Bayezit 2024 represents the EKF for SOC estimation using a first-order ECM, described below:

$$\frac{d}{dt}\mathrm{SOC} = -\frac{I}{3600 \cdot Q_c} \tag{2.2}$$

$$\frac{d}{dt} V_1 = \frac{I}{C_1(\mathrm{SOC})} - \frac{V_1}{R_1(\mathrm{SOC}) \cdot C_1(\mathrm{SOC})} \tag{2.3}$$

$$\frac{d}{dt} R_0 = 0 \tag{2.4}$$

$$V_t = V_{OCV}(\mathrm{SOC}) - I \cdot R_0 - V_1 \tag{2.5}$$

The state vector is given by $x = \begin{bmatrix} \mathrm{SOC} & V_1 & R_0 \end{bmatrix}$ and nonlinear process and observation functions are:

$$f(x, i) = \begin{bmatrix} \dfrac{-i}{3600 \cdot AH} \\ \dfrac{i}{C_1(\mathrm{SOC})} - \dfrac{V_1}{R_1(\mathrm{SOC}) \cdot C_1(\mathrm{SOC})} \end{bmatrix} \tag{2.6}$$

$$h(x, i) = V_{OCV}(\mathrm{SOC}) - i \cdot R_0 - V_1 \tag{2.7}$$

To approximate the nonlinear system, the process and observation functions are linearised at each time step through online computation of the Jacobian matrices F and H with sample time T_s and these are given by:

$$F = \begin{bmatrix} 1 & 0 & 0 \\ 0 & e^{\frac{-T_s}{R_1 C_1}} & 0 \\ 0 & 0 & 1 \end{bmatrix} \tag{2.8}$$

$$H = \begin{bmatrix} \dfrac{-I}{3600 \cdot Q_c} & \dfrac{I}{C_1(\mathrm{SOC})} - \dfrac{V_1}{R_1(\mathrm{SOC}) \cdot C_1(\mathrm{SOC})} \end{bmatrix} \tag{2.9}$$

Qi et al. 2025 proposes a dual KF framework that combines open-loop CC with two sequential filtering layers driven by real-time physical sensor data. Measured battery current provides the input for open-loop CC state propagation, while measured terminal voltage drives an EKF correction layer to resolve non-linear ECM prediction errors. A secondary linear KF layer then suppresses residual CC integration drift and modelling uncertainties, thereby improving overall SOC tracking accuracy.

The dual-filter scheme is formulated around a temperature-dependent second-order ECM in discrete state space form, defined by state vector $x = [\text{SOC}\ V_1\ V_2]^T$, input $u = I$, and output $y = V$ [37] and is given as follows:

$$\begin{cases} x_{k+1} = Ax_k + Bu_k + \omega_k \\ y_k = Cx_k + Du_k + v_k \end{cases} \tag{2.10}$$

where ω_k and v_k denote process and measurement noise, and the system matrices are:

$$A = \begin{bmatrix} 1 & 0 & 0 \\ 0 & e^{\frac{-t}{R_1 C_1}} & 0 \\ 0 & 0 & e^{\frac{-t}{R_2 C_2}} \end{bmatrix}, \quad B = \begin{bmatrix} \frac{\eta t}{Q} \\ R_1\left(1 - e^{\frac{-t}{R_1 C_1}}\right) \\ R_2\left(1 - e^{\frac{-t}{R_2 C_2}}\right) \end{bmatrix} \tag{2.11}$$

$$C = \begin{bmatrix} \frac{d\text{OCV}}{d\text{SOC}} & 1 & 1 \end{bmatrix}, \qquad D = R_0$$

The KF is a highly efficient, recursive algorithm that accurately estimates unknown internal states and suppresses noise interference using only current and previous state data, requiring minimal memory [37]. The EKF significantly improves SOC estimation accuracy by accounting for non-linear electrochemical behaviour and ageing, and is often combined with standard CC to maximise precision [35]. Standard industry implementations, such as the battery SOC estimator in MathWorks Simscape Battery, likewise utilise a static 3-state formulation represented by a state vector to dynamically estimate SOC alongside the polarization voltages across the RC branches [40]. This benchmark model relies on a standard prediction-correction architecture where state predictions are updated using terminal voltage error feedback.

2.3.2. State of Health Estimation

SOH quantifies the battery's current condition relative to its fresh state, reflecting the cumulative effect of mechanical and chemical degradation that is an inevitable outcome of repeated charge-discharge cycling [38]. As the battery undergoes irreversible chemical ageing, such as active lithium loss and electrode structural damage, its capacity exhibits permanent degradation that is independent of external operating conditions [34]. The SOH is typically expressed as a percentage of the current maximum capacity to the nominal capacity [10]:

$$\text{SOH} = \frac{Q_{max}}{Q_c} \cdot 100 \tag{2.12}$$

Jeon et al. 2026 presents a framework for jointly diagnosing capacity fade and power fade in Li-ion batteries from early-cycle health indices, using a model to predict both degradation modes and classify the underlying mechanisms. Capacity fade, shown in Equation 2.12, evolves non-linearly, whereas power fade typically progresses approximately linearly over cycling due to the gradual growth of the solid electrolyte interphase layer and the associated rise in internal resistance, which is quantified by the rate at which the average discharge voltage decreases over successive cycles. SOH estimation can be addressed using similar recursive filter frameworks to those applied for SOC estimation. A Kalman-based linear filter is commonly adopted to reconstruct the internal resistance of the cell as a proxy for the degradation state, accounting for nonlinear ageing effects over extended cycling [35, 38]. To actively mitigate degradation, online controllers must protect the battery from operating conditions that accelerate capacity fade. Adaptive Model Predictive Control (MPC) is also well suited to this purpose, accounting for the time-varying and ageing characteristics of the battery through a rolling-horizon optimisation with an entropy-weighted cost function [42]. This strategy is shown to reduce peak battery currents and cumulative ampere-hour throughput compared to conventional Proportional-Integrator (PI) controllers, directly slowing capacity fade [42].

2.3.3. Thermal Modelling and Management

Thermal models describe the temperature distribution within the battery and are fundamental for temperature prediction and control to ensure safe operation [43]. Battery operating temperature has a significant impact on battery performance and longevity. Elevated temperatures accelerate internal side reactions and risk thermal runaway, while low temperatures increase internal resistance and reduce available capacity [12].

Battery Thermal Model

Battery thermal models range from simple lumped representations, which treat the cell as a single thermal mass with a uniform average temperature, to spatially distributed nodal models, which discretise the cell geometry to resolve temperature gradients across its volume [43]. A lumped thermal model assumes a uniform temperature distribution over the battery pack [6, 44, 45] which makes it well suited to control-orientated thermal management systems. Mesbahi et al. 2021 applies this approach to determine the temperature of a 40 Ah Li-ion battery cell with a Nickel Manganese Cobalt Oxide cathode and graphitic anode, where the thermal behaviour of the cell is governed by the following energy balance:

$$\rho c V \frac{dT}{dt} = \dot{Q}_{gen} + \dot{Q}_{in} - \dot{Q}_{out} \tag{2.13}$$

The internal heat generated within the cell is represented by the term $\dot{Q}_{gen}$, while $(\dot{Q}_{in} - \dot{Q}_{out})$ accounts for heat transferred to and from the cell by conduction and convection. The internal heat generation arises from two sources, namely a reversible thermodynamic contribution due to entropy changes during the cell reaction, and an irreversible contribution due to Joule heating losses [6, 46]. A nodal thermal model adopts a spatially distributed approach, discretising the cell geometry into a grid and solving the heat equation at each node to produce temperature and heat generation distributions across the cell volume, as demonstrated by Mesbahi et al. 2021 and illustrated in Figure 2.6. While this approach captures spatial temperature non-uniformity and localised heat generation effects, its computational cost scales with the number of nodes, making it impractical for real-time simulation.

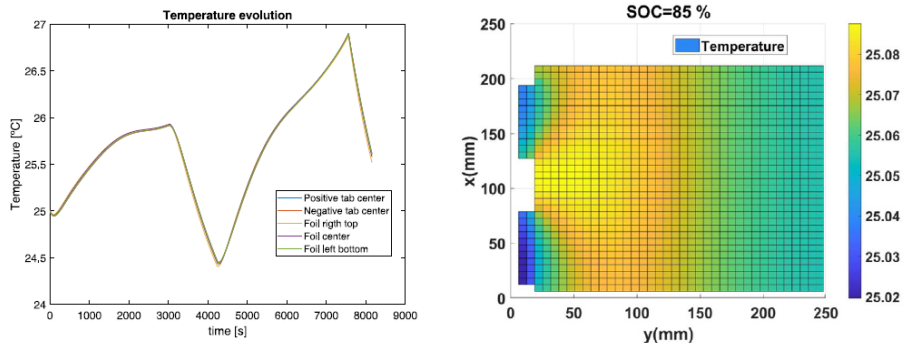


Figure 2.6: Temperature evolution and distribution for spatially distributed nodal modelling approach [6]

Coolant Heat Transfer Modelling

Accurate supervision of the battery pack temperature is essential for effective cooling, particularly when subjected to extreme loading conditions typical of endurance racing, where internal heat generation is the primary driver of temperature rise within the cell [43]. Li et al. 2023 investigates liquid cooling configurations for battery thermal management using computational fluid dynamics, providing a framework for quantifying the heat removed by the coolant. The heat removed by the coolant, corresponding to $\dot{Q}_{in}$ in Equation 2.13, is obtained from the coolant energy balance defined by:

$$\dot{Q}_{cool} = m_{cool} c_{p,cool} \epsilon \left(T_{batt} - T_{cool,in} \right) \tag{2.14}$$

While the physical fluid properties and thermal boundary conditions in Equation 2.14 are readily known or measured, the effectiveness ε is derived from the Number of Transfer Units (NTU) under a constant surface temperature assumption:

$$\varepsilon = 1 - e^{-NTU} \tag{2.15}$$

where $NTU = \frac{hA_t}{m_{cool} c_{p,cool}}$ is determined by the overall heat transfer coefficient between the battery and the coolant that be obtained from determining the Nusselt number.

$$h = \frac{Nu \cdot k}{D_h} \tag{2.16}$$

The coolant flow regime must be accurately characterised to evaluate Nu, which is determined from the Reynolds number [44] where for fully developed turbulent flow, the Nusselt number is evaluated using the Dittus-Boelter correlation [47]:

$$Nu = 0.023 \cdot Re^{0.8} \cdot Pr^{0.3} \tag{2.17}$$

Battery Thermal Management

Battery performance, including efficiency, capacity, lifespan, and safety, is significantly affected by extreme temperature variation, making the Battery Thermal Management System (BTMS) a critical technology for battery research and application [44, 45]. Effective thermal management relies on minimising internal heat generation and regulating cell temperature and three available strategies dominate in literature, namely rule-based control, Proportional-Integral-Derivative (PID) control, and MPC.

Rule-based strategies apply a predefined logic, typically on-off switching or constant flow rate operation, to maintain the battery within its permissible temperature range [45, 48]. Singh et al. 2025 implements a rule-based EMS incorporating BTMS for a fuel-cell-supplemented heavy-duty electrified vehicle over a standard drive cycle, applying a constant coolant flow rate that successfully maintains system temperature within recommended limits. While rule-based strategies are widely used in production vehicles due to their simplicity and reliability, they adapt poorly to dynamic operating conditions and offer limited energy efficiency, making them insufficient for demanding applications such as endurance racing [45].

PID controllers are widely adopted in industrial thermal management due to their simplicity and reliability, determining the required actuator output through a linear combination of proportional, integral, and derivative terms of the input error [44]. To address the non-linear, time-varying dynamics of battery thermal systems, fuzzy and hierarchical PID schemes dynamically adapt parameters, outperforming conventional PID in multi-objective thermal regulation and reducing cooling energy consumption by over 70% relative to constant-flow baselines [44, 49]. However, PID strategies are typically applied to a single actuator, and the lack of coordination between multiple actuators can result in energy loss when several control variables are involved [45].

MPC handles multiple objectives, constraints, and disturbances simultaneously, and is effective for controlling Multi-Input Multi-Output (MIMO) systems with high robustness, making it well suited to battery thermal management applications [45]. Adaptive MPC further exploits the electrical and thermal coupling of the battery through a rolling-horizon optimisation, simultaneously regulating current demand and thermal loading, which is particularly relevant to hybrid endurance racing applications [42]. Lopez-Sanz et al. 2017 implements a nonlinear MPC for multi-variable high-voltage battery and power electronics cooling circuits, while Park and Ahn 2020 develops a stochastic MPC incorporating probabilistic heat generation predictions. Further, Guo et al. 2024 formulates thermal management mode selection as an optimal control problem using nonlinear MPC solved via Dynamic Programming (DP). However, while DP provides a globally optimal solution, state and continuous control signal discretisation requires significant computational resources [16, 45, 52].

2.3.4. Coordinated Controller Strategy

Battery management strategies have traditionally treated the BTMS and EMS as isolated control problems, limiting simultaneous improvements in energy efficiency, thermal safety, and long-term durability under variable driving conditions [7]. Pan et al. (2026) notes that modern strategy framework designs are shifting toward coordinated setups such as rule-based, optimisation-based, learning-based, and hierarchical methods, seen in Figure 2.7. However, accurately modelling the battery dynamics and coordinating EMSs for real-time feasibility and implementation are still major challenges.

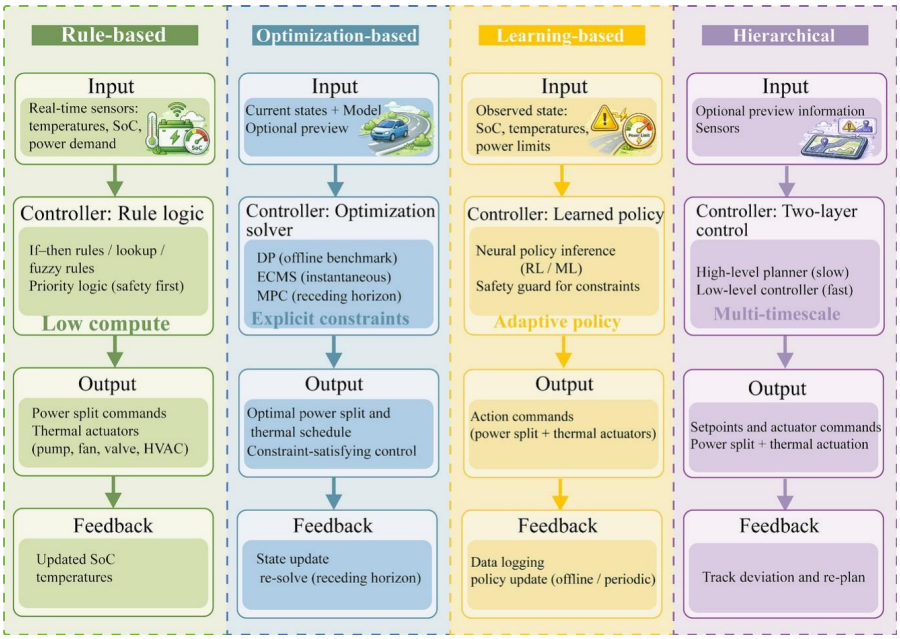
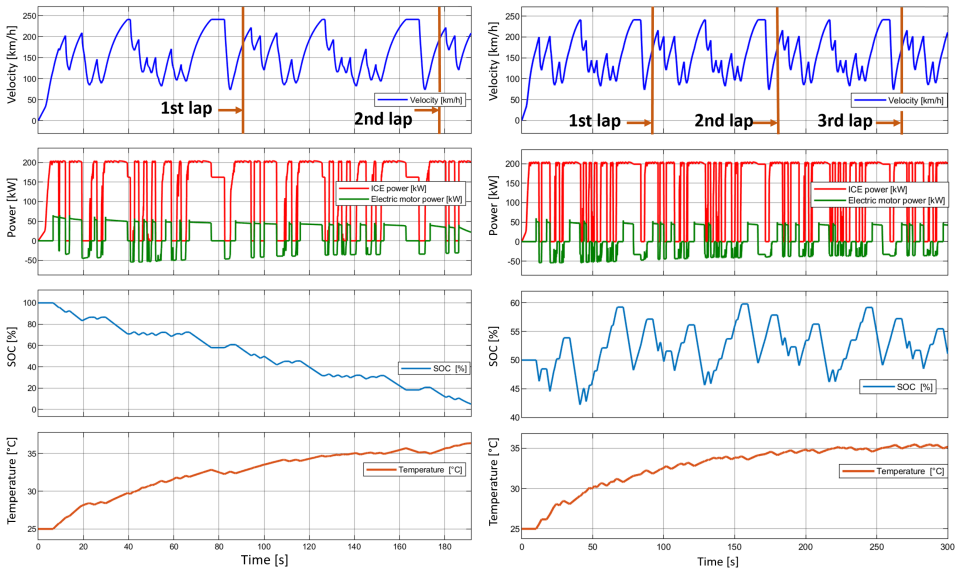


Figure 2.7: Classification of coordinated EMS control architectures [7]

The accurate modelling of battery dynamics coupled with coordinating EMSs for real-time feasibility and implementation remains a major challenge that is continuously being addressed through novel solutions. srikiran 2023 integrates receding-horizon MPC with adaptive estimators, such as unscented KF and Recursive Least Squares, achieving proactive thermal management and an estimated 12–18% increase in battery longevity. Similarly, Feng et al. 2020 employs a coupled electrochemical-thermal-neural-network model combined with an Unscented KF for robust SOC and temperature co-estimation across extreme ambient conditions (−10 to 40°C) and high discharge rates (up to 10 C).

2.3.5. Metric for Performance Evaluations

In endurance racing, battery systems endure intense thermal and electrical loads during repetitive, high-current cycles over continuous stints lasting from 4 up to 24 hours. To sustain optimal performance, the EMS of the hybrid powertrain is evaluated on its ability to maintain energy balance throughout a race. Hybrid powertrains offer significant lap time advantages over conventional ICE vehicles. However, the increased mass has the potential to negatively impact the vehicle performance, which further emphasises the importance of optimising and evaluating the coordinated EMS [23]. Malikov et al. 2025 addresses this challenge and finds that hybrid powertrains offer significant lap time advantages over conventional ICE. However, Figure 2.8(a) shows that without an effective controller strategy, the fully charged battery depletes the available energy in 200s. The advanced control algorithm is developed to address this shortcoming by dynamically managing the energy depletion and generation which is shown by the battery's SOC maintained within a stable 15% window in Figure 2.8(b) for optimal, repeatable lap times.



(a) Simulation without EM control algorithm **(b)** Simulation without EM control algorithm

Figure 2.8: Lap time simulation indicating racing car's performance with motor control algorithm [8]

The performance of advanced controller algorithms developed for hybrid powertrains must be evaluated against knowledge obtained from available related works and those operational boundaries that are satisfied in previous works are summarised in Table 2.1.

Table 2.1: Battery Performance Evaluation Metrics for Hybrid Endurance Racing

Metric	Description	Evaluation Criteria
SOC Swing	Peak-to-peak charge fluctuation per lap.	An optimal function range, between 5%–50%, is maintained by constraining the operational boundary battery limits to ensure that the system can satisfy rapid acceleration demands, support high-frequency load components and maintaining optimal operational range. [8, 15]
Cumulative ΔSOC	Net change in battery charge per lap.	Endurance racing requires charge-sustaining operation ($\Delta SOC/lap \approx 0$) to prevent long-term battery depletion that negatively impacts overall powertrain performance [8, 26].
Lap-to-Lap Consistency	Repeatability of energy management across stint simulation.	Strict energy balance preserves identical charge and discharge power limits to maintain repeatable lap times [8].

2.4. Conclusion of Literature Review

This chapter reviews existing work surrounding hybrid powertrains in endurance racing, virtual simulation environments, battery modelling approaches, and advanced battery management strategies. The analysis demonstrates that virtual simulation of the EMS for hybrid motorsport applications demands real-time feasibility, computational efficiency, and physical interpretability. However, existing literature reveals a notable gap regarding battery system modelling techniques, that describe the electrochemical behaviour in real-time, coupled with control algorithms for state estimation, thermal regulation and energy distribution specific to hybrid endurance racing applications. This review establishes the methodological foundation required for the battery system architectures and controller strategies developed in this thesis by evaluating various modelling frameworks alongside baseline control algorithms.

3

Enhanced Battery Modelling Approach

Batteries are energy storage devices that can be represented mathematically to quantify the electrochemical behaviour that converts chemical energy into electrical energy. The underlying nanoscale phenomena of battery operation, described in Section 2.2.1, are computationally intensive and not feasible for real-time simulation. The ECM is therefore adopted as a practical modelling approach for the purpose of this study.

3.1. IPG CarMaker Simulation Environment

IPG CarMaker is a vehicle simulation environment for software-in-the-loop testing that can be extended to hardware-in-the-loop applications [55]. Its integration with Simulink allows custom powertrain models and control algorithms to be incorporated into the simulation environment to enable safe and cost-effective verification and validation of dynamic models while accounting for system non-linearities and energy constraints.

3.1.1. Co-Simulation Architecture and Simulink Coder Plug-In Integration

The co-simulation workflow between IPG CarMaker and Simulink bridges custom powertrain and power supply logic with the full-vehicle environment through a Simulink Coder plugin model interface. IPG CarMaker acts as the master solver within this co-simulation structure by managing the virtual environment, tyre-road interaction, chassis dynamics, and the remaining vehicle subsystems. The compiled Simulink Coder plug-in runs simultaneously within this environment, receiving the real-time vehicle states required by the battery model, including the current demand and driver inputs, and returning the computed battery states to the powertrain model at each time step. This framework replaces the native CarMaker power supply subsystem with the developed battery model, allowing its behaviour to be evaluated under full-vehicle driving conditions.

3.1.2. CarMaker Baseline Architecture

IPG CarMaker provides vehicle model systems and applications supporting different hybrid architectures. The parallel hybrid powertrain configuration adopted in this study is shown in Figure 3.1, which represents the vehicle's electric system within the hybrid powertrain and its primary task is to account for the electric power flow to and between the electric circuits of the vehicle.

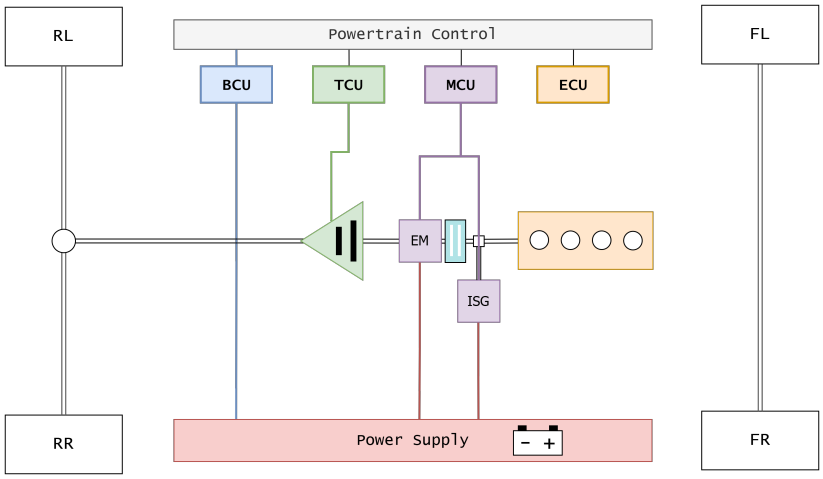


Figure 3.1: CarMaker Office Parallel Hybrid Configuration Overview with Rear Drive

The hybrid powertrain implemented in this study utilises a parallel P2 configuration, where the EM is positioned between the engine clutch and transmission which allows the ICE and EM to contribute to wheel torque independently or simultaneously while minimising added weight. Additionally, this layout supports powertrain control functionalities crucial for this study, including engine start/stop, regenerative braking, supplementary electric propulsion, and seamless mode transitions. The powertrain control strategy manages the operating states of the vehicle and dictates the distribution of both electrical and mechanical energy. This parallel powertrain is governed by its overarching controller strategy, electro-mechanical components, and dedicated control units shown in Figure 3.1, namely the Engine Control Unit (ECU) for the combustion engine, the Motor Control Unit (MCU) for the electric motors and integrated starter-generator, the Transmission Control Unit (TCU) for the gearboxes and clutches, and the BCU for the power supply.

3.2. CarMaker Chen Battery Model

The battery model reflects available energy storage of the power supply system and supplies voltage to drive the EM and integrated starter generator. IPG CarMaker implements a voltage supply model based on Chen and Rincon-Mora 2006 to predict runtime and current-voltage performance. The circuit diagram of the Chen model, illustrated in Figure 3.2, consists of an SOC-dependent open-circuit voltage in series with an internal resistance and two parallel RC branches. The voltage source U_{oc} represents the battery's idle voltage as a function of its SOC, while R_0 accounts for the instantaneous ohmic voltage drop due to internal resistance and the two RC branches, each consisting of a resistance and capacitance in parallel, represent the battery's transient electrochemical and diffusion dynamics, which captures the short and long term voltage behaviour observed during charge and discharge cycles.

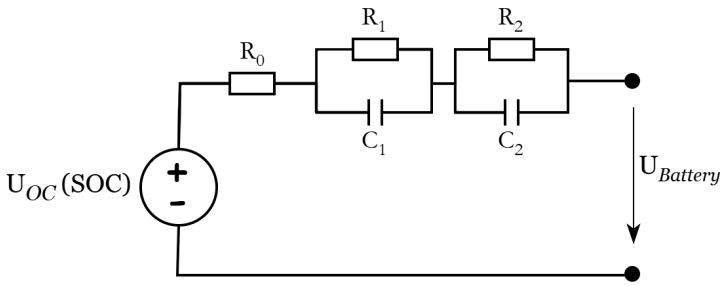


Figure 3.2: IPG CarMaker Battery Model "Chen"

3.2.1. Mathematical Description of Chen Battery Terminal Voltage

The terminal voltage of the Chen battery model is described mathematically as follows:

$$U_{\text{Battery}} = U_{oc}(\text{SOC}) - (I \cdot R_0) - U_1 - U_2 \tag{3.1}$$

$$U_1 = \int \left(\frac{I}{C_1} - \frac{U_1}{R_1 \cdot C_1} \right) dt \tag{3.2}$$

$$U_2 = \int \left(\frac{I}{C_2} - \frac{U_2}{R_2 \cdot C_2} \right) dt \tag{3.3}$$

where U_1 and U_2 are the voltages across the first and second RC branches respectively.

The Chen battery model provides a functional baseline that treats model parameters as static constants and only defines the OCV as a one-dimensional nonlinear function of SOC, illustrated in Figure 3.3. This limitation introduces cumulative errors, especially under high-load endurance racing conditions, which motivates the extension of the Chen battery model to a state-dependent 2^{nd} Order ECM.

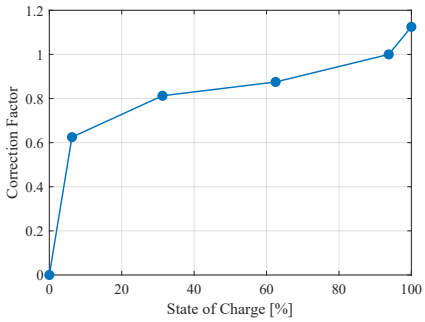


Figure 3.3: SOC non-linear correction factor applied to the Battery's OCV.

3.3. State Dependent 2^{nd} Order Equivalent Circuit Model

The HV battery model is represented by a state dependent 2^{nd} order ECM designed to accurately capture transient battery dynamics. The electrical circuit topology, shown in Figure 3.4, extends the baseline Chen model, in Figure 3.3, by incorporating additional complexity to better represent internal electrochemical processes. The model parameters R_0, R_1, C_1, R_2, C_2, and V_{OC} are implemented as multidimensional lookup tables varying dynamically with temperature, SOC, and current load. The ECM leverages discrete circuit elements to capture the nonlinear dynamic behaviour of the battery while mitigating computational demand for real-time feasibility. Nonlinear loss mechanisms are described through instantaneous ohmic voltage drop and slower polarisation losses, where the two RC branches account for short term transient charge double layer effects and long term solid state diffusion and concentration polarisation in series with the idle voltage.

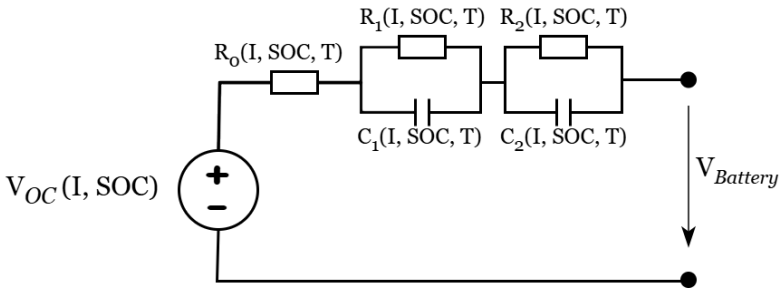


Figure 3.4: Higher Fidelity 2^{nd} Order Thévenin ECM

3.3.1. Mathematical Description of Battery State Behaviour

A complete representation of the battery system requires accurate tracking of its internal states and operational limits throughout a driving scenario. The quantified state behaviour of the battery system is represented by its terminal voltage, SOC, Amount of Charge (AOC), remaining energy capacity, electrical power, maximum charge/discharge power, and temperature, which collectively describe the battery's behaviour under dynamic charge and discharge cycles. The mathematical descriptions of the battery's states are presented below.

Instantaneous Battery Voltage

The terminal voltage of the battery pack is a nonlinear state defined by the OCV offset by the ohmic and polarisation voltage losses across the two RC branches. The state-dependent parameters are defined at the battery cell-level, therefore the OCV and RC parameters are scaled to the pack level. The instantaneous terminal voltage of state-dependent 2^{nd} Order ECM described mathematically below in Equation 3.4 is an extension of the terminal voltage for the simplified static parameter Chen battery model described in Equation 3.1.

$$V_{\text{Battery}} = V_{OC}(I, \text{SOC}) - I\frac{1}{n_p} \cdot R_0(I, \text{SOC}, T)\, n_s - V_1\, n_s - V_2\, n_s \tag{3.4}$$

where the dynamics of the two polarisation voltages, corresponding to the charge double-layer and diffusion polarisation mechanisms respectively, are governed by the following equations:

$$\frac{dV_1}{dt} = \frac{I}{C_1(I, \text{SOC}, T)} - \frac{V_1}{R_1(I, \text{SOC}, T) \cdot C_1(I, \text{SOC}, T)} \tag{3.5}$$

$$\frac{dV_2}{dt} = \frac{I}{C_2(I, \text{SOC}, T)} - \frac{V_2}{R_2(I, \text{SOC}, T) \cdot C_2(I, \text{SOC}, T)} \tag{3.6}$$

Instantaneous Battery State of Charge

The instantaneous SOC represents the remaining charge in the battery relative to its nominal capacity and is expressed as follows:

$$\text{SOC(t)} = \frac{Q(t)}{Q_n}$$

The SOC is tracked using Coulomb counting which measures the accumulated current flow out of the battery cell over time and is expressed as a percentage [%].

$$\text{SOC} = \text{SOC}_{\text{initial}} - \frac{1}{Q_C \cdot 3600} \int I \cdot dt \tag{3.7}$$

Current and voltage measurement errors as well as battery temperature and ageing typically affect Coulomb counting.

Instantaneous Amount of Charge

The instantaneous AOC represents the amount of energy at any time and is expressed in Ampere-hours [Ah]:

$$\text{AOC} = \text{SOC} \cdot Q_c \tag{3.8}$$

Battery Remaining Energy Capacity

The remaining energy capacity reflects the total usable energy stored in the battery at its current state, expressed in kilo-Watt hours [kWh].

$$E = V_{oc}(I, \text{SOC}) \cdot \text{AOC} \tag{3.9}$$

Total Electric Power on Electric Circuit

The instantaneous electrical power delivered by or supplied to the battery is calculated from the terminal voltage and battery current and expressed in Watts [W].

$$P_{\text{batt}} = V_{\text{Battery}} \cdot I \tag{3.10}$$

Maximum Charge/Discharge Power

The maximum allowable charge and discharge power of the battery is constrained by the maximum permissible current, I_{max}, which is limited to protect the cell from excessive current stress, and is calculated as follows:

$$P_{\text{max}} = V_{\text{Battery}} \cdot I_{\text{max}} \tag{3.11}$$

Unlike the constant maximum power rating assumed in the Chen baseline model, this quantity is treated as a dynamic value in the developed model, varying with the instantaneous terminal voltage as the battery's states and operating conditions change.

Battery Temperature

The temperature of the battery pack is a critical battery state that directly influences safety, degradation rates, system efficiency and output terminal voltage. To quantify the thermal dynamics, a transient thermal model is derived from the First Law of Thermodynamics and is applied to a closed battery pack system where the total energy of the isolated system is constant, meaning energy can neither be created nor destroyed, only transformed from one form to another. It can be expressed as the change in internal energy of a system being equal to the heat added to the system, subtracted by the work done by the system, which is described as:

$$\Delta U_{\text{net}} = \Delta Q_{\text{net}} - \Delta W_{\text{net}} \tag{3.12}$$

The thermal model is a mathematical representation that can be manipulated to describe the heat transfer and temperature distribution within the battery system which is necessary for thermal management to ensure safe operations, understanding the degradation phenomena under extreme operating conditions for lifespan and to optimise battery efficiency. The change in internal energy of the closed battery system is expressed in Equation 3.13 where the system does no work but only heat is added to the system.

$$\Delta U = \dot{Q}_{\text{gen}} + \dot{Q}_{\text{in}} + \dot{Q}_{\text{out}} \tag{3.13}$$

Equation 3.13 can be extended to the closed battery system and is expressed as:

$$C_{th} \frac{dT_{\text{batt}}}{dt} = \dot{Q}_{\text{gen}} + \dot{Q}_{\text{cool}} + \frac{T_{\text{amb}} - T_{\text{batt}}}{R_{\text{th}}} \tag{3.14}$$

where

$$C_{th} = m_c \cdot C_p \text{ and } R_{th} = \frac{1}{h \cdot n_s \cdot A}$$

The complete mathematical description for the battery temperature is expressed by Equation 3.15.

$$T_{\text{batt}} = T_{\text{batt}}(0) + \int_0^t \frac{1}{C_{\text{th}}} \left(\dot{Q}_{\text{gen}} + \dot{Q}_{\text{cool}} + \frac{T_{\text{amb}} - T_{\text{batt}}}{R_{\text{th}}} \right) dt \tag{3.15}$$

The internal heat generation term, $\dot{Q}_{\text{gen}}$, is evaluated based on the electrical parameters of the ECM:

$$\dot{Q}_{\text{gen}} = \dot{Q}_{\text{irreversible}} + \dot{Q}_{\text{reversible}} \tag{3.16}$$

The irreversible heat generation is driven by Joule heating due to internal resistance, while the reversible heat generation results from entropy changes during the electrochemical reactions. where

$$\dot{Q}_{\text{irreversible}} = I^2 R_0 + \frac{V_1^2}{R_1} + \frac{V_2^2}{R_2} \text{ and } \dot{Q}_{\text{reversible}} = I T_{batt} \frac{dV_{\text{OCV}}}{dT}$$

The heat transfer rate extracted by the coolant, $\dot{Q}_{\text{cool}}$, is an active cooling system that controls the temperature profile under extended, demanding racing profiles. It is dependent on the coolant mass flow rate and temperature rise across the cooling plate channel and is described as follows:

$$\dot{Q}_{\text{cool}} = \dot{m}_{\text{cool}}\, c_{p,\text{cool}}\, (T_{\text{c,out}} - T_{\text{c,in}}) \tag{3.17}$$

where the outlet coolant temperature is coupled to the state of the battery cell via the heat exchanger effectiveness factor, ϵ:

$$T_{\text{c,out}} = T_{\text{c,in}} + \epsilon\, (T_{\text{batt}} - T_{\text{c,in}})$$

therefore

$$\dot{Q}_{\text{cool}} = \dot{m}_{\text{cool}}\, c_{p,\text{cool}}\, \epsilon\, (T_{\text{batt}} - T_{\text{c,in}}) \tag{3.18}$$

3.4. Extended Battery Modelling Simulink Coder Plug-In Model

The mathematical descriptions of the underlying electrochemical dynamics are defined for both the static baseline model and the extended state-dependent 2$^{\text{nd}}$ Order ECM. Implemented in MATLAB/Simulink as a modular power supply plug-in for IPG CarMaker, the model structures the state-dependent parameter lookup tables, lumped thermal model, and derived battery state calculations as discrete subsystems interfaced through dedicated signal selectors. The state-dependent electric circuit parameters, obtained from industrial partners at TU Delft, are documented in Section A.1.1 of Appendix A.1 as functions of SOC, temperature, and current load. These parameters are implemented as 3D lookup tables within the 2$^{\text{nd}}$ Order ECM to extract data in real-time during simulation. The complete Simulink model architecture is presented in Section A.1.2 of Appendix A.1.

Upon simulation initialization, the model loads the battery's total capacity, idle voltage, and initial SOC. During runtime, it receives pack current, coolant inlet temperature, and coolant mass flow rate from the BCU, and outputs standard PTBattery signals: instantaneous voltage, SOC, AOC, remaining energy, maximum available power, and temperature. Co-simulation within CarMaker captures dynamic vehicle power demand and enables model validation. By incorporating state-dependent parameters and coupled thermal dynamics, the extended model achieves high electro-thermal fidelity while remaining computationally efficient for real-time implementation, operating alongside the developed BCU and energy management strategies under representative hybrid endurance racing conditions.

3.5. Battery Modelling Conclusion

In this chapter, an advanced state-dependent 2$^{\text{nd}}$ order ECM for the HV battery system is formulated and integrated into IPG CarMaker as an executable Simulink Coder plug-in. The pack is represented as a single lumped model scaled to a 96-series, 4-parallel (96s4p) cell configuration, assuming uniform heating behaviour without accounting for cell-to-cell variations, internal nodal dynamics, or localized thermal gradients. By capturing RC and OCV parameter variations through 3D lookup tables dependent on SOC, temperature, and current load, the model robustly resolves nonlinear electro-thermal dynamics and transient losses with minimal computational overhead. This validated battery plant model establishes the foundation for the following chapter, which details the BCU control and estimation architectures, including real-time state estimation, active thermal management, and high-level energy management within the hybrid powertrain.

4

Controller Strategy Development

The state-dependent 2nd Order ECM established in Chapter 3 forms the basis for the control and estimation algorithms developed in this chapter to manage the HV battery system and optimise its integration within the parallel hybrid powertrain configuration. Section 4.1 establishes the state estimation framework using a coupled three-state EKF, augmented with a parameter correction filter to account for parameter degradation under repeated high charge-discharge cycles while providing real-time SOC feedback. Section 4.2 addresses thermal management, where the controller regulates coolant flow to maintain safe operating temperatures under sustained high-power requests. Finally, Section 4.3 presents the energy management strategy, which governs the hybrid powertrain operating modes. These developed strategies form a coordinated framework for state, thermal, and energy management, validated within the IPG CarMaker simulation environment.

4.1. State Estimation

Accurate estimation of battery SOC is essential for extending battery life, maximising energy utilisation, and ensuring operational safety [30], which are critical in hybrid endurance racing where high precision is required to achieve peak performance. The extended state-dependent HV battery model relies on Coulomb counting to estimate the battery state. However, Coulomb counting lacks robustness as it neglects dynamic thermal variations and sensor bias, leading to cumulative drift errors over extended operating periods [34]. To prevent state estimation errors from corrupting state-dependent RC parameter and OCV lookups and further misrepresenting battery states, a coupled four-state EKF is proposed and implemented.

4.1.1. Recursive State Estimation Algorithm Framework

The baseline state estimation framework is adapted from the MATLAB & Simulink Battery State-of-Charge Estimation example [57]. While the original implementation utilises a standard extended Kalman filter structure, this work extends the framework by introducing state-dependent parameters and expanding the state vector to include a fourth thermal state for coupled electro-thermal tracking. The framework of the proposed coupled four-state EKF algorithm is illustrated in Figure 4.1, following the two-phase prediction-correction structure of the implemented EKF.

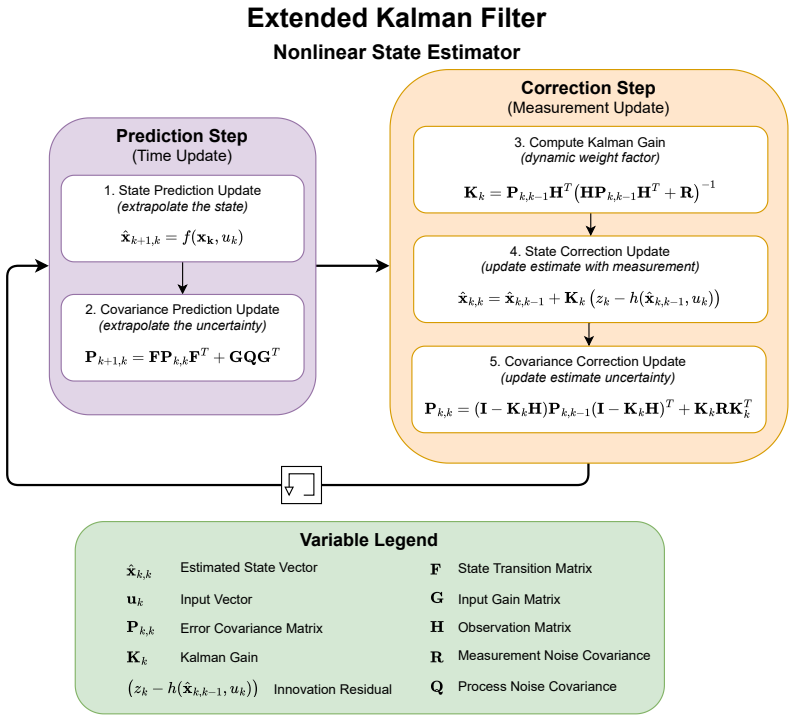


Figure 4.1: Schematic of Extended Kalman Filter Operation

In the prediction step, the current state estimate $\hat{\mathbf{x}}_{k,k}$ and its uncertainty covariance $\mathbf{P}_{k,k}$ are propagated forward using the process model, producing the state estimate $\hat{\mathbf{x}}_{k+1,k}$ and covariance estimate $\mathbf{P}_{k+1,k}$ along with their associated uncertainties. The Kalman gain $\mathbf{K}_k$ serves as a dynamic weighting factor, adjusting the state estimate based on the innovation residual between the predicted and measured output. The innovation residual is described by the terminal voltage measurement error, which is corrupted by both current and voltage sensor noise. The state estimate and covariance are then corrected by balancing prior state uncertainty against measurement noise via the Kalman gain. These corrected estimates $\hat{\mathbf{x}}_{k,k}$ and $\mathbf{P}_{k,k}$ subsequently feed back into the next prediction step, forming a recursive estimation loop.

4.1.2. State Estimation Algorithm

The EKF is an extension of the Kalman Filter for nonlinear systems, and is a recursive state estimator capable of real-time operation, where the current input measurements, the previously estimated states, and their associated uncertainty covariance matrix are required to determine the present state. To implement the EKF algorithm, the developed state-dependent battery ECM is expressed in non-linear state-space form. By combining a series of noisy and uncertain measurements over time, the algorithm produces a state estimate that is more accurate than one obtained from any single sensor measurement or coulomb counting alone.

System State-Space Formulation

In real-world systems, the process and measurement models are nonlinear. The states of the system are estimated by linearising the nonlinear process and measurement models around the current state estimates. The dynamic behaviour of the battery is estimated via the state vector, x_k, the control input vector u_k and the measurement vector y_k described as follows:

$$\mathbf{x}_k = \begin{bmatrix} \mathrm{SOC}_k & T_k & V_{1,k} & V_{2,k} \end{bmatrix}^T, \quad \mathbf{u}_k = \begin{bmatrix} I_k & \dot{m}_{\mathrm{cool},k} \end{bmatrix}^T, \quad y_k = V_{\mathrm{batt},k} \tag{4.1}$$

The propagation of the state vector is governed by the nonlinear process function $f(\mathbf{x}_k, \mathbf{u}_k)$, which describes the rate of change of state vector x_k, while the terminal battery voltage is obtained from the nonlinear observation function $h(\mathbf{x}_k, \mathbf{u}_k)$ where all state-dependent parameter quantities are implicitly time-dependent. The nonlinear process function is defined as follows:

$$f(\mathbf{x}_k, \mathbf{u}_k) = \begin{bmatrix} SOC_{k+1} \\ T_{k+1} \\ V_{1,k+1} \\ V_{2,k+1} \end{bmatrix} = \begin{bmatrix} SOC_k - \frac{\Delta t \cdot I_k}{q_c} \\ T_k + \frac{\Delta t}{C_{th}} \left(Q_{gen,k} + Q_{cool,k} - \frac{1}{R_{th}} (T_k - T_{amb}) \right) \\ V_{1,k} e^{-\Delta t/\tau_1} + R_1 I \left(1 - e^{-\Delta t/\tau_1}\right) \\ V_{2,k} e^{-\Delta t/\tau_2} + R_2 I \left(1 - e^{-\Delta t/\tau_2}\right) \end{bmatrix} \tag{4.2}$$

where the state-dependent time constants are defined by:

$$\tau_1 = R_1(I, SOC, T) \cdot C_1(I, SOC, T) \tag{4.3}$$

$$\tau_2 = R_2(I, SOC, T) \cdot C_2(I, SOC, T) \tag{4.4}$$

and the measurement function is defined as follows:

$$h(\mathbf{x}_K, \mathbf{u}_k) = V_{batt,k} = V_{oc}(I, \mathrm{SOC}) - \frac{I}{n_p} \cdot R_0(I, \mathrm{SOC}, T) - n_s V_1 - n_s V_2 \tag{4.5}$$

Jacobian Matrices

The EKF algorithm relies on linearisation at every time step k to approximate the nonlinear battery dynamics. For the prediction step, the process function is linearised about the current corrected state estimate $\hat{\mathbf{x}}_{k,k}$ and input vector $\mathbf{u}_k$ to yield the state transition Jacobian matrix $\mathbf{F}_k$ and the input gain Jacobian matrix $\mathbf{G}_k$. Subsequently, the measurement function is linearised about the predicted state estimate $\hat{\mathbf{x}}_{k+1,k}$ to obtain the observation Jacobian matrix $\mathbf{H}_k$ required for the correction step. The state transition matrix $\mathbf{F}_k$ describes how each state affects its future states and is derived analytically as follows:

$$\mathbf{F}_k = \frac{\partial f(\mathbf{x}_k, \mathbf{u}_k)}{\partial \mathbf{x}_k} = \begin{bmatrix} 1 & 0 & 0 & 0 \\ f_{21} & f_{22} & f_{23} & f_{24} \\ 0 & 0 & e^{-\Delta t/\tau_1} & 0 \\ 0 & 0 & 0 & e^{-\Delta t/\tau_2} \end{bmatrix} \tag{4.6}$$

where the highly coupled thermal derivative elements in the second row are defined as follows:

$$f_{21} = \frac{\partial T_{k+1}}{\partial SOC_k} = \frac{\Delta t}{C_{th}} \left(\frac{I}{n_p}^2 \frac{\partial R_0}{\partial SOC} \right) \tag{4.7}$$

$$f_{22} = \frac{\partial T_{k+1}}{\partial T_k} = 1 + \frac{\Delta t}{C_{th}} \left(\frac{I}{n_p}^2 \frac{\partial R_0}{\partial T} + \frac{\partial OCV}{\partial T} I - \frac{1}{R_{th}} - \dot{m}_{cool,k} \cdot c_{p,c} \cdot \epsilon \right) \tag{4.8}$$

$$f_{23} = \frac{\partial T_{k+1}}{\partial V_{1,k}} = \frac{\Delta t}{C_{th}} \left(\frac{2 n_s V_{1,k}}{R_1} \right) \tag{4.9}$$

$$f_{24} = \frac{\partial T_{k+1}}{\partial V_{2,k}} = \frac{\Delta t}{C_{th}} \left(\frac{2 n_s V_{2,k}}{R_2} \right) \tag{4.10}$$

The input gain matrix $\mathbf{G}_k$ maps the input current $u_k = I_k$ directly onto the state derivatives as follows:

$$\mathbf{G}_k = \frac{\partial f(\mathbf{x}_k, \mathbf{u}_k)}{\partial \mathbf{u}} = \begin{bmatrix} -\frac{\Delta t \cdot \eta}{q_c} & 0 \\ \frac{\Delta t}{C_{th}} \left(\frac{2 I R_0}{n_p{}^2} + \frac{I}{n_p}^2 \frac{\partial R_0}{\partial I} + \frac{\partial OCV}{\partial T} T_k \right) & \frac{\Delta t}{C_{th}} \left(c_{p,c} \epsilon (T_{cool} - T_k) \right) \\ R_1 \left(1 - e^{-\Delta t/\tau_1}\right) & 0 \\ R_2 \left(1 - e^{-\Delta t/\tau_2}\right) & 0 \end{bmatrix} \tag{4.11}$$

The observation matrix $\mathbf{H}_k$ is the Jacobian of the measurement function, evaluated at each time step:

$$\mathbf{H}_k = \frac{\partial h}{\partial \mathbf{x}} = \begin{bmatrix} \frac{\partial V_{oc}}{\partial z} - \frac{I_k}{n_p}\frac{\partial R_0}{\partial SOC} & -\frac{I_k}{n_p}\frac{\partial R_0}{\partial T} & -n_s & -n_s \end{bmatrix} \tag{4.12}$$

4.1.3. Covariance Matrix Parametrization

To account for real-world sensor characteristics, synthetic zero-mean Gaussian white noise v_k is injected into the ideal current, terminal voltage, and temperature signals according to:

$$v_k = w_k \sqrt{\frac{P_n}{T_s}} \tag{4.13}$$

where $w_k \sim \mathcal{N}(0,1)$ represents a standard normal random variable, $P_n = 10^{-2}$ is the noise power, and $T_s = 0.001\,\text{s}$ is the discrete simulation time step. Corrupting these ideal feedback signals provides a realistic simulation environment to evaluate the tracking accuracy and noise rejection performance of the EKF. To stabilise the state estimator during aggressive driving cycles, the filter covariance matrices ($\mathbf{P}_0$, $\mathbf{Q}$, and $\mathbf{R}$) are tuned to balance trust between physical model predictions and the noisy sensor feedback.

Initial Error Covariance Matrix ($\mathbf{P}_0$)

The initial error covariance is set to $\mathbf{P}_0 = \text{diag}\left(\left[10^{-6}, 10^{-6}, 10^{-3}, 10^{-3}\right]\right)$, corresponding to the state vector $\mathbf{x}_k = [\text{SOC}_k,\, T_k,\, V_{1,k},\, V_{2,k}]^T$. The small initial uncertainties reflect high confidence in the initial state estimates at $t = 0$, preventing aggressive or unstable filter corrections during the first few simulation time steps.

Process Noise Covariance Matrix (Q)

The process noise covariance matrix accounts for system model simplifications and sensor noise on the control inputs $\mathbf{u}_k = [I_k,\, \dot{m}_{\text{cool},k}]^T$. The covariance is defined as $\mathbf{Q} = \text{diag}\,([0.01,\, 0.05])$, where 0.01 corresponds to input current variance and 0.05 to coolant mass flow rate variance. This configuration enables the EKF to correct for CC integration drift during current transients without over-reacting to short-term input noise or causing phase lag during aggressive driving manoeuvres.

Measurement Noise Covariance Matrix (R)

The measurement noise covariance matrix accounts for instrument noise across the feedback channels $\mathbf{y}_k = [V_{\text{batt},k},\, T_{\text{casing},k}]^T$. The covariance is defined as $\mathbf{R} = \text{diag}\,([0.5,\, 0.01])$, where 0.5 corresponds to terminal voltage variance and 0.01 to casing temperature variance. This configuration enables the EKF to filter high-frequency electrical noise, relying heavily on model physics (RC transient dynamics and state-dependent OCV lookups), while compensating for spatial gradient simplifications in the lumped-parameter thermal model.

4.1.4. Implementation of State Estimation in Coordinated Framework

The discrete four-state EKF is integrated within the CarMaker for Simulink (CM4SL) co-simulation environment at a fixed step time of $T_s = 0.001\,\text{s}$ (1 kHz). The complete subsystem-level layout and execution chain are provided in Appendix A.2. Operating within this coordinated framework, the filter updates the full state vector at each time step, supplying noise-filtered SOC and temperature estimates directly to the high-level energy and thermal management controllers.

4.2. State of Health Estimation

Accurate SOC estimation is essential for reliable SOH prediction, directly influencing battery safety, lifespan, and system stability. A dual-estimator architecture is employed, in which the four-state EKF presented in Section 4.1 estimates dynamic internal states while a secondary filter updates key model parameters in real time.

4.2.1. State Estimation using Power Fade

In battery management systems, SOH is generally categorised into two primary degradation mechanisms, namely capacity fade and power fade. Capacity fade tracks the loss of total energy storage capability. However, power fade characterises the increase in the internal ohmic resistance, R_0, of the cell due to ageing factors such as SEI layer growth and active material isolation. This is particularly relevant to the present study to effectively capture the electrochemical degradation, since R_0 is treated as a state-dependent parameter varying with SOC, temperature, and current load, and its drift over the SOH directly affects the accuracy of the ECM, the usable service life of the battery, and its safety limits.

For this study, the SOH estimation is formulated around power fade rather than capacity fade. In hybrid endurance racing applications, the battery operates within a relatively narrow usable SOC window and is primarily subjected to aggressive, transient power demands during dynamic acceleration and regenerative braking. Under these high-rate conditions, an increase in internal resistance significantly limits the power delivery capability. Furthermore, while capacity is practically unobservable, resistance is highly observable under dynamic excitation, making it suitable for online SOH estimation. The resistance-based SOH is defined as the ratio of the currently estimated resistance to the baseline resistance of a new battery cell:

$$SOH_R(t) = \frac{R_0(t)}{R_{0,\text{fresh}}} \tag{4.14}$$

4.2.2. Parameter Correction Filter Implementation

The battery's degradation associated with power fade is tracked via a parameter state vector, $\boldsymbol{\theta}_k$. The parameter state, the input vector $\mathbf{u}_k$, and the measurement vector y_k are described as follows:

$$\boldsymbol{\theta}_k = \left[k_{R0,k}\right], \quad \mathbf{u}_k = [I_k], \quad y_k = \left[V_{batt,k}\right] \tag{4.15}$$

The propagation of the parameter state vector is governed by a linear process function, $f_\theta(\boldsymbol{\theta}_k)$, treating degradation as a slow-varying process relative to fast state dynamics. The nonlinear observation function, $h_\theta(\boldsymbol{\theta}_k, \mathbf{u}_k, \mathbf{x}_k)$, maps this internal health scaling factor and state vector to the physical terminal voltage. The parameter process and observation equations are defined as follows:

$$f_\theta(\boldsymbol{\theta}_k) = k_{R0,k} \tag{4.16}$$

$$h_\theta(\boldsymbol{\theta}_k, \mathbf{u}_k) = OCV(\text{SOC}_k) - I_k \cdot (R_0 \cdot k_{R0,k}) - V_{1,k} - V_{2,k} \tag{4.17}$$

The state transition matrix $F_\theta = 1$ and input gain matrix $G_\theta = 0$ define stationary parameter propagation between sample steps, therefore the degradation estimator relies entirely on sensor feedback. The observation matrix $H_{\theta,k}$ quantifies terminal voltage sensitivity to the scaling factor k_{R_0}. As internal resistance increases with ageing, the resulting voltage tracking error drives the recursive Kalman update to adjust k_{R_0} in real time.

$$H_{\theta,k} = \frac{\partial h_\theta}{\partial \theta} = -I_k \cdot R_0 \tag{4.18}$$

4.2.3. Implementation of Degradation in Coordinated Framework

The single-parameter SOH filter operates alongside the primary four-state EKF to dynamically estimate internal resistance degradation via the scaling factor k_{R_0}. The measurement noise ($R = 10$) is set significantly higher than the process noise ($Q = 10^{-9}$), therefore the parameter estimator behaves similar to a low-pass filter. It actively ignores the rapid, erratic voltage spikes caused by aggressive driving and only responds to the slow, permanent voltage shift errors caused by actual battery degradation. This architecture, shown in Appendix A.2, successfully decouples slow physical battery aging from high-frequency driving transients, ensuring stable parameter adaptation and continuous propagation of corrected model parameters.

4.3. Battery Thermal Management System

An effective BTMS is essential to maintain the battery within its optimal operating temperature range while ensuring uniform thermal distribution across cells and modules. Batteries operating well outside optimal ranges can be detrimental to the battery health where this can lead to thermal runaway that presents a significant safety risk. However, lower temperatures lead to an increase in internal resistance and a decrease in capacity which compromises the overall powertrain performance. This section details the thermal plant model, dynamic coolant properties, and the control strategy designed to maintain target operating temperatures.

4.3.1. Battery Thermal Representations

The lumped thermal energy balance for the battery, in Section 3.3, is rearranged to isolate the state derivative:

$$\dot{T}_{batt} = -\frac{1}{C_{th}}\left(\frac{1}{R_{th}} + \dot{m}_{cool}c_{p,cool}\varepsilon\right)T_{batt} + \frac{\dot{Q}_{gen}}{C_{th}} + \frac{\dot{m}_{cool}c_{p,cool}\varepsilon}{C_{th}}T_{c,in} + \frac{T_{amb}}{C_{th}R_{th}} \tag{4.19}$$

The thermal model exhibits bilinear coupling between the state and control input via the convective term $\dot{m}_{\text{cool}}T_{\text{batt}}$. This inherent nonlinearity prevents simple controllers, such as standard PID, from performing reliably across the entire operating range. To manage this nonlinearity while enforcing strict physical boundaries, MPC is implemented due to its ability to directly handle input, output, and state constraints. By optimising a predictive cost function over a rolling horizon, the controller proactively anticipates required cooling actions which is particularly valuable under the dynamic, high-rate drive cycles expected in endurance racing.

4.3.2. Coolant Mass Flow Rate Properties

Controlling the temperature of a battery via forced convection is an inherently nonlinear problem. From the energy balance equation it is known that the specific heat capacity, $c_{p,cool}$, and the heat exchanger effectiveness, ε, are not constant but highly dependent on the environment. The specific heat capacity varies with the coolant temperature, whereas the effectiveness varies with both the coolant temperature and the mass flow rate. This subsection details the coolant selected, the temperature-dependent properties used in the model, and the method by which the heat exchanger effectiveness is obtained.

Coolant Fluid Properties and Heat Exchanger Effectiveness

The thermal management system utilises a 50% by volume Ethylene Glycol solution from DOWTHERM [58] which provides an optimal balance of thermal conductivity, extended temperature limits and corrosion resistance which are critical for managing the thermal dynamics experienced during endurance racing cycles. The saturation properties are evaluated as functions of the battery temperature:

$$\left[c_{p,cool},\ \rho_{cool},\ k_{cool},\ \mu_{cool}\right] = f\left(T_{batt}\right) \tag{4.20}$$

The Prandtl number expresses the ratio of momentum diffusivity to thermal diffusivity and is given as:

$$\text{Pr} = \frac{c_{p,cool}\,\mu_{cool}}{k_{cool}} \tag{4.21}$$

The cooling plate is represented as a set of rectangular channels of width w_c and depth d_c. The cross-sectional area, wetted perimeter and hydraulic diameter of a single channel are given by:

$$A_c = w_c d_c, \qquad P_w = 2\left(w_c + d_c\right), \qquad D_h = \frac{4A_c}{P_w} \tag{4.22}$$

The total heat transfer area presented to the coolant is determined by the cell length L_{cell}, the channel width and the number of cells in series,

$$A_{ht} = n_s L_{cell}\, w_c \tag{4.23}$$

The Reynolds number for an individual coolant channel is calculated as:

$$\mathrm{Re} = \frac{\dot{m}_{cool} D_h}{n_p A_c \mu_{cool}} \tag{4.24}$$

In the turbulent regime the Nusselt number is obtained from the Dittus-Boelter correlation:

$$\mathrm{Nu} = 0.023\,\mathrm{Re}^{0.8}\,\mathrm{Pr}^{0.3} \tag{4.25}$$

The convective heat transfer coefficient is obtained from the Nusselt number as follows:

$$h_{cool} = \frac{\mathrm{Nu}\, k_{cool}}{D_h} \tag{4.26}$$

Finally, the number of transfer units and the resulting heat exchanger effectiveness are given as follows:

$$\mathrm{NTU} = \frac{h_{cool} A_{ht}}{\dot{m}_{cool} c_{p,cool}}, \qquad \varepsilon = 1 - e^{-\mathrm{NTU}} \tag{4.27}$$

4.3.3. Thermal Management Controller Implementation

Standard Linear Time-Invariant (LTI) control theory requires the system to be written in the state-space form $\dot{x} = Ax + Bu$. However, the thermal plant is nonlinear due to the bilinear coupling of the system state and control input. Therefore, linearising the model at a fixed operating condition causes a loss in prediction accuracy. Although Nonlinear MPC addresses this issue, its underlying non-convex optimisation is computationally expensive and complicates finding the global optimum. Alternatively, the plant can be modelled using Linear Parameter-Varying (LPV) embedding, which bridges nonlinear and LTI control formulations by keeping the system model linear in the state space but parameter-dependent in the system matrices. As highlighted by Morato et al. [59], this representation captures essential non-linearities while avoiding the heavy computational burden of Nonlinear MPC. By framing the system as pseudo-linear at each time step, the control objective is reduced to a standard quadratic cost function. When paired with a streamlined control horizon, this enables the optimal control law to be computed via a closed-form algebraic expression, bypassing the need for iterative numerical solvers. Furthermore, integrating a dynamic disturbance estimator directly mitigates the real-time set-point tracking errors caused by unmodelled disturbances and parameter uncertainties.

Parameter-Varying Discretisation

The prediction model is updated at each time step by evaluating the pseudo-linear matrices A_c and B_c, obtained from Equation 4.19, using the previous actuator state, $\dot{m}_{\mathrm{prev}}$:

$$A_c = -\frac{1}{C_{th}}\left(\frac{1}{R_{th}} + \dot{m}_{prev} c_{p,cool}\varepsilon\right), \quad B_c = \begin{bmatrix} \frac{1}{C_{th}} & \frac{\dot{m}_{prev} c_{p,cool}\varepsilon}{C_{th}} & \frac{1}{C_{th} R_{th}} \end{bmatrix} \tag{4.28}$$

The continuous model is discretised at each time step T_s using exact Zero-Order Hold to obtain the following discrete prediction matrices:

$$A_d = e^{A_c T_s}, \quad B_d = \frac{B_c}{A_c}\left(e^{A_c T_s} - 1\right) \tag{4.29}$$

Dynamic Disturbance Estimator

To prevent steady-state errors caused by plant-model mismatch, a dynamic disturbance estimator computes the residual between the measured battery temperature ($T_{\mathrm{batt},k}$) and the prior predicted state ($\hat{x}_{k|k-1}$) shown below. This residual is processed through a discrete first-order low-pass filter using a 95/5 weighting ratio, suppressing high-frequency sensor noise while capturing genuine thermal drift. The resulting offset, d_{filt}, is applied uniformly across all steps of the prediction horizon to align model predictions with physical measurements and guarantee offset-free tracking.

$$d_{filt,k} = 0.95 \cdot d_{filt,k-1} + 0.05 \cdot (T_{batt,k} - \hat{x}_{k|k-1}) \tag{4.30}$$

Dynamic Reference Trajectory

A dynamic reference trajectory is implemented to enforce a smooth approach to the target temperature, preventing overshoot and oscillatory behaviour. Without this trajectory, the controller reacts abruptly when the target temperature is reached, commanding maximum coolant flow and causing the battery temperature to drop too rapidly, which forces the actuator to cycle on and off rather than maintain a steady control action. This aggressive behaviour reduces the algorithm to a basic rule-based thermostat and ignores the predictive advantages of MPC. To eliminate these oscillations around the setpoint, an activation temperature threshold (T_{activate}) initiates a ramped trajectory before the target temperature is reached:

$$T_{\text{ref}}(i) = \min\left(T_{\text{activate}} + i \cdot \Delta T_{\text{ramp}},\ T_{\text{trg}}\right) \tag{4.31}$$

where $T_{\text{activate}} = T_{\text{trg}} - 0.5\,^{\circ}\text{C}$, i is the prediction step index, and ΔT_{ramp} is the allowable thermal rate ($0.005\,^{\circ}\text{C}$).

Closed-Form Algebraic Optimisation

The response time of the coolant actuator is notably faster than the thermal dynamics of the battery pack. Therefore, to fundamentally simplify the optimization problem, the control horizon is restricted to a single step ($m = 1$). This configuration eliminates the need for iterative numerical solvers to evaluate multi-variable matrices, allowing the optimal actuator command to be directly derived through a closed-form algebraic expression. To formulate this expression, the predicted trajectory over the horizon is decomposed into two distinct components: the free response and the step response. The free response, denoted by X_{free}, represents the baseline thermal trajectory, predicting future battery temperatures under the assumption that the current coolant flow rate remains constant. Conversely, the step response, denoted by S, quantifies the isolated thermal effect of varying the coolant flow rate. The tracking error (E) over the entire prediction horizon ($p = 60$) is used to calculate the precise control effort required to reach the target temperature. It is defined as the difference between this free baseline response and the dynamic reference trajectory:

$$E = X_{free} - T_{ref} \tag{4.32}$$

The unconstrained control action, ΔU, is computed analytically by minimising this tracking error and is given in Equation 4.33. To prevent aggressive actuator transients, a dimensionless effort penalty, β, is incorporated to heavily penalise rapid fluctuations in the coolant mass flow rate. Additionally, a minimal regularisation term, ϵ, is introduced in the denominator to prevent numerical singularities, which ensures computational stability during controller initialisation:

$$\Delta U = -\frac{S^T E}{(1+\beta)(S^T S) + \epsilon} \tag{4.33}$$

Finally, to protect the physical hardware, this unconstrained control action must be saturated before being commanded to the actuator. The change in flow rate is bounded by the maximum permissible rate of change ($\Delta \dot{m}_{max}$), and the absolute command is restricted strictly within its physical operating limits:

$$\Delta U_{sat} = \max\left(\min(\Delta U, \Delta \dot{m}_{max}), -\Delta \dot{m}_{max}\right) \tag{4.34}$$

$$\dot{m}_{cool} = \max\left(\min(\dot{m}_{prev} + \Delta U_{sat}, \dot{m}_{max}), \dot{m}_{min}\right) \tag{4.35}$$

The presented BTMS architecture effectively manages the nonlinear thermal dynamics of the battery model. The LPV model updates its parameters dynamically to keep predictions accurate across the entire operating range, while the MPC calculates the optimal coolant flow rate in a single time step while respecting physical actuator limits. Co-simulation of the BTMS within CM4SL is integrated into the BCU architecture detailed in Figure 3(g) in Appendix A.2 and the single-move LPV-MPC algorithm is implemented as a MATLAB Function, with the full source code provided in Appendix A.2.2.

4.4. Powertrain Energy Management Strategy

The supervisory powertrain controller, referred to as PTControl within IPG CarMaker's simulation environment, executes the superordinated energy management strategy. The control model interprets the driver's torque demand alongside the current battery state and driving mode, allocating torque requests between the ICE and EM. This section presents a rule-based Finite-State Machine (FSM) adapted from a standard parallel hybrid control strategy and parametrised to enforce charge-sustaining behaviour that guarantees continuous regenerative braking and electric boost availability over 24-hour race stints.

4.4.1. Endurance Powertrain Control Architecture

The mechanical energy management module operates as a prioritised, rule-based FSM that determines the active strategy mode and distributes torque demand between the ICE and EM. The supervisory controller evaluates operating conditions against predefined state transition boundaries, utilising hysteresis bands to prevent high-frequency mode oscillations around threshold limits. The powertrain strategy modes and their priority hierarchy are configured for a rear-wheel-drive, two-clutch (P2) parallel hybrid architecture which is illustrated in Figure 4.2 and detailed in Appendix A.2.3 [55].

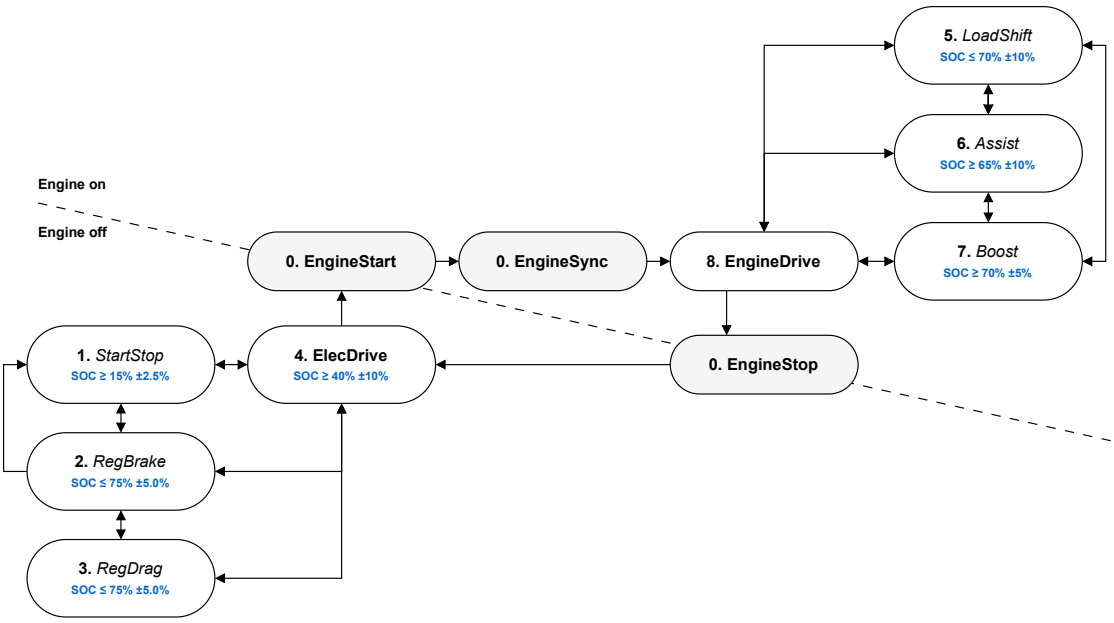


Figure 4.2: Hybrid endurance parallel P2 powertrain PTControl strategy modes

The primary control objective for endurance racing is maintaining charge-sustaining equilibrium to prevent HV battery depletion. Discharging the battery to its lower cutoff limit triggers a protective disconnection that abruptly eliminates electric propulsion and regenerative braking which compromises vehicle deceleration and track safety. To prevent this, the supervisory controller parametrises the strategy modes around an HV battery SOC target of 75%. Energy-depleting deployment modes, namely through Boost and Assist, are restricted to higher charge levels, with pure electric driving, ElecDrive, disabled below $40\% \pm 10\%$. Energy recovery modes, namely RegBrake and RegDrag, engage as SOC drops to recover kinetic energy up to $75\% \pm 5.0\%$, while LoadShift provides active ICE generation. The closed-loop boundaries presented in the rule-based FSM are parametrised to maintain the HV battery state within a stable operational window lap after lap.

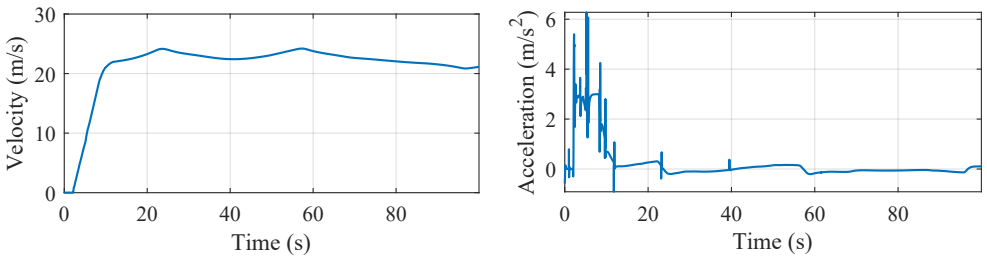
5

Simulations and Results

This chapter presents the simulation framework and evaluates the performance of the developed HV Li-ion battery model. The co-simulation architecture and integration within IPG CarMaker are established by examining baseline Chen battery responses with and without SOC dependence, after which the state-dependent 2^{nd} Order ECM is extended to accurately represent real-world dynamics as the foundation for advanced controller algorithms to optimise overall racing performance. Preliminary validation is performed using the Assessment and Reliability of Transport Emission Models and Inventory Systems (ARTEMIS) driving cycle to benchmark the conventional energy management strategies against the proposed hybrid control framework detailed in Section 4.4. Finally, the integrated battery management system is evaluated under endurance racing scenarios to assess long-term electro-thermal dynamics and overall powertrain performance.

5.1. Battery Model Integration and Validation in IPG CarMaker

The static-parameter HV battery model developed in Section 3.2 is validated by integrating in IPG CarMaker and benchmarking it against the default Chen battery model. Model validation is conducted using a test run driving scenario, shown in Figure 5.1, that presents a parallel hybrid configuration, shown in Figure 3.1, travelling up and down the Bernina Pass in Switzerland. Along this route, the engine drive, electric drive and regenerative braking operating modes of the powertrain control strategy can all be observed. The battery discharges on the ascent and recharges on the descent, producing sustained high-current discharge and recharge phases in a single cycle which is appropriate to evaluate the battery's dynamic response.



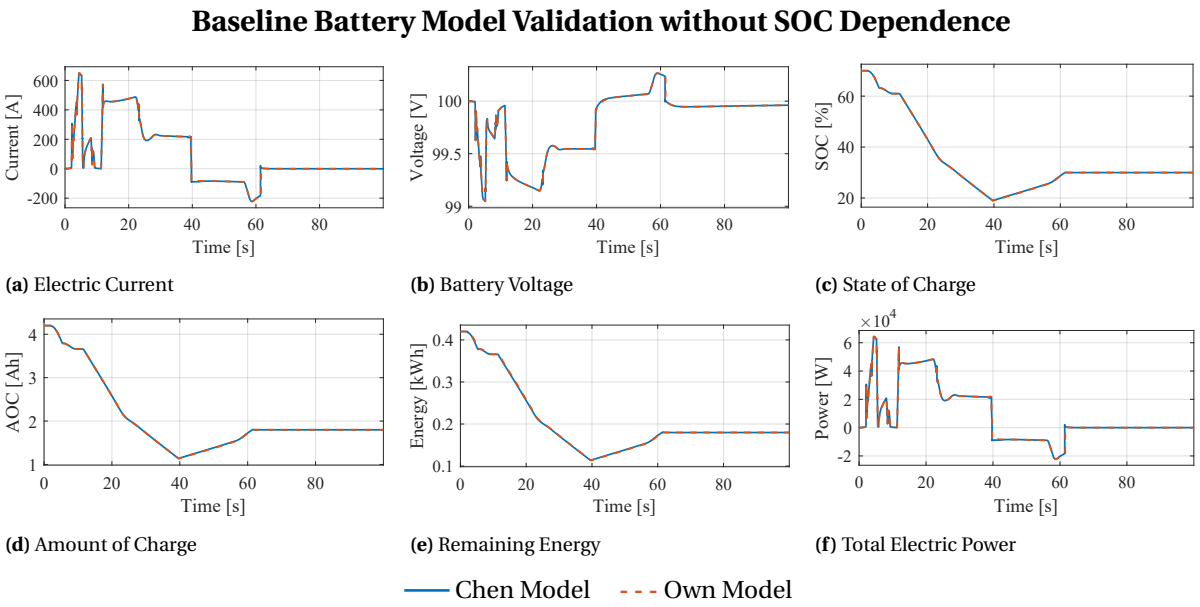
(a) Vehicle velocity

(b) Vehicle acceleration

Figure 5.1: CarMaker vehicle driving profile for the mountain driving cycle.

5.1.1. Battery Model Baseline Response without SOC Dependence

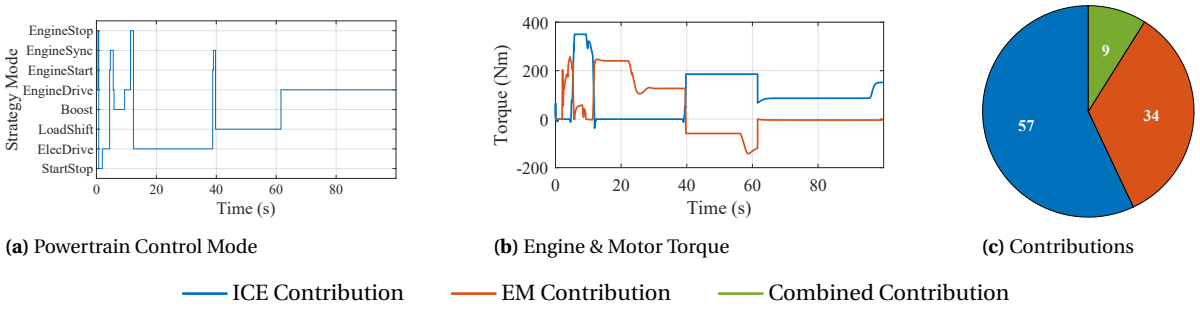
Simulation within IPG CarMaker captures the dynamic contribution of the vehicle demand on the battery and enables validation of the developed battery model against CarMaker's Chen Battery Model. The developed static-parameter 2nd Order ECM replicates the dynamic response of the Chen Battery Model and is validated as indicated in Figure 5.2. The 2nd Order ECM depicted here uses static circuit parameters, such that the idle OCV, resistor and capacitor values remain constant throughout the simulation. The results indicate that the mathematical representation described by the 2nd Order ECM replicates the Chen Battery Model, where their respective dynamic response are identical over the full duration of the drive cycle. The powertrain modes and their respective power supply contributions are provided in Figure 5.3.



(a) Electric Current **(b)** Battery Voltage **(c)** State of Charge

(d) Amount of Charge **(e)** Remaining Energy **(f)** Total Electric Power

Figure 5.2: Chen battery dynamic response of developed 2nd Order ECM without SOC dependence



(a) Powertrain Control Mode **(b)** Engine & Motor Torque **(c)** Contributions

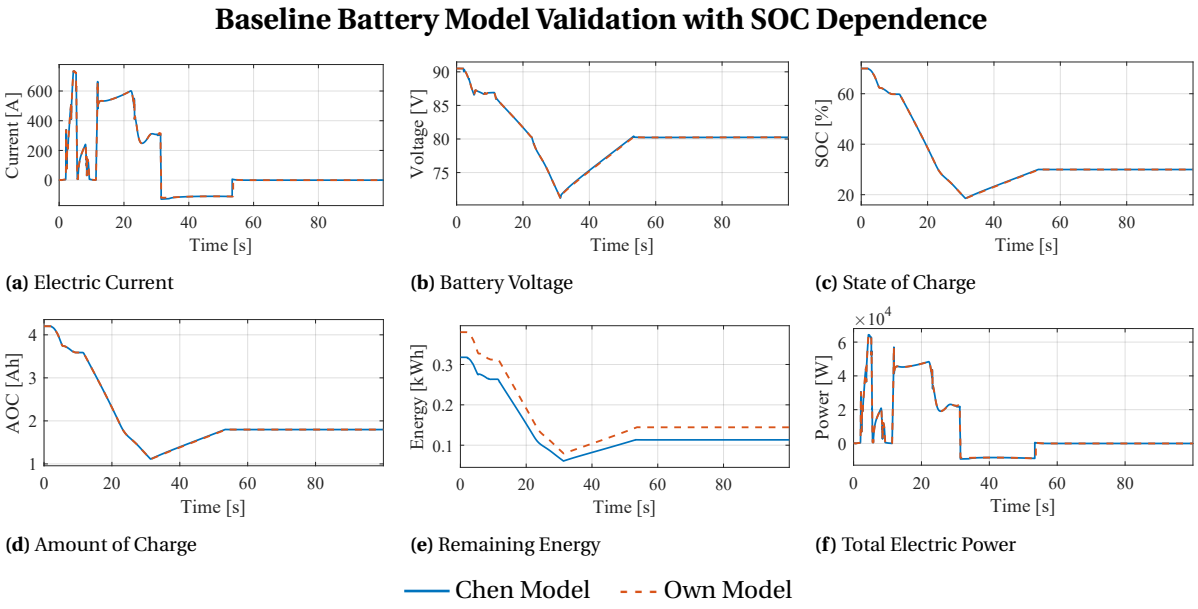
Figure 5.3: Powertrain modes and energy source contributions for Chen battery model without SOC dependence

The battery dynamic response in Figure 5.2 illustrates the instantaneous electric current drawn from the battery in response to the vehicle's electrical power demand, alongside its propagation on the overall state of the battery system. During the initial high-acceleration phases, the powertrain demands high power from its power supply and is seen where the discharge current peaks above 600A, causing a rapid depletion of the battery SOC from 70% to just below the critical 20% lower threshold. Once the battery reaches its limit, ICE becomes the primary powertrain energy source and provides excess mechanical power specifically to drive the EM as a generator, indicated by the charging (negative) battery current. It can be seen that during the recharging phase, the instantaneous terminal voltage exceeds the idle voltage of 100 V which is physically unrealistic and further motivates the implementation of state-dependent parameters to accurately capture true electrochemical behaviour and improve the fidelity of the battery dynamics within the co-simulation.

The powertrain control strategy in Figure 5.3 indicates the respective operating modes engaged over the duration of the drive cycle, transitioning through StartStop, ElecDrive, Boost and EngineDrive states before settling into sustained engine-driven operation. It is clear that the ICE contributes to 57% of the total powertrain which is more than half of the total powertrain propulsion power.

5.1.2. Battery Model Baseline Response with SOC Dependence

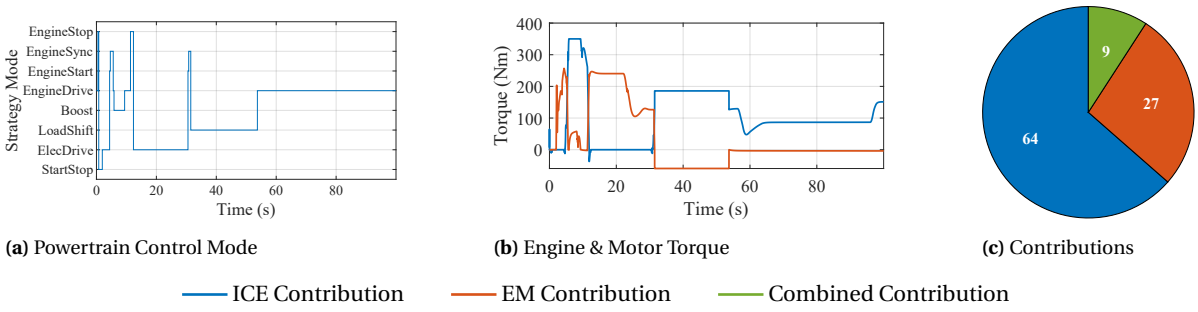
The dynamic response of the static baseline model is validated such that battery model evaluation shifts to consider the impact of incorporating SOC dependence. The dynamic response of the model is presented in Figure 5.4 and the powertrain power supply contributions are illustrated in Figure 5.5.



(a) Electric Current **(b)** Battery Voltage **(c)** State of Charge

(d) Amount of Charge **(e)** Remaining Energy **(f)** Total Electric Power

Figure 5.4: Chen battery dynamic response of developed 2nd Order ECM with SOC dependence



(a) Powertrain Control Mode **(b)** Engine & Motor Torque **(c)** Contributions

Figure 5.5: Powertrain modes and energy source contributions for Chen battery model with SOC dependence

The electric current profile in Figure 5.4 is almost unchanged from the baseline case without SOC dependence, since the vehicle power demand and drive cycle are identical. However, there is a notable difference in instantaneous terminal battery voltage as it starts at a lower idle OCV and falls from approximately 90V to approximately 70V as the SOC depletes from 70 % to 20 %. The voltage additionally recovers smoothly to a lower terminal voltage during the recharging phase, without the abrupt step-change observed previously. The idle OCV produces a more physically realistic dynamic response by incorporating a SOC correction factor. The SOC, AOC and total electric power dynamic responses follow an identical profile to the Chen Battery Model. There is, however, a noticeable deviation in the instantaneous energy response, where the starting energy differs but follows a similar profile thereafter. This arises because the Chen Battery Model does not account for SOC dependence in the idle OCV, whereas this is incorporated in the developed 2nd Order ECM.

The drive cycle is identical for both baseline cases, considering the SOC independency or dependency, where the vehicle travels over 2 km within the 100s Test Run. The superordinate powertrain control strategy follows an almost identical profile to the case without SOC dependence, however the EngineDrive mode is initiated earlier, at approximately 50s instead of 60s. This effects the energy source contribution, where the ICE contributes more than in the case without SOC-dependent idle OCV, increasing from 57 % to 64 %.

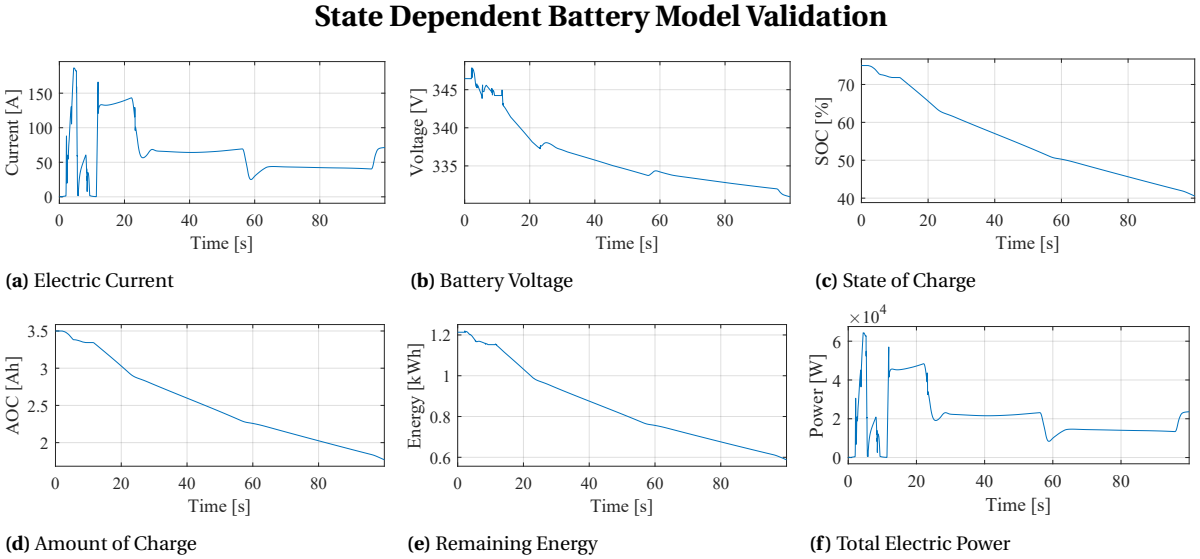
5.1.3. Battery Model Baseline Response Discussion

The baseline HV battery model successfully replicates the Chen response. However, several limitations that motivate extending the complexity of the HV battery model are discussed below:

- **Static Circuit Parameters:** Neglecting circuit parameter state-dependency misrepresents energy management behaviour, as incorporating an SOC-dependent OCV shifts the powertrain distribution and increases the ICE drive contribution from 57 % to 64 %.
- **Open-Loop SOC Estimation:** Open-loop CC lacks feedback error correction, accumulating integration drift over extended race durations that compromises the reliability of SOC-dependent energy management strategies.
- **Absence of Thermal Dynamics:** The absence of a thermal sub-model prevents capturing the effects of battery cell heating on internal resistance and polarisation dynamics, which critically influence overall system performance.

5.2. Extended State-Dependent High-Voltage Battery Model

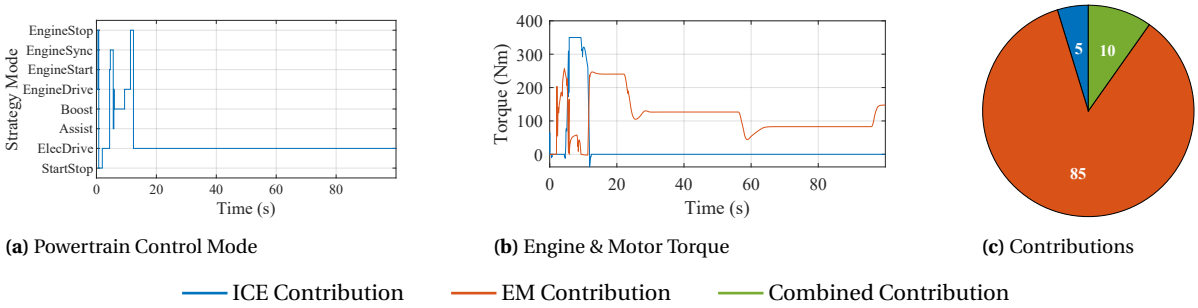
The extended HV battery model is formulated as a state-dependent 2nd Order ECM to accurately represent the nonlinear electrochemical and thermal dynamics inherent to HV battery systems under sustained high charge-discharge cycles typical of endurance racing conditions. The following section evaluates the simulation results of this extended model, demonstrating its dynamic response and its improved fidelity in predicting coupled electro-thermal behaviour. The vehicle states over the corresponding test run are illustrated in Figure 5.1, where it is clear that these states remain identical to those of the Chen battery model baseline, ensuring that the extended model is evaluated under the exact same operating conditions. The extended HV battery model and its represented dynamics are evaluated in Figure 5.6 below.



(a) Electric Current **(b)** Battery Voltage **(c)** State of Charge

(d) Amount of Charge **(e)** Remaining Energy **(f)** Total Electric Power

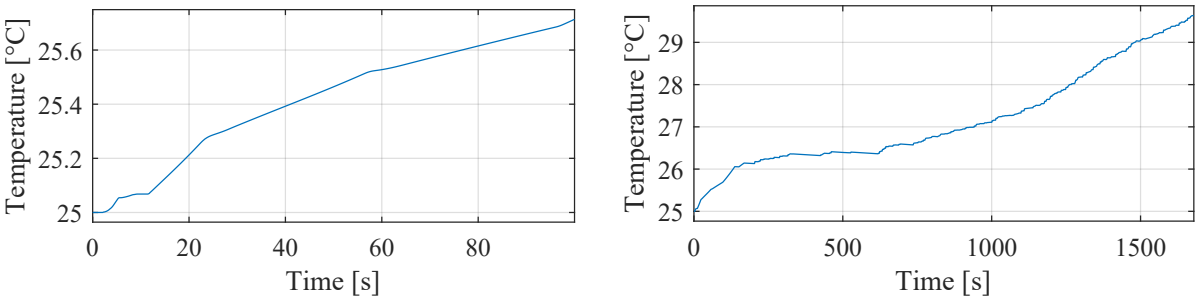
Figure 5.6: Extended 2nd Order ECM dynamic response with state dependence



(a) Powertrain Control Mode **(b)** Engine & Motor Torque **(c)** Contributions

Figure 5.7: Powertrain modes and energy source contributions for extended 2nd Order ECM with state dependence

The representative electrochemical behaviour differs from the simplified baseline battery model which is due to two main reasons: 1. the initial conditions have changed, and 2. the ECM parameters are now state-dependent, where OCV = $f(I, \text{SOC})$, $R_{0,1,2} = f(I, \text{SOC}, T)$, and $C_{1,2} = f(I, \text{SOC}, T)$. The initial OCV is set to 400 V and the capacity, Q_c, is set to 10 Ah. The EM is able to provide more electric propulsion power over the 100 s drive cycle because of the higher operating voltage. The powertrain control strategy, in Figure 5.7, operates almost entirely in ElecDrive mode with its total energy contribution increasing to 85 %. To meet this high electric power demand, which peaks near 60 kW, the SOC drops rapidly from approximately 75 % to 40 % over the duration of the cycle.



(a) Battery Temperature over 100s **(b)** Battery Temperature over Entire Drive Cycle

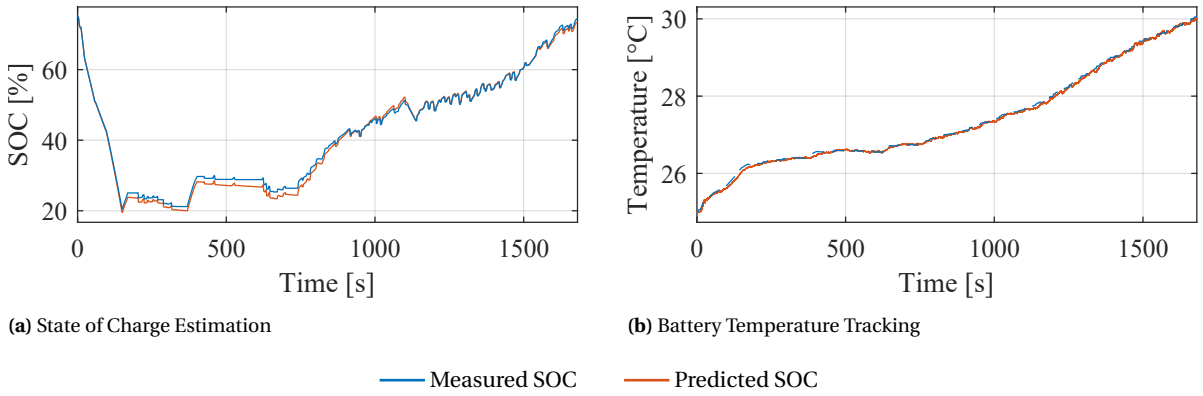
Figure 5.8: Electro-thermal response of extended 2nd Order ECM

The electro-thermal behaviour is represented in Figure 5.8. The extended HV battery model accounts for temperature. It is clear that when the vehicle operates in electric drive mode, the EM draws a high current from the battery. As shown in Figure 5.6, this results in a temperature increase of approximately 0.7 °C over the first 100 s. This temperature rise is physically realistic by the energy used, where for a 95% efficiency, the battery loses approximately 0.03kWh to heat. Mountain driving is more aggressive than sustained highway cruising or normal city driving, demanding continuous high power. These sustained high discharge currents cause a rapid increase in irreversible Joule heating within the cells. This internal heat generation explains the steady temperature rise observed across the entire 1600 s drive cycle, where the battery ultimately reaches nearly 30 °C after more than 25 minutes of operation.

The extended HV battery model serves as an accurate representation of the underlying electrochemical dynamics. This is further verified by comparing the dynamic response shown in Section 3.3 with the Chen battery model response detailed in Appendix A.3, Figure 4. While inherent differences in the parameter dependencies mean the exact values are quantitatively different, the overall profiles are qualitatively close, demonstrating that the essential dynamics are correctly represented. This extended model provides a solid foundation to validate the BCU and EMSs under representative endurance racing conditions.

5.3. Battery Management Strategy for Battery State Tracking

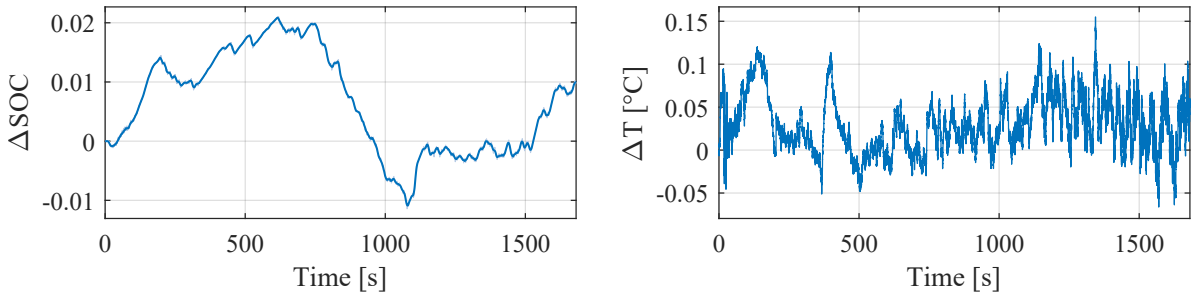
This section evaluates the four-state EKF's ability to track the HV battery's SOC and temperature, using noisy current, voltage, and temperature measurements to compute the innovation residual and predict the state trajectories. As shown in Figure 5.9, the predicted SOC and temperature closely follow the measured reference, capturing both rapid electrical transients and gradual thermal accumulation which is further supported by the SOC and temperature differences in Figure 5.10, which confirms the estimator's advantage over single-sensor measurement or CC and lumped thermal modelling alone.



(a) State of Charge Estimation

(b) Battery Temperature Tracking

Figure 5.9: Extended 2nd Order ECM internal state tracking using EKF



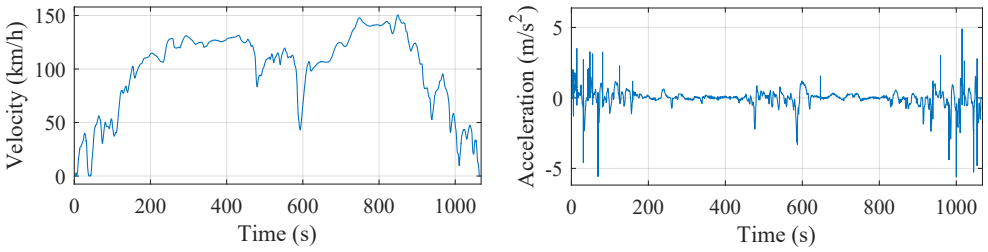
(a) State of Charge Difference

(b) Battery Temperature Difference

Figure 5.10: Extended 2nd Order ECM internal state difference evaluation

5.4. Preliminary Validation in ARTEMIS Driving Cycle

The ARTEMIS driving cycle, illustrated in Figure 5.11, provides a standard reference speed profile that the full-vehicle system tracks within IPG CarMaker. The driving cycle covers a total distance of 29.545 km over a duration of 1068 s, resulting in an average speed of 99.59 km/h, with a maximum speed of 150.40 km/h and a peak acceleration of 1.917 m/s^2.



(a) Vehicle Velocity

(b) Vehicle Acceleration

Figure 5.11: CarMaker vehicle driving profile for ARTEMIS driving cycle

The ARTEMIS driving cycle is a relevant European standard for measuring vehicle pollutant emissions, to evaluate electric-assisted acceleration reduced emissions, which aligns with motorsport's growing focus on sustainability. This section evaluates the powertrain EMS detailed in Section 4.4, a coordinated strategy developed to maintain hybrid powertrain performance while optimising torque distribution to outperform traditional ICE vehicles. In this preliminary scenario, battery dynamics are assessed under two EMS configurations:

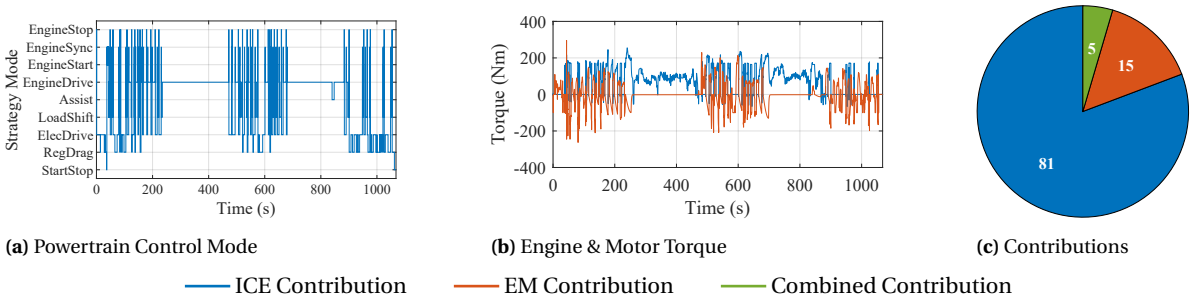
- **Conventional EMS:** The vehicle operates exclusively in Engine Drive mode, relying solely on the ICE.
- **Active Racing EMS:** An endurance-focused, charge-sustaining strategy that actively utilises the EM for torque boosting.

5.4.1. Conventional Energy Management Strategy Performance

The baseline EMS, in which the vehicle operates strictly in EngineDrive mode, is presented to establish a comparative reference for the hybrid powertrain. The control strategy maintains a pure EngineDrive state, resulting in a 100% energy contribution from the ICE, with the EM torque remaining at zero throughout the test duration. The resulting fuel consumption of the conventional powertrain is 9.02 l/100 km, which serves as the baseline performance metric against which the developed charge-sustaining EMS is evaluated.

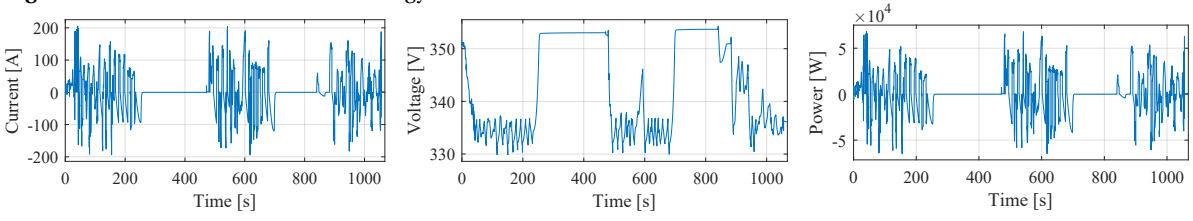
5.4.2. Proposed Hybrid Control Strategy Performance

The performance of the active hybrid EMS adopted in this study is evaluated under the ARTEMIS driving cycle and is illustrated in Figure 5.12. The powertrain control strategy dynamically transitions between EngineDrive, regenerative braking, and electric assist modes during transient acceleration periods, while settling into pure EngineDrive during near-zero acceleration periods. This behaviour confirms that the hybrid powertrain relies primarily on the ICE for baseline propulsion, deploying the EM to provide torque assist and energy recovery during high-demand acceleration periods. The hybrid configuration achieves a fuel consumption of 8.49 l/100 km which is 0.53 l/100 km lower compared to the conventional powertrain baseline, therefore verifying the effectiveness of the proposed control strategy.



(a) Powertrain Control Mode **(b)** Engine & Motor Torque **(c)** Contributions

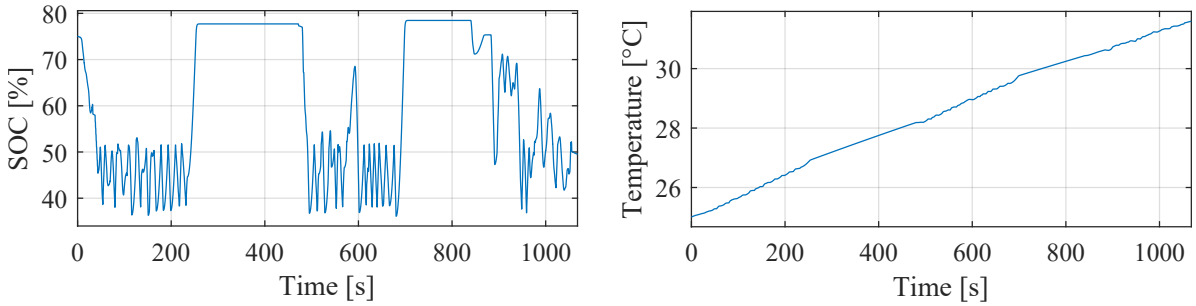
Figure 5.12: Powertrain modes and energy source contributions for extended 2nd Order ECM for ARTEMIS



(a) Electric Current **(b)** Terminal Voltage **(c)** Total Electric Power

Figure 5.13: Extended 2nd Order ECM dynamic response with state dependence for ARTEMIS

The HV battery dynamic response is presented in Figure 5.13, where the response clearly illustrates a charge-sustaining behaviour across the transient load profile. It can be seen that the electric current and total power profiles alternate symmetrically between positive (discharging during acceleration and EM assistance) and negative values (regenerative braking and energy recovery), peaking at approximately ±200 A and ±60 kW, respectively. The terminal voltage fluctuates dynamically in response to these transient load variations and can be seen dropping during high-power discharge and recovering during regeneration. This balanced charge-sustaining behaviour is further validated in Figure 5.14.



(a) State of Charge Estimation

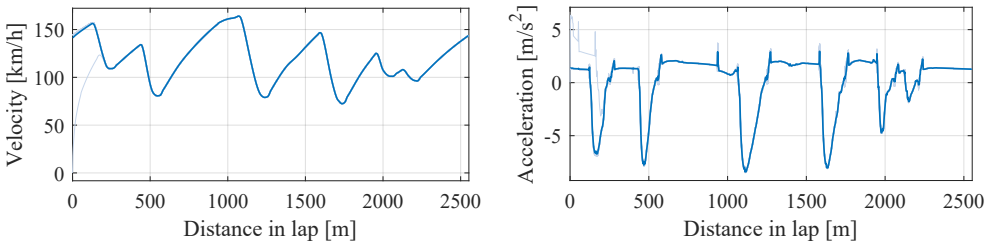
(b) Battery Temperature Tracking

Figure 5.14: Evaluation of battery internal states for ARTEMIS

The ARTEMIS cycle evaluation confirms that the supervisory energy management strategy successfully achieves charge-sustaining operation. During aggressive acceleration and high-demand phases, the battery discharges and oscillates within lower operational bounds for ElecDrive to maximize electric propulsion. Regenerative braking and load-shifting modes actively recover energy up to 78% to restore the SOC toward its nominal 75% target, ensuring long-term energy sustainability and system robustness. The observed dynamic SOC swing between 38% and 78% demonstrates that the controller fully utilises the available operational window to balance high-power electric assistance and continuous energy recovery.

5.5. Endurance Racing Driving Scenario Evaluation

The performance of the integrated power supply model with state estimation, thermal management, and energy management for the hybrid endurance powertrain is evaluated under a representative endurance racing driving scenario. This extended evaluation assesses the system's long-term energy management, thermal accumulation, and state-tracking robustness under continuous, highly dynamic racing loads. The driving scenario is modelled on the Hockenheimring racing circuit, which is approximately 2600m long. During the simulation, the vehicle achieves an average speed of approximately 117km/h and a maximum speed of 162km/h. The power supply framework and controller schemes are evaluated over a 1 hour test duration, as illustrated in Figure 5.15, where the vehicle travels approximately 120km while demonstrating the identical velocity and acceleration profiles per lap.



(a) Vehicle Velocity

(b) Vehicle Acceleration

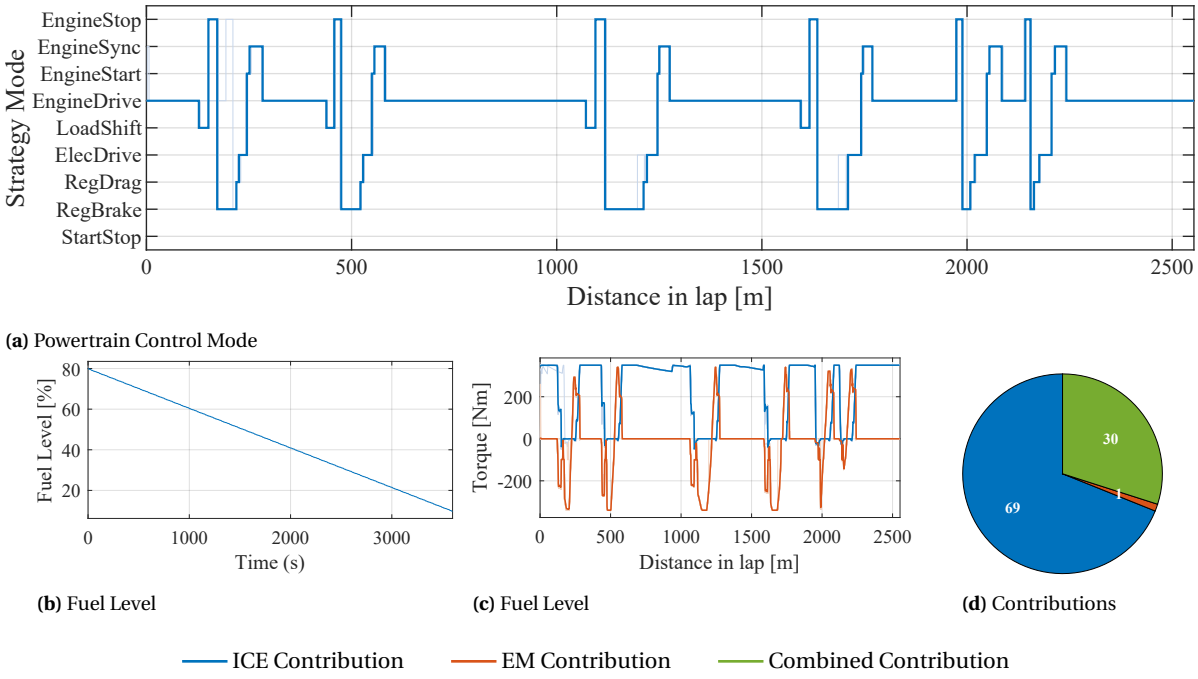
Figure 5.15: CarMaker vehicle driving profile for Hockenheim racing driving cycle

5.5.1. Conventional Control Long-Term Performance Assessment

To establish a performance baseline for the hybrid endurance powertrain architecture, the vehicle's long-term performance is assessed using a purely conventional control strategy where vehicle propulsion relies exclusively on the ICE. It is determined from real-time simulation that operating without hybrid assistance leads to severe fuel depletion under continuous racing loads, where the vehicle's fuel level reaches empty at 3455s and terminates the simulation. This premature fuel starvation highlights the critical role of hybrid systems in endurance applications, where electric assistance and regenerative energy capture optimise fuel efficiency and ensure the vehicle can complete the full race distance without hindering overall vehicle performance.

5.5.2. Hybrid Racing Control Long-Term Performance Assessment

The long-term behaviour of the full hybrid endurance powertrain is evaluated under the same one-hour Hockenheimring racing scenario, as presented in Figure 5.16. As shown in the powertrain control mode profile over a representative single-lap cycle, the active hybrid strategy continuously coordinates multiple operating states, which include boost, load-shifting, and regenerative braking to dynamically manage and coordinate power delivery. This active distribution is reflected in the torque and energy contributions where the ICE accounts for 69 % of the total energy supply, while combined hybrid and electric contributions account for 30 %. A crucial factor to note is that the vehicle completes the entire driving simulation stint with roughly 10 % fuel remaining, which demonstrates that the integration of electric assistance and regenerative energy further reduces fuel consumption without compromising the overall driving performance.



(a) Powertrain Control Mode

(b) Fuel Level

(c) Fuel Level

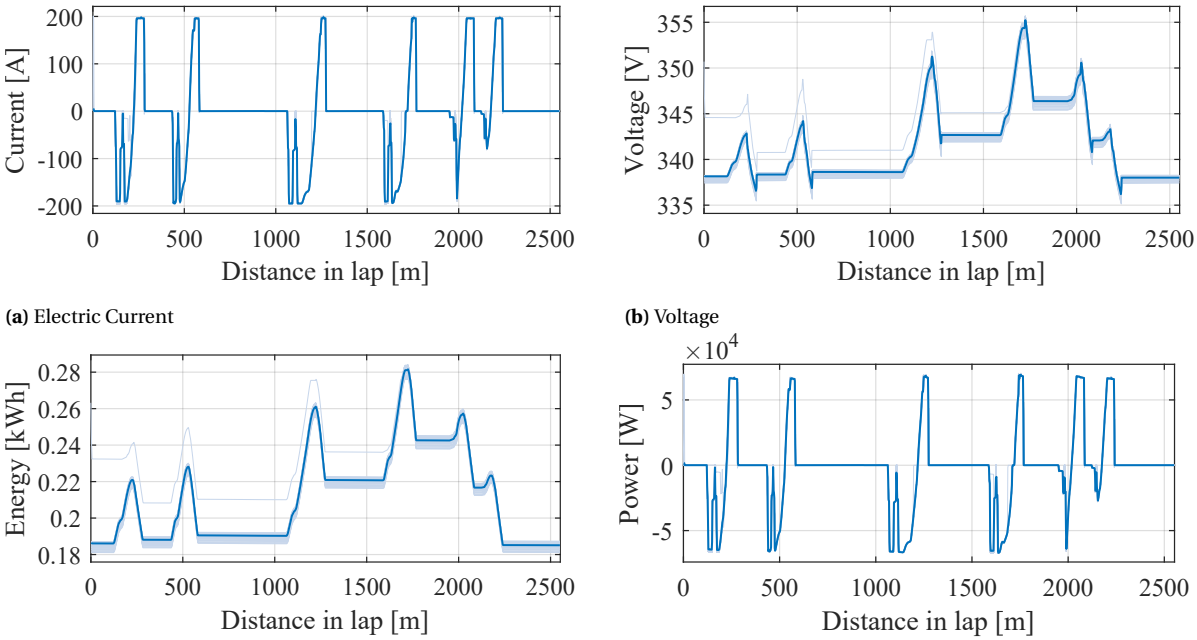
(d) Contributions

Figure 5.16: Powertrain modes and energy source contributions for active racing EMS

Accurate tracking of internal battery states is critical for coordinating powertrain control strategies as well as managing long-term torque distribution. The internal states, within the power supply architecture, are monitored by the BCU using estimates derived from the HV battery power supply model. The following sections evaluate the optimal operating temperature required to minimize battery degradation, the state-estimation performance focusing on SOC tracking across its dynamic charge-sustaining and charge-depleting profiles, and finally the temperature tracking performance necessary for effective thermal management throughout the full one-hour racing stint.

5.5.3. HV Battery Dynamics

The battery dynamic response over a representative single-lap cycle, with lap distance of 2548 m, is illustrated in Figure 5.17. The average individual-lap profile, in blue, is overlaid on the recursive lap simulations over the 1-hour stint, in grey, which captures both transient variation and the average performance trend. The recursive lap simulations reflect high lap-time repeatability with minimal lap-to-lap variance. This driving behaviour is generated by IPG CarMaker's advanced driver model, configured with an aggressive style that forces high-performance cornering, hard acceleration, and intense braking, consistent with the representative race stint in Figure 5.15. A notable feature of the multi-lap cycle is the alternating pattern of discharge-heavy and charge-heavy phases, reflecting how the driver model handles consecutive laps.



(a) Electric Current

(b) Voltage

(c) Remaining Energy

(d) Total Electric Power

Figure 5.17: Lap-profile showing charge-sustaining behaviour for 2nd Order ECM dynamic response with state dependence

It is clear that the resulting electric current and total electric power profiles exhibit severe transient spikes, reaching upper and lower limits of ±200 A and ±60 kW, respectively. These sharp peaks correspond directly to heavy power demands during acceleration boost phases and high energy recovery during regenerative braking. Despite these high-stress dynamic loads, both the terminal voltage and the remaining energy capacity strictly follow a stable charge-sustaining profile. The remaining energy oscillates within a controlled band between 0.18 kWh and 0.28 kWh, confirming that the energy management strategy successfully balances power delivery and recovery without causing net pack depletion. The presented lap-time simulation for HV battery dynamics highlights the exceptional repeatability and robustness of the integrated powertrain and control framework under continuous endurance conditions.

State of Health Evaluation for Thermal Operating Conditions

An initial SOH evaluation is conducted to determine the optimal operating temperature that the battery can sustain without causing performance degradation, system disruptions, or premature failure. This evaluation is performed across six discrete operating temperatures [25°C, 30°C, 35°C, 40°C, 45°C, and 50°C]. The state-dependent parameters for the 2nd order ECM are derived from technical lookup tables bounded at 45°C. Because of this upper limit, simulations at 50°C rely on data from the maximum table boundary, resulting in the overlapping trajectories observed in Figure 5.18.

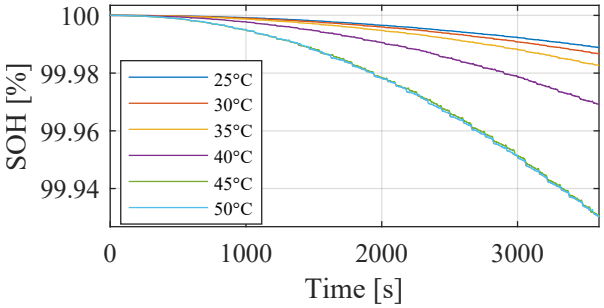
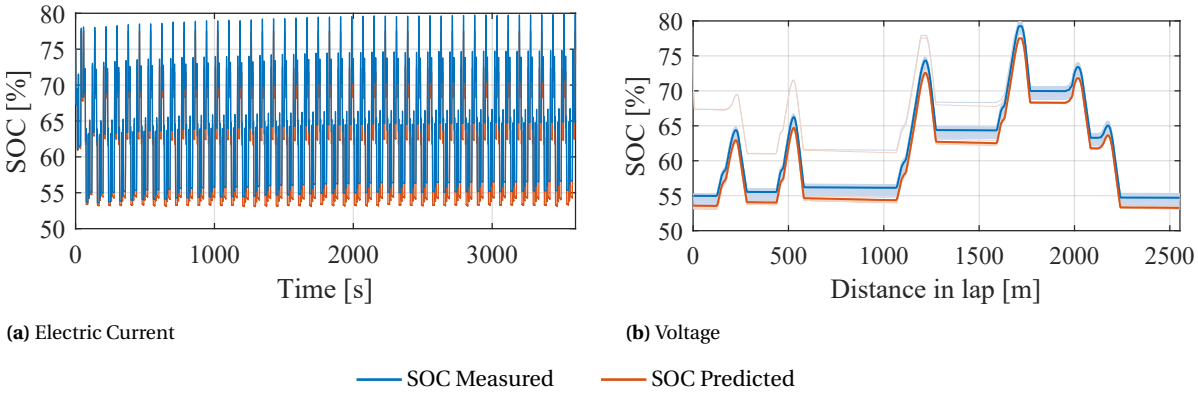


Figure 5.18: Evaluation of SOH Degradation for 2nd Order ECM dynamic response with state dependence

As shown in the evaluation results, battery degradation accelerates non-linearly with rising temperatures due to increased thermal losses. The optimal operating temperature is selected as 35°C, as it maintains a minimal degradation rate of < 0.02 % per hour, whereas temperatures exceeding this threshold experience sharply accelerated power fade. A conservative operating point is selected to guarantee that the battery remains robust against performance drops, power losses, or system failures during aggressive racing manoeuvres, and it also accounts for speed and acceleration limitations in the driver simulation.

State of Charge Estimation Evaluation

The SOC estimation performance during the one-hour endurance racing scenario is evaluated in Figures 5.19 and 5.20. As illustrated by the time-based and lap-distance profiles in Figure 5.19, the battery SOC exhibits a highly repetitive profile characterised by charge-sustaining behaviour, confirming the energy-neutral operation of the hybrid powertrain. Throughout the entire race stint, the SOC swings dynamically between 54 % and 80 %, remaining strictly within the specified usable operational window. This demonstrates that the active racing EMS fully exploits the usable SOC window of the HV battery to balance high electric power delivery with continuous energy recovery to maximise the performance and efficiency of the hybrid powertrain while maintaining the battery longevity.

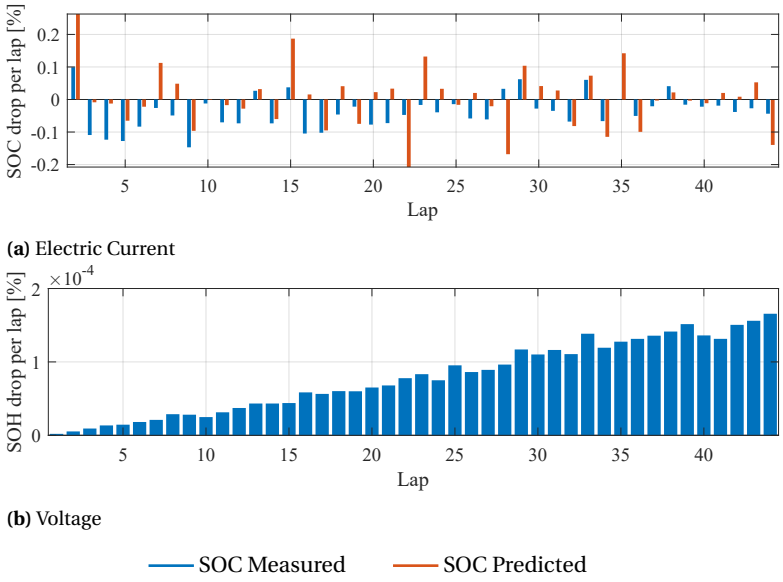


(a) Electric Current

(b) Voltage

Figure 5.19: SOC Dynamic Swing over racing profile stint

A comparison between the measured SOC (derived from open-loop CC) and the predicted SOC (estimated via the EKF) reveals distinct trajectory behaviours. The measured SOC exhibits a progressive upward drift over time due to uncorrected cumulative drift and integration errors, whereas the EKF-predicted estimate successfully compensates for sensor noise and system uncertainties. As a result of this, the deviation between the open-loop and filtered trajectories gradually increases as the simulation progresses, emphasising the critical role of the EKF to mitigate accumulated integration errors to ensure reliable long-term state tracking.



(a) Electric Current

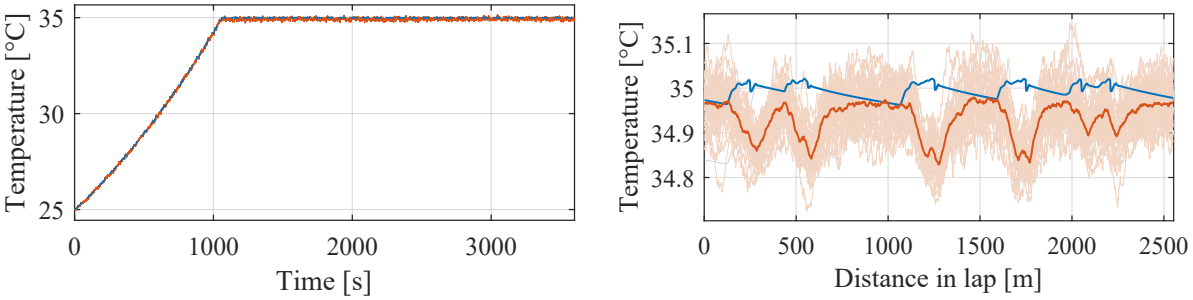
(b) Voltage

Figure 5.20: SOC and SOH drop per lap over the entire 1 hour simulation

Figure 5.20 details the variations across the racing profile stint per lap. The per-lap SOC drop remains tightly bounded within allowable limits (<0.05% per hour), reinforcing the stability of the charge-sustaining strategy. Meanwhile, the SOH drop per lap demonstrates that cumulative battery degradation occurs non-linearly, accelerating as the thermal and electrical stress accumulates over the course of the aggressive racing scenario. The robustness and reliability of the integrated battery state estimation and energy management framework are validated for extended high-stress racing stint profiles.

5.5.4. Thermal Management

The thermal management performance and cooling system response during the one-hour endurance racing scenario are evaluated in Figures 5.21 and 5.22 where the average load profile is plotted on top of the lap-to-lap temperature profiles. The battery temperature increases exponentially during the initial simulation phases until it reaches the targeted optimal operating threshold of 35°C at approximately 1000 s. At this point, the thermal operating condition is reached, and the LPV MPC strategy anticipates thermal loads and actively corrects them by engaging actuators to circulate coolant through the battery pack at specified mass flow rates, successfully managing the pack temperature within safe operating bounds.

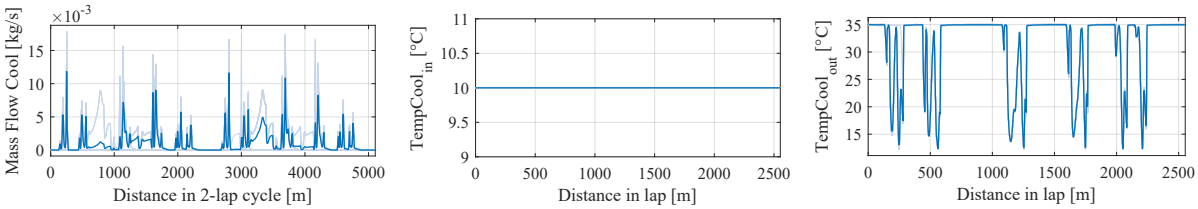


(a) Battery Temperature over Time

(b) Battery Temperature per Lap

Figure 5.21: Battery temperature tracking over the racing profile stint

The cooling system tracks the lap-sector heat cycles and maintains the core battery temperature near 35°C. However, the single-move horizon ($m = 1$) induces an aggressive control action, causing the outlet coolant temperature to fluctuate sharply between 15°C and 35°C. This behaviour highlights a clear area for control smoothing to minimise thermal fatigue on the cooling circuit components.



(a) Mass Flow Rate **(b)** Inlet Coolant Temperature **(c)** Outlet Coolant Temperature

Figure 5.22: Cooling circuit actuator response over the racing profile stint

5.6. Discussion of Results

5.6.1. Evaluation

The model-based design of a HV battery management system is effectively integrated and validated in the IPG CarMaker vehicle simulation environment. The battery management system framework integrates three main subsystems, namely the power supply model, battery control unit and powertrain control. The 2^{nd} Order ECM is fully coupled with a four-state EKF for real-time state tracking of SOC, SOH and temperature, paired with a LPV MPC strategy for active thermal management alongside powertrain energy management strategies which collectively ensure accurate representation of battery dynamics, state estimation and charge-sustaining behaviour for lap-time simulations.

Controller strategies are evaluated, namely the effectiveness of state tracking and thermal control. The four-state EKF effectively mitigates open-loop CC drift and maintains an accurate representation of the battery state, which is essential for managing the energy contribution split of 69% from the ICE and 30% from combined ICE-EM operation. Accurate state tracking prevents premature battery depletion, which under a conventional, ICE-only strategy would eliminate the regenerative drag recovered through RegDrag, imposing higher loads on the brake discs and increasing the risk of system failure. The thermal management system regulates the core battery temperature around the optimal 35°C threshold throughout the simulation. Lap-simulation results demonstrate the value of the hybrid electric powertrain, and how it exploits the EM to assist the ICE and reduce vehicle pollutant emissions, aligning with the growing focus on sustainability in motorsport. The active hybrid EMS avoids the premature fuel starvation of the conventional powertrain, completing the one-hour simulation with 10% fuel remaining which corresponds to approximately two fewer fuel stops than a conventional powertrain following an identical drive profile.

The overall performance of the coordinated HV battery management system is evaluated against the charge-sustaining battery performance, namely the peak to peak fluctuation, net change and consistency of the battery SOC per lap over a one-hour driving cycle scenario simulation. Lap-to-lap repeatability is verified by evaluating the battery dynamics for recursive lap simulations that indicate minimal lap-to-lap variance in current, voltage, and remaining energy. It is evident that the system maintains a strict charge-sustaining behaviour, achieving energy-neutral operation. The dynamic battery SOC peak-to-peak fluctuation per lap is approximately 26% and the net change per lap is given by $\Delta SOC \approx 0$ with the highest net change being 0.002, and the lap time repeatability is verified by the average SOC per lap overlaying the cumulative SOC profile. The rule-based FSM actively rebalances energy deployment against recovery on every lap, rather than simply avoiding depletion across a single stint, which is the behaviour required for a controller intended to operate over a full endurance race distance. This reflects that, for the given drive cycle, the system exploits the advantages of electric propulsion by executing the ElecDrive, RegBrake, and RegDrag strategy modes effectively. However, the driving cycle does not exhibit high velocity and transient acceleration of typical aggressive racing behaviour to activate the Assist and Boost strategy modes.

5.6.2. Limitations

Despite the robust performance demonstrated by the simulation framework, several limitations must be acknowledged and are described in this section.

Battery Plant Modelling

The battery plant model is entirely model-based, and simplifications and assumptions have therefore been made to represent the system behaviour as accurately as possible without compromising real-time simulation feasibility. The state-dependent parameter lookup tables for the 2^{nd} Order ECM are experimentally bounded at 45°C, which limits the model's accuracy when predicting electrochemical degradation and internal resistance behaviour under severe thermal runaway or high-temperature racing conditions. The thermal model further adopts a lumped formulation rather than distributed nodal modelling, neglecting cell-to-cell variations and localised thermal gradients within the battery pack, in order to preserve computational efficiency for real-time co-simulation. Physical experimental data from a real endurance test bench or vehicle prototype is not available to validate the battery, powertrain, state, and thermal responses. The baseline Chen battery model, IPG CarMaker's built-in reference model, is therefore used as the foundation against which this study's model is validated.

State Estimation and Control Algorithm

Limitations also exist within the estimation and advanced control algorithm architectures. The four-state EKF is validated using synthetic zero-mean Gaussian white noise injected onto ideal current, voltage, and temperature signals, rather than noise characteristics derived from physical sensor data sheets or measured hardware, whereas real sensor noise may exhibit bias, non-Gaussian behaviour, or correlated drift not captured by this assumption which can impact the estimation accuracy in hardware implementations. The thermal management MPC strategy is tuned with a single-move prediction horizon which induces aggressive actuator action and sharp coolant outlet temperature transients that increase thermal fatigue on the cooling circuit components such as pumps and valves.

Simulation Environment and Driving Cycle

The lap simulation behaviour introduces several limitations, since the system is not subjected to fully representative endurance racing conditions. IPG CarMaker's advanced driver model relies on predefined control parameters that cannot fully replicate the limit-handling behaviour, complex tyre slip dynamics, and adaptive lines executed by a professional human endurance racing driver. The simulation framework also assumes uninterrupted track running, neglecting dynamic racing interactions such as overtaking manoeuvres, aerodynamic slipstreaming, and the strategic time losses associated with pit stops. Finally, the simulated Hockenheimring drive cycle does not demand peak acceleration transients high enough to trigger the highest-priority Assist and Boost strategy modes, leaving the framework's behaviour under extreme charge-depleting conditions unvalidated.

6

Conclusion and Recommendations

6.1. Conclusion

The HV battery management system framework is evaluated for its long-term energy management, thermal control, and state-tracking behaviour under the continuous, highly dynamic racing loads of a representative endurance racing lap-time simulation on the Hockenheimring circuit. This study contributes a coordinated battery management system that integrates advanced high-voltage battery modelling, state estimation, and thermal control within a co-simulation environment, building a robust framework to advance public knowledge and optimise performance under the severe electrical and thermal stresses inherent to endurance racing driving profiles, characterised by high-power transients, rapid charge-discharge cycles, and aggressive continuous loads.

Extension of the baseline battery model into a state-dependent 2^{nd} Order ECM accurately captures the non-linear electrochemical dynamics of the HV battery across varying operating conditions, providing an accurate foundation for the state estimation and control algorithms built upon it. The four-state EKF tracks the battery SOC on this foundation and resolves the open-loop CC drift inherent to the baseline model by leveraging real-time voltage and temperature feedback, bounding SOC estimation errors within tight margins of ± 0.02. Thermal state tracking is achieved to a similar standard, with the lumped thermal model keeping core temperature discrepancies under ± 0.15°C while preserving the real-time processing speed required for co-simulation and minimising the computational overhead. The modelling and estimation results are validated across standardised driving cycles, confirming that the framework produces accurate and reliable state tracking under representative operating conditions. Finally, the lap simulation on the Hockenheimring circuit confirms that the supervisory energy management strategy achieves charge-sustaining operation by dynamically exploiting the usable SOC window of 54% to 80%, yielding improved fuel efficiency, stable thermal regulation, and reliable long-term state tracking under the aggressive continuous loads characteristic of endurance racing.

Overall, the synchronised performance of the energy management controller, the BCU, and the state-dependent equivalent circuit model highlights a robust, highly repeatable, and well-coordinated multidisciplinary architecture suitable for endurance racing applications.

6.2. Recommendations for Future Works

The results of this study demonstrate the effectiveness of the integrated HV battery management architecture. The findings are, however, fundamentally derived from model-based co-simulations in CarMaker for Simulink that are subject to specific assumptions and boundary conditions. As previously discussed in Section 5.6, discrepancies between simulation and physical battery operational behaviour primarily originate from lumped model approximations, bounded state-dependent parameter tables, and predefined driver models that do not fully capture the limit-handling behaviour and adaptive racing lines of a professional human endurance racing driver.

This model-based work should be paired with experimental validation, using physical test bench data or telemetry collected from real-world hybrid racing track testing, to confirm that the coupled simulation framework and state estimation algorithms generalise beyond the co-simulation environment. The state-dependent parameter lookup tables underpinning the battery model would also benefit from extended thermal characterisation, expanding testing beyond the current 45°C bound to preserve model fidelity at the higher temperatures aggressive racing operation can reach. Alternative forced convection strategies in the cooling architecture, such as integrating passive aerodynamic airflow through the vehicle body alongside the existing active liquid cooling, could improve thermal efficiency and reduce pump losses. The thermal control algorithm would likewise benefit from multi-move MPC tuning to minimise thermal shock on the closed-loop cooling architecture.

To bridge the gap between simulation and real-world deployment, future work must prioritise comprehensive sensitivity evaluations under variable driver profiles and track dynamics, alongside hardware-in-the-loop testing and full-scale prototype validation to further verify model-based HV battery management system performance under empirical conditions.

Appendix

A.1. Battery Modelling Approach Implementation in MATLAB & Simulink

A.1.1. State-Depended Model-Parameter 3D Lookup Tables

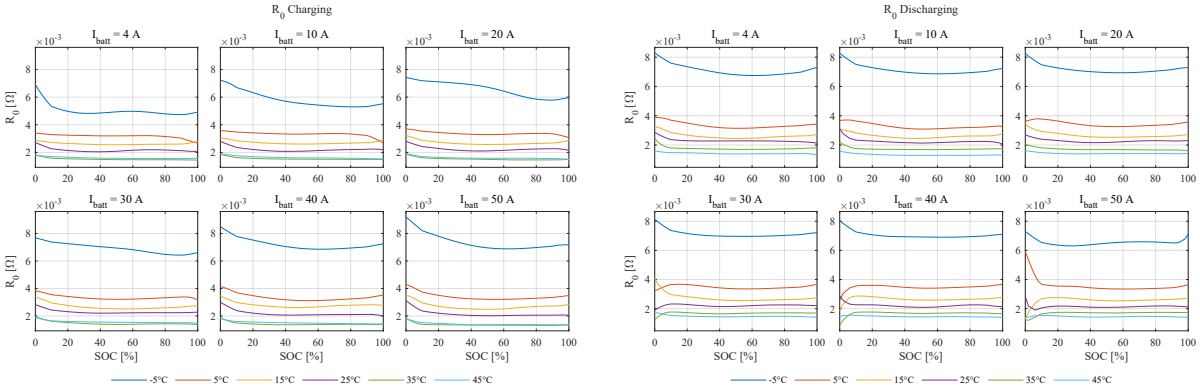


Figure 1: State-dependent R_0 model-parameter 3D lookup table across charging and discharging operating conditions

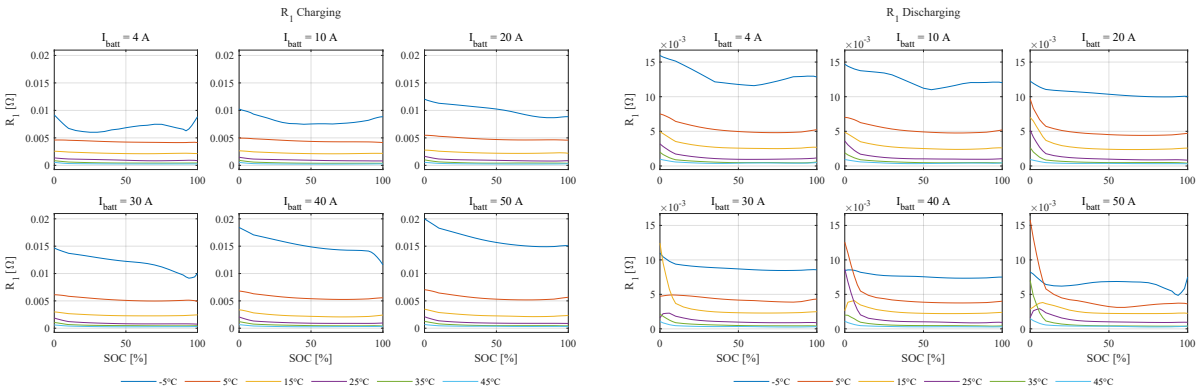


Figure 1: State-dependent R_1 model-parameter 3D lookup table across charging and discharging operating conditions

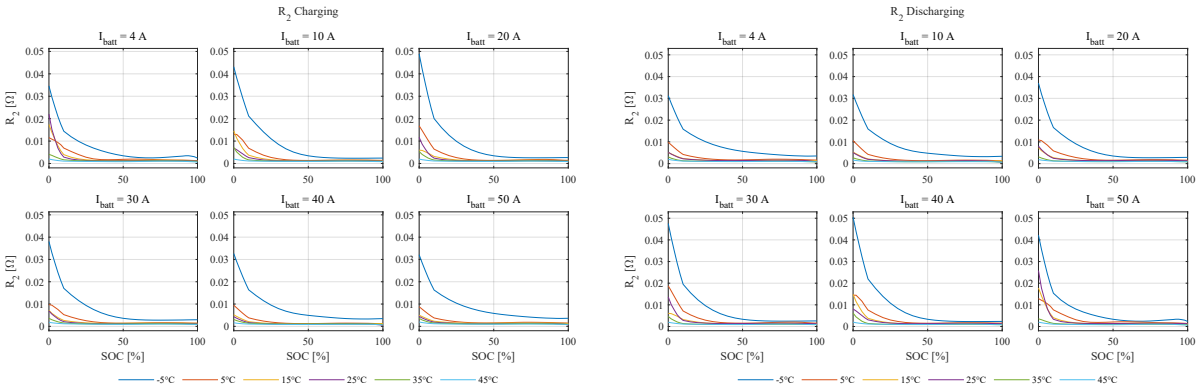


Figure 1: State-dependent R_2 model-parameter 3D lookup table across charging and discharging operating conditions

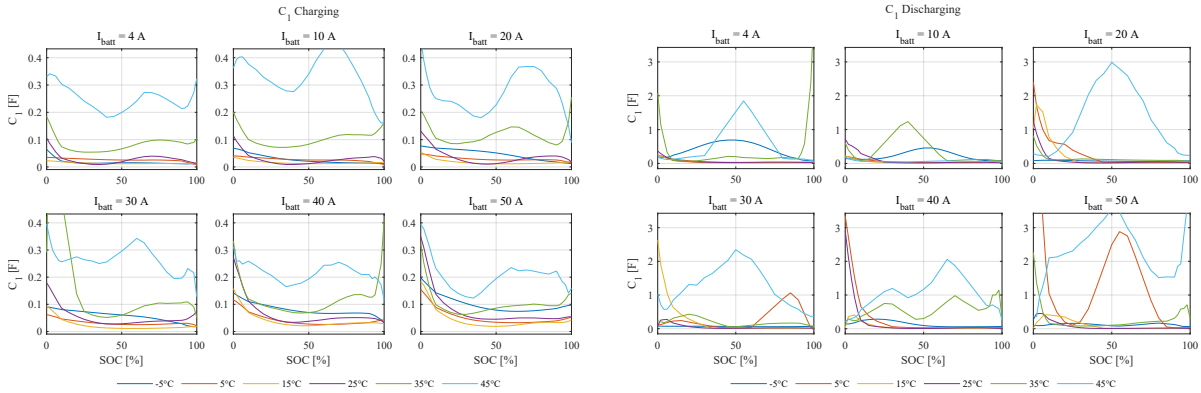


Figure 1: State-dependent C_1 model-parameter 3D lookup table across charging and discharging operating conditions

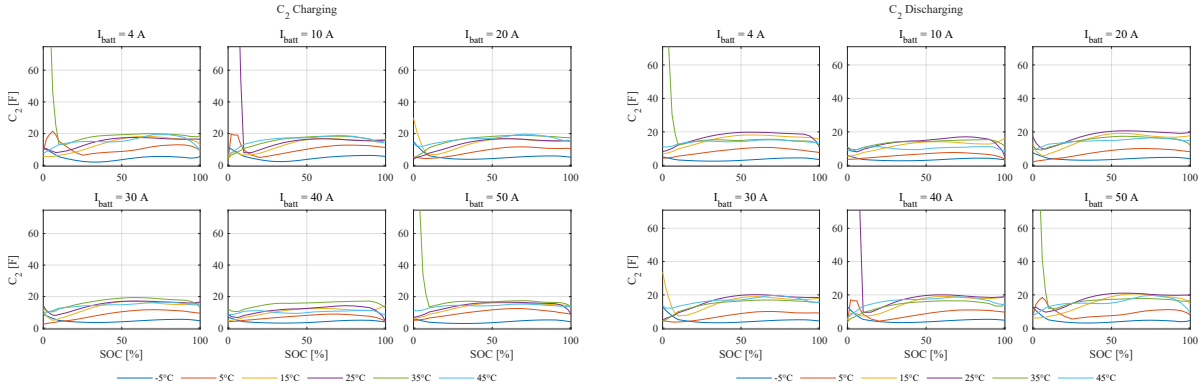


Figure 1: State-dependent C_2 model-parameter 3D lookup table across charging and discharging operating conditions

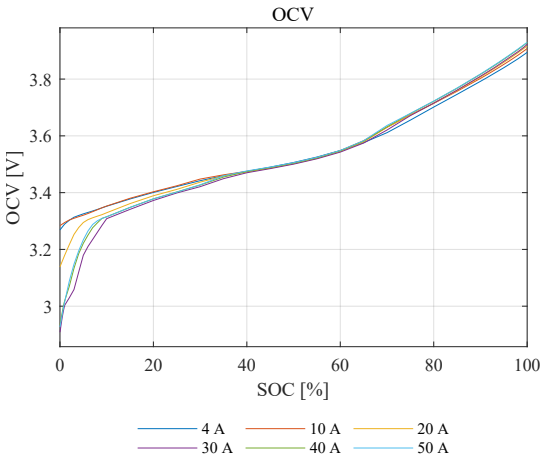
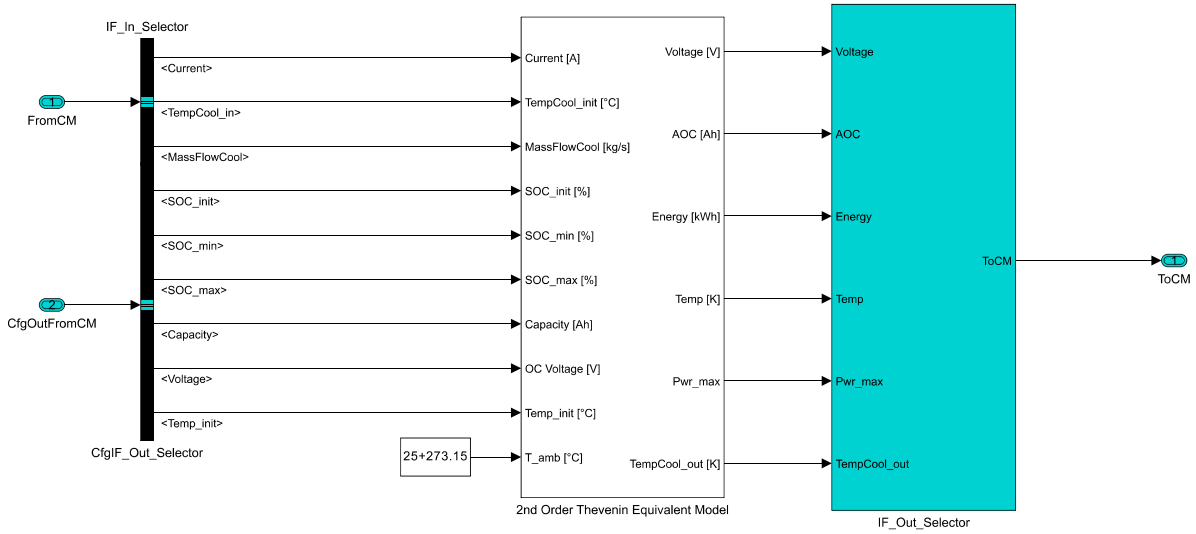
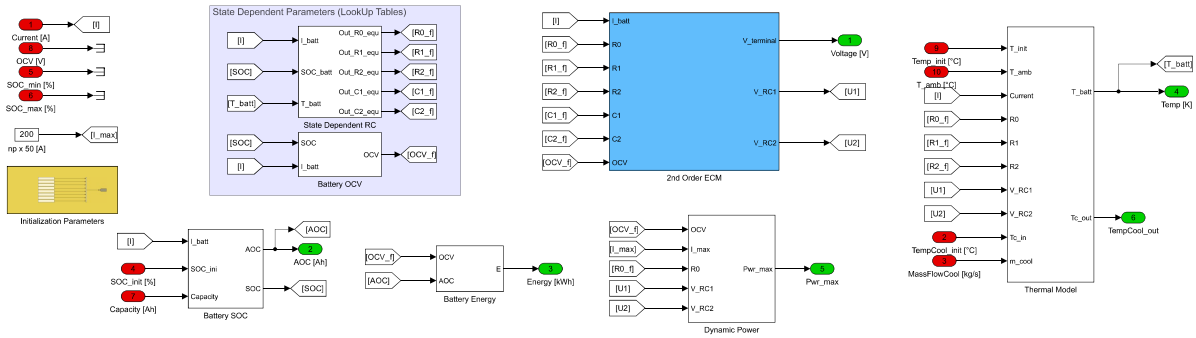


Figure 1: State-dependent OCV model-parameter 3D lookup table across charging and discharging operating conditions

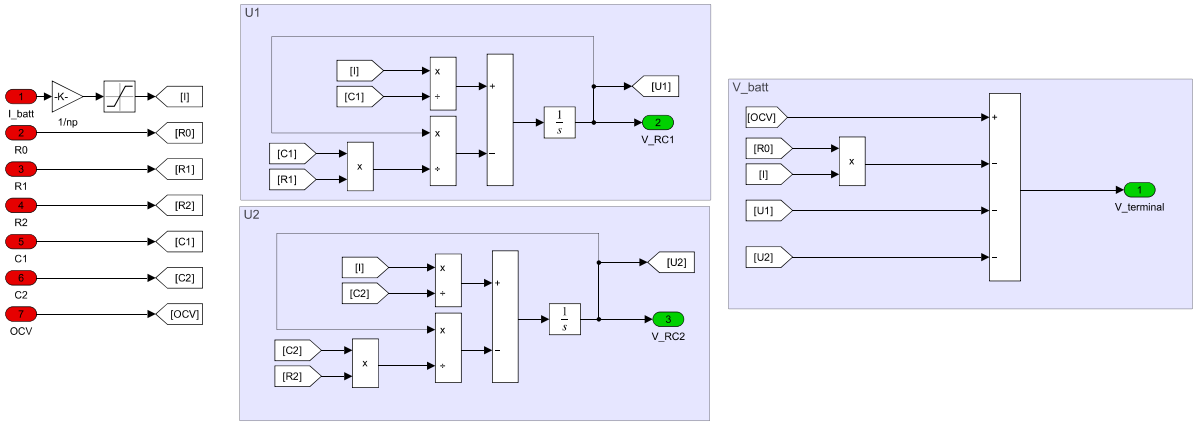
A.1.2. Simulink Coder Plug-In Model for CarMaker Power Supply



(a) Level 1: Top level power supply Simulink coder plug-in model



(b) Level 2: 2^{nd} order ECM subsystem

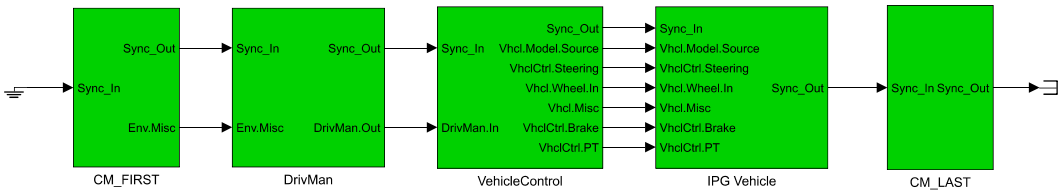


(c) Level 3: Terminal voltage implementation in Simulink

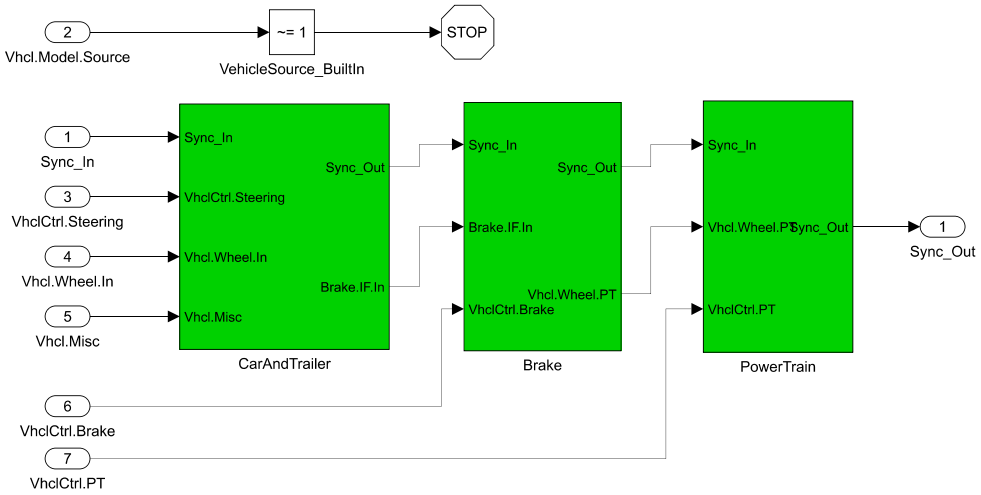
Figure 2: Simulink plug-in model for IPG CarMaker of HV battery power supply system

A.2. Controller Strategy Development in CarMaker for Simulink

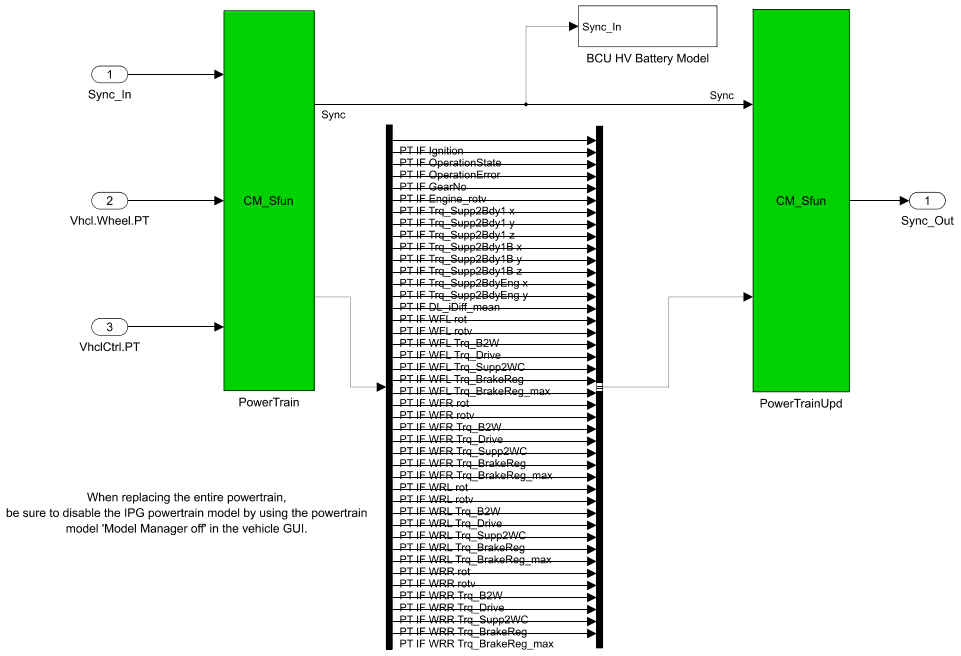
A.2.1. State Estimation implementation in CM4SL



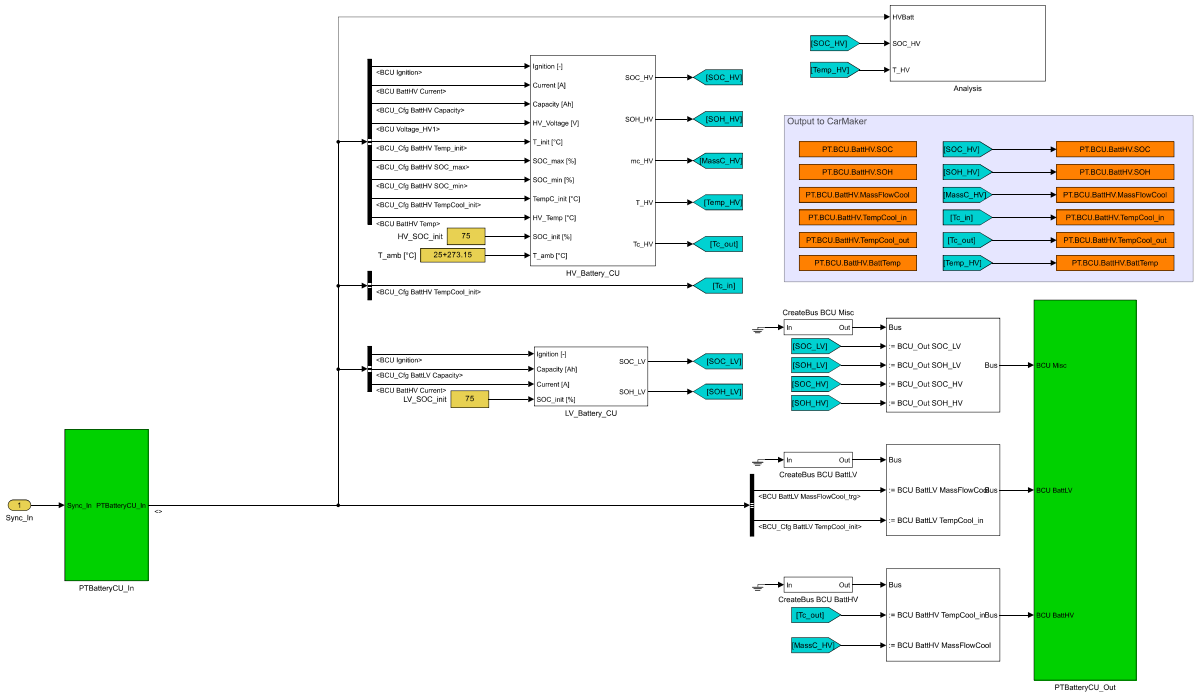
(a) Level 1: Top-level CarMaker execution chain



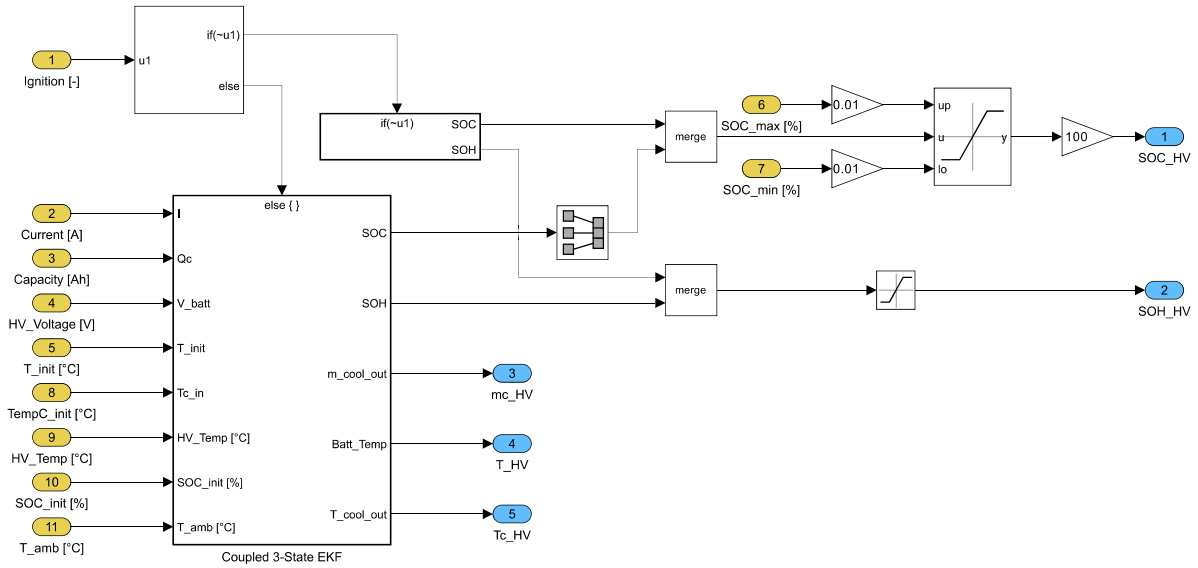
(b) Level 2: Subsystem containment inside `IPG Vehicle`



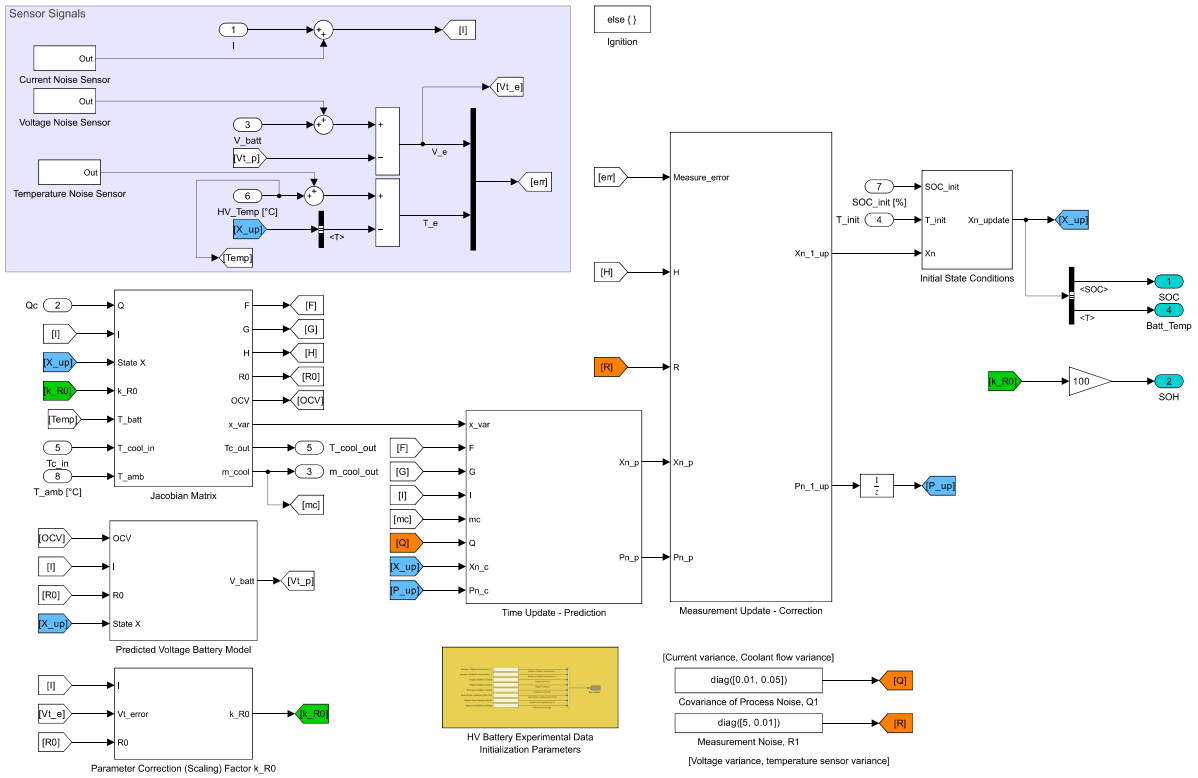
(c) Level 3: BCU subsystem execution routing within `PowerTrain`



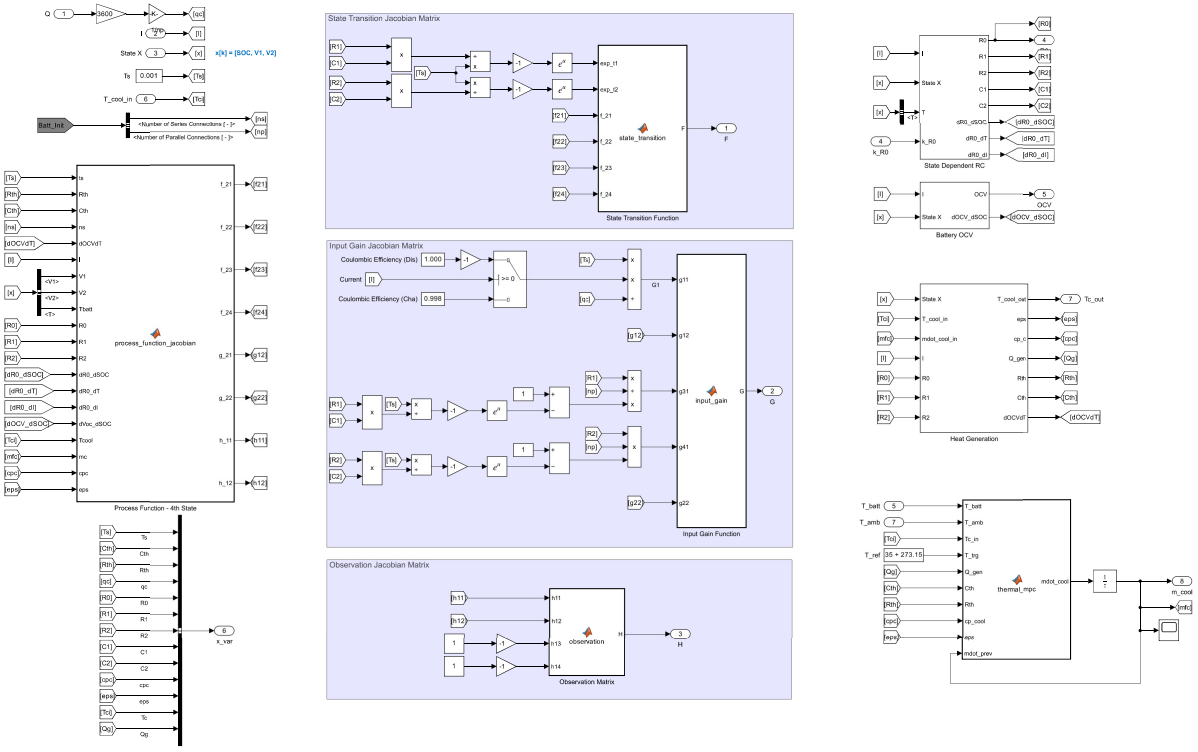
(d) Level 4: Internal signal routing, bus creation, and battery control subsystems



(e) Level 5: Coupled 3-State EKF estimation and state limiting architecture



(f) Level 6: Coupled 4-State EKF estimation and state limiting architecture



(g) Level 7: Jacobian linearisation for the 4-State EKF

Figure 3: CarMaker execution chain and BCU state estimation architecture across the CM4SL model hierarchy

A.2.2. Single-move LPV-MPC for Battery Thermal Management

```
function mdot_cool = thermal_mpc(T_batt, T_amb, Tc_in, T_trg, Q_gen, Cth, Rth, cp_cool, eps, mdot_prev)

    Ts = 1;  p = 100;

    beta      = 50;
    mdot_min  = 0.001;   mdot_max = 1000;   max_step = 0.015;
    ramp_rate = 0.005;

    persistent T_filt
    if isempty(T_filt), T_filt = T_batt; end
    T_filt = 0.9*T_filt + 0.1*T_batt;
    T = T_filt;

    Ax = -(1/Cth) * (1/Rth + mdot_prev*cp_cool*eps);
    Bv =  [1/Cth, (mdot_prev*cp_cool*eps)/Cth, 1/(Cth*Rth)];
    Bu = -(cp_cool*eps/Cth) * (T - Tc_in);

    A_d  = exp(Ax*Ts);
    B_d  = (Bv/Ax) * (A_d - 1);
    Bu_d = (Bu/Ax) * (A_d - 1);
    v_k  = [Q_gen; Tc_in; T_amb];

    persistent x_last d_filt
    if isempty(x_last), x_last = T; d_filt = 0; end
    d_filt = 0.95*d_filt + 0.05*(T - x_last);

    X_free = zeros(p,1);  S = zeros(p,1);
    x = T;  s = 0;
    for i = 1:p
        x = A_d*x + B_d*v_k;   X_free(i) = x + d_filt;
        s = A_d*s + Bu_d;      S(i) = s;
    end

    T_activate = T_trg - 3.0;
    persistent ramp_ref
    if isempty(ramp_ref), ramp_ref = T_activate; end
    if T >= T_activate || ramp_ref > T_activate
        ramp_ref = min(ramp_ref + ramp_rate*Ts, T_trg);
    end
    R_traj = min(ramp_ref + ramp_rate*Ts*(1:p)', T_trg);

    E  = X_free - R_traj;
    dU = -(S'*E) / ((1 + beta) * (S'*S) + eps_reg(S));

    hi = min(mdot_max - mdot_prev, max_step);
    lo = min(mdot_prev - mdot_min, max_step);
    dU = max(min(dU, hi), -lo);

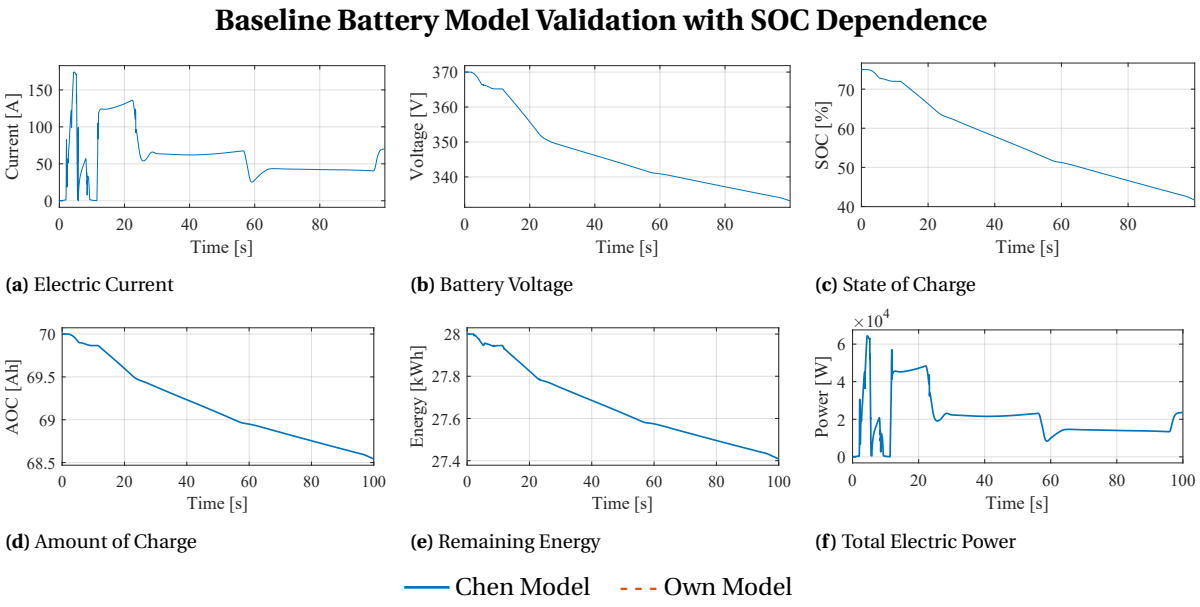
    mdot_cool = min(max(mdot_prev + dU, mdot_min), mdot_max);
    x_last = A_d*T + B_d*v_k + Bu_d*(mdot_cool - mdot_prev);
end

function r = eps_reg(S)
    r = 1e-12 * max(S'*S, 1);
end
```

A.2.3. Mechanical Energy Management Strategy Modes

0. **Transient Modes:** Manages the dynamic transitions between engine-off and engine-on states:
   - **EngineStart:** Cranks the ICE to idle speed using maximum starter motor load, while the EM maintains driver torque demand.
   - **EngineStop:** Opens the decoupling clutch and brakes the ICE to zero speed, while the EM maintains driver torque demand.
   - **EngineSync:** Matches ICE speed to driveline speed before closing the decoupling clutch to ensure smooth torque transfer.
1. **StartStop:** Corresponds to a standstill with the ICE off, where the target torques for the ICE and EM are zero.
2. **RegBrake:** Controls regenerative braking by assigning generator torques to the EM to recover braking energy and recharge the battery, mitigating energy loss due to friction braking. The strategy mode receives a target regenerative brake torque, $T_{\text{BrakeRegTarget}}$, and calculates the EM's target torque, T_{EMtarget}, accounting for the current transmission ratio from motor to wheel i_{M2W}:
$$T_{\text{EMtarget}} = -\frac{T_{\text{BrakeRegTarget}}}{i_{\text{M2W}}}$$
3. **RegDrag:** Controls regenerative drag, creating an artificial drag torque using the EM as a generator based on the negative torque demand interpreted from the pedal map. This recharges the power supply instead of dragging the ICE.
4. **ElecDrive:** Corresponds to pure electric driving, where the entire torque demand is satisfied by the EM while the ICE is disengaged by opening the clutch, setting the ICE target torque to zero.
5. **LoadShift:** Sets the ICE target torque to its optimum torque, T_{ICEopt}, which generates more energy than necessary so that the surplus energy is used for recharging the power supply by assigning an appropriate generator torque to the EM. The ICE is commanded to run at its optimum torque, converting excess mechanical energy into electrical energy by commanding the EM with a negative surplus torque:
$$T_{\text{ICE, target}} = T_{\text{ICE,opt}}, \qquad T_{\text{EM, target}} = T_{\text{target}} - T_{\text{ICE,opt}} < 0$$
6. **Assist:** Activated when the target torque is greater than the ICE optimum torque and smaller than its maximum torque. It sets the ICE target torque to its optimum torque, $T_{\text{ICE,opt}}$, and assigns the remaining demand to the EM:
$$T_{\text{ICE,target}} = T_{\text{ICE,opt}}, \qquad T_{\text{EM,target}} = T_{\text{target}} - T_{\text{ICE,opt}} > 0$$
7. **Boost:** Activated when the target torque is greater than the ICE maximum delivery torque at the current rotation speed. Boost serves as a primary deployment mechanism during acceleration phases where the ICE is commanded to maximum torque and the EM delivers the remaining demand:
$$T_{\text{ICE,target}} = T_{\text{ICE,max}}, \qquad T_{\text{EM,target}} = T_{\text{target}} - T_{\text{ICE,max}} > 0$$
8. **EngineDrive:** Corresponds to pure ICE driving, where the entire torque demand is assigned to the ICE and the EM target torque is zero.

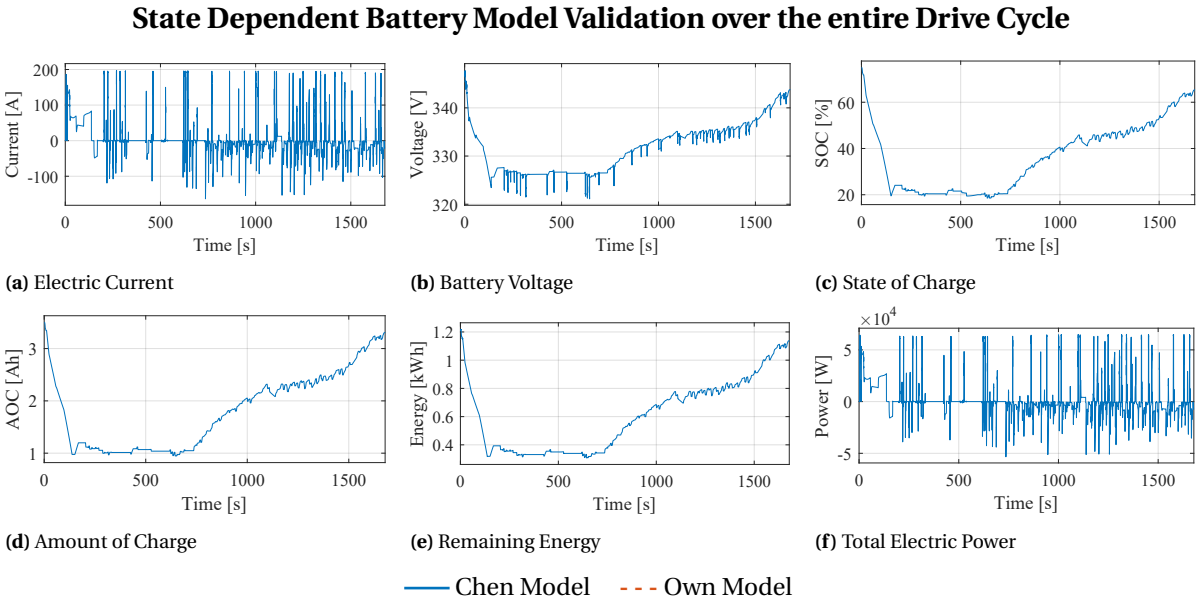
A.3. Chen Battery Model



(a) Electric Current **(b)** Battery Voltage **(c)** State of Charge

(d) Amount of Charge **(e)** Remaining Energy **(f)** Total Electric Power

Figure 4: Battery dynamic response of developed 2nd Order ECM with SOC dependence



(a) Electric Current **(b)** Battery Voltage **(c)** State of Charge

(d) Amount of Charge **(e)** Remaining Energy **(f)** Total Electric Power

Figure 5: Battery dynamic response of developed 2nd Order ECM with SOC dependence

Bibliography

[1] Weichao Zhuang, Shengbo Li (Eben), Xiaowu Zhang, Dongsuk Kum, Ziyou Song, Guodong Yin, and Fei Ju. A survey of powertrain configuration studies on hybrid electric vehicles. Applied Energy, 262: 114553, 2020. ISSN 0306-2619. doi: https://doi.org/10.1016/j.apenergy.2020.114553. URL https://www.sciencedirect.com/science/article/pii/S0306261920300659.

[2] How Lithium-ion Batteries Work, November 2006. URL https://electronics.howstuffworks.com/everyday-tech/lithium-ion-battery.htm.

[3] The Degradation Behavior of LiFePO4/C Batteries during Long-Term Calendar Aging | MDPI, n.d.. URL https://www.mdpi.com/1996-1073/14/6/1732.

[4] Achikkulath Prasanthi, Hussain Shareef, Rachid Errouissi, Ganesan V. Murugesu, and Madathodika Asna. Optimal Sizing and Dynamic Energy Source Characteristics of Hybrid Electric Vehicles: A Comprehensive Review and Future Directions. IEEE Access, 12:44695–44729, 2024. ISSN 2169-3536. doi: 10.1109/ACCESS.2024.3380464. URL https://ieeexplore.ieee.org/document/10477488/.

[5] Mohamed A. A. Mohamed, Tung Fai Yu, Grace Ramsden, James Marco, and Thomas Grandjean. Advancements in parameter estimation techniques for 1RC and 2RC equivalent circuit models of lithium-ion batteries: A comprehensive review. Journal of Energy Storage, 113:115581, March 2025. ISSN 2352-152X. doi: 10.1016/j.est.2025.115581. URL https://www.sciencedirect.com/science/article/pii/S2352152X25002944.

[6] Tedjani Mesbahi, Rocío Bendala Sugrañes, Reda Bakri, and Patrick Bartholomeüs. Coupled electro-thermal modeling of lithium-ion batteries for electric vehicle application. Journal of Energy Storage, 35: 102260, March 2021. ISSN 2352-152X. doi: 10.1016/j.est.2021.102260. URL https://www.sciencedirect.com/science/article/pii/S2352152X21000281.

[7] Mingzhang Pan, Dongliang Hu, Lu Liang, Wei Guan, Zhiqing Zhang, Nianye Ye, Haifeng Qin, and Xingjia Man. Coordinated thermal–energy management for battery energy storage systems in hybrid electric vehicles: Architecture, modeling, control strategies, and engineering validation. Journal of Energy Storage, 164:121939, July 2026. ISSN 2352-152X. doi: 10.1016/j.est.2026.121939. URL https://www.sciencedirect.com/science/article/pii/S2352152X26016038.

[8] Ramil Malikov, Pablo Iturralde, Kirill Karpukhin, Filipp Karpukhin, and Roman Zimov. Development of a Power Flow Management Strategy for a Hybrid Racing Car Aimed at Minimizing Lap Time. World Electric Vehicle Journal, 16(10):558, October 2025. ISSN 2032-6653. doi: 10.3390/wevj16100558. Num Pages: 18 Web of Science ID: WOS:001602285800001.

[9] Rushali R. Thakkar. (PDF) Electrical Equivalent Circuit Models of Lithium-ion Battery. In ResearchGate. IntechOpen, June 2026. doi: 10.5772/intechopen.99851. URL https://www.researchgate.net/publication/354617443_Electrical_Equivalent_Circuit_Models_of_Lithium-ion_Battery.

[10] Eway Energy. State of Health (SOH) in Lithium Batteries: Comprehensive Guide to Degradation & Estimation. March 2026. URL https://ewayenergy.com/state-of-health-soh-in-lithium-batteries-comprehensive-guide-to-degradation-estimation/. Section: Technical Blog.

[11] Manoj Mathew, Mehrdad Mastali, John Catton, Ehsan Samadani, Stefan Janhunen, and Michael Fowler. Development of an Electro-Thermal Model for Electric Vehicles Using a Design of Experiments Approach. Batteries, 4(2), 2018. ISSN 2313-0105. doi: 10.3390/batteries4020029. URL https://www.mdpi.com/2313-0105/4/2/29.

[12] Ming Li, Shiming Ma, Hui Jin, Rujin Wang, and Yan Jiang. Performance analysis of liquid cooling battery thermal management system in different cooling cases. Journal of Energy Storage, 72:108651, November 2023. ISSN 2352-152X. doi: 10.1016/j.est.2023.108651. URL https://www.sciencedirect.com/science/article/pii/S2352152X23020480.

[13] J. Jacob, J.A. Colin, H. Montemayor, D. Sepac, H.D. Trinh, S.F. Voorderhake, P. Zidkova, J.J.H. Paulides, A. Borisaljevic, and E.A. Lomonova. InMotion hybrid racecar: F1 performance with LeMans endurance. COMPEL - The International Journal for Computation and Mathematics in Electrical and Electronic Engineering, 34(1):210–233, 2015. ISSN 0332-1649. doi: 10.1108/COMPEL-11-2013-0344.

[14] Erik van den Eshof, Jorn van Kampen, and Mauro Salazar. Human-in-the-loop energy and thermal management for electric racing cars through optimization-based control. European Journal of Control, 86:101293, 11 2025. ISSN 0947-3580. doi: 10.1016/J.EJCON.2025.101293. URL https://www.sciencedirect.com/science/article/pii/S0947358025001220.

[15] Hatim Jbari, Rachid Askour, and Badr Bououlid Idrissi. Energy Management of Battery/Supercapacitor Electric Vehicle Considering Regenerative Braking Control. In 2022 IEEE 3rd International Conference on Electronics, Control, Optimization and Computer Science (ICECOCS), pages 1–8, December 2022. doi: 10.1109/ICECOCS55148.2022.9982885. URL https://ieeexplore.ieee.org/document/9982885/.

[16] Tong Liu, Lei Feng, Mikael Hellgren, and Jan Wikander. A Binary Controller to Ensure Engine Peak Efficiency for a Parallel Hybrid Electric Car. In 2019 IEEE Intelligent Transportation Systems Conference (ITSC), pages 726–732, October 2019. doi: 10.1109/ITSC.2019.8917315. URL https://ieeexplore.ieee.org/document/8917315/.

[17] Tong Liu, Lei Feng, and Wenyao Zhu. Fuel Minimization of a Hybrid Electric Racing Car by Quasi-Pontryagin's Minimum Principle. Ieee Transactions on Vehicular Technology, 70(6):5551–5564, June 2021. ISSN 0018-9545, 1939-9359. doi: 10.1109/TVT.2021.3075729. Num Pages: 14 Web of Science ID: WOS:000671544000030.

[18] Luca Paparusso, Manuel Riani, Fabio Ruggeri, and Francesco Braghin. Competitors-Aware Stochastic Lap Strategy Optimisation for Race Hybrid Vehicles. IEEE Transactions on Vehicular Technology, 72(3): 3074–3089, March 2023. ISSN 0018-9545, 1939-9359. doi: 10.1109/TVT.2022.3215171. Num Pages: 16 Web of Science ID: WOS:000965639600001.

[19] J. Jacob, J.A. Colin, H. Montemayor, D. Sepac, H.D. Trinh, S.F. Voorderhake, P. Zidkova, J.J.H. Paulides, A. Borisavljevic, and E.A. Lomonova. InMotion: Hybrid race car, beating F1 at LeMans. In Int. Conf. Exhib. Ecol. Veh. Renew. Energies, EVER, 2013. ISBN 978-1-4673-5270-3. doi: 10.1109/EVER.2013.6521638. Journal Abbreviation: Int. Conf. Exhib. Ecol. Veh. Renew. Energies, EVER.

[20] Zainab Asus, El-Hassane Aglzim, Daniela Chrenko, Zul-Hilmi Che Daud, and Luis Le Moyne. Dynamic

Modeling and Driving Cycle Prediction for a Racing Series Hybrid Car. IEEE Journal of Emerging and Selected Topics in Power Electronics, 2(3):541–551, September 2014. ISSN 2168-6777, 2168-6785. doi: 10.1109/JESTPE.2014.2307079. Num Pages: 11 Web of Science ID: WOS:000358607400021.

[21] G Zhuo and Y Gu. Optimization of parallel regenerative brake system control strategy and simulation analysis. In 2011 International Conference on Electrical and Control Engineering, pages 737–741, 2011. doi: 10.1109/ICECENG.2011.6057108.

[22] Harald Neudorfer. Comparison of three different electric powertrains for the use in high performance Electric Go-Kart. In 2007 International Aegean Conference on Electrical Machines and Power Electronics, pages 21–26, September 2007. doi: 10.1109/ACEMP.2007.4510478. URL https://ieeexplore.ieee.org/document/4510478/.

[23] Zainab Asus, Daniela Chrenko, El-Hassane Aglzim, Athmane Kebairi, Alan Keromnes, and Luis Le-Moyne. Model and Control Strategy Simulation of a Racing Series Hybrid Car. In 2014 IEEE Vehicle Power and Propulsion Conference (VPPC), pages 1–6, October 2014. doi: 10.1109/VPPC.2014.7007100. URL https://ieeexplore.ieee.org/document/7007100/. ISSN: 1938-8756.

[24] Luis D. Couto, Odile Capron, Jan Servotte, Raf Ponnette, and Grietus Mulder. Physics-based lifetime modeling and parameter identification of lithium-ion batteries under various degradation conditions. Journal of Energy Storage, 127:116739, August 2025. ISSN 2352-152X. doi: 10.1016/j.est.2025.116739. URL https://www.sciencedirect.com/science/article/pii/S2352152X25014525.

[25] Ferdinando Luigi Mapelli and Davide Tarsitano. Energy control for Plug-In HEV with ultracapacitors lithium-ion batteries storage system for FIA Alternative Energy Cup Race. In 2010 IEEE Vehicle Power and Propulsion Conference, pages 1–6, September 2010. doi: 10.1109/VPPC.2010.5729147. URL https://ieeexplore.ieee.org/abstract/document/5729147. ISSN: 1938-8756.

[26] Jose Roberto Boffino de A. Monteiro, Stefan Thiago Cury A. dos Santos, Mehrshad Pakjoo, Luca Perbellini, Luigi Piegari, and Rafael Souza Baquero. Comparison of Energy Management Strategies for an e-Racing Vehicle with Hybrid Energy Storage. In 2024 IEEE Vehicle Power and Propulsion Conference, Vppc 2024, New York, 2024. IEEE. ISBN 979-8-3315-4161-3 979-8-3315-4160-6. doi: 10.1109/VPPC63154.2024.10755226. Num Pages: 6 Series Title: IEEE Vehicle Power and Propulsion Conference Web of Science ID: WOS:001423189500012.

[27] Kailong Liu, T. R. Ashwin, Xiaosong Hu, Mattin Lucu, and W. Dhammika Widanage. An evaluation study of different modelling techniques for calendar ageing prediction of lithium-ion batteries. Renewable and Sustainable Energy Reviews, 131:110017, October 2020. ISSN 1364-0321. doi: 10.1016/j.rser.2020.110017. URL https://www.sciencedirect.com/science/article/pii/S1364032120303087.

[28] Haisheng Chen, Thang Ngoc Cong, Wei Yang, Chunqing Tan, Yongliang Li, and Yulong Ding. Progress in electrical energy storage system: A critical review. Progress in Natural Science, 19(3):291–312, March 2009. ISSN 1002-0071. doi: 10.1016/j.pnsc.2008.07.014. URL https://www.sciencedirect.com/science/article/pii/S100200710800381X.

[29] Giulio Barletta, Piera DiPrima, and Davide Papurello. Thévenin's Battery Model Parameter Estimation Based on Simulink. Energies, 15(17), August 2022. ISSN 1996-1073. doi: 10.3390/en15176207. URL https://www.mdpi.com/1996-1073/15/17/6207.

[30] Feng Li, Wei Zuo, Kun Zhou, Qingqing Li, Yuhan Huang, and Guangde Zhang. State-of-charge estimation

of lithium-ion battery based on second order resistor-capacitance circuit-PSO-TCN model. Energy, 289: 130025, February 2024. ISSN 0360-5442. doi: 10.1016/j.energy.2023.130025. URL https://www.sciencedirect.com/science/article/pii/S0360544223034199.

[31] Nadeem Ahmad Arif, Saad Mekhilef, Mehdi Seyedmahmoudian, and Alex Stojcevski. Degradation in Li-ion batteries and capacity decline under different cycling conditions: A comprehensive review. Journal of Energy Storage, 154:121270, April 2026. ISSN 2352-152X. doi: 10.1016/j.est.2026.121270. URL https://www.sciencedirect.com/science/article/pii/S2352152X26009345.

[32] Pavel Blažek, Ondřej Klvač, Martin Šedina, Ondřej Čech, Markéta Tkadlecová, Zuzana Stravová, Tomáš Kazda, Tomáš Zikmund, Robert H. Schmitt, and Jozef Kaiser. Comprehensive analysis of degradation mechanisms in 18650 Li-Ion cells under prolonged cycling conditions. Journal of Energy Storage, 130: 117436, September 2025. ISSN 2352-152X. doi: 10.1016/j.est.2025.117436. URL https://www.sciencedirect.com/science/article/pii/S2352152X25021498.

[33] Matthieu Dubarry, Cyril Truchot, and Bor Yann Liaw. Synthesize battery degradation modes via a diagnostic and prognostic model. Journal of Power Sources, 219:204–216, December 2012. ISSN 0378-7753. doi: 10.1016/j.jpowsour.2012.07.016. URL https://www.sciencedirect.com/science/article/pii/S0378775312011330.

[34] Gao Huaibin, Yang Jiangwei, Wei Meng, Ma Jianzhong, and Zhang Chuanwei. Dual time-scale state of charge estimation for lithium-ion batteries under temperature effects on the equivalent circuit model and available capacity. Ionics, 32:1759–1770, December 2025. doi: 10.1007/s11581-025-06897-8.

[35] Mostafa Abdelkhalek and İsmail Bayezit. Trajectory Planning for eVTOL with High-Fidelity HV Battery Modeling and SOC Estimation. In Proceedings of the Urban Air Mobility Conference, December 2024. URL https://www.researchgate.net/publication/391564332_Trajectory_Planning_for_eVTOL_with_High-Fidelity_HV_Battery_Modeling_and_SOC_Estimation.

[36] Christophe Forgez, Dinh Vinh Do, Guy Friedrich, Mathieu Morcrette, and Charles Delacourt. Thermal modeling of a cylindrical LiFePO4/graphite lithium-ion battery. Journal of Power Sources, 195(9):2961–2968, May 2010. doi: 10.1016/j.jpowsour.2009.10.105. URL https://utc.hal.science/hal-01999911.

[37] Yibo Qi, Wei Zhao, Xiaofeng Sun, Lei Qi, Donghui Wang, and Yuliang Zhang. State estimation of Li-ion batteries via improved second-order RC model. Energy Reports, 14:31–42, December 2025. ISSN 2352-4847. doi: 10.1016/j.egyr.2025.05.083. URL https://www.sciencedirect.com/science/article/pii/S2352484725003646.

[38] Lorenzo Breglio, Arcangelo Fiordellisi, Giovanni Gasperini, Giulio Iodice, Denise Palermo, Manuela Tufo, Fabio Ursumando, and Agostino Mele. A Model-Based Strategy for Active Balancing and SoC and SoH Estimations of an Automotive Battery Management System. Modelling, 5(3):911–935, August 2024. ISSN 2673-3951. doi: 10.3390/modelling5030048. URL https://www.mdpi.com/2673-3951/5/3/48.

[39] Xiaohua Zeng, Tong Liu, Dafeng Song, Nannan Yang, and Haoyong Cui. Extended Kalman filter–based and model predictive control–based dynamic coordinated control strategy for power-split hybrid electric bus. Proceedings of the Institution of Mechanical Engineers, Part D: Journal of Automobile Engineering, 234:095440701989175, December 2019. doi: 10.1177/0954407019891750.

[40] The MathWorks, Inc. Battery state-of-charge estimation, 2026. URL https://nl.mathworks.com/help/simscape-battery/ug/battery-state-of-charge-estimation.html. Accessed: August 2026.

[41] Sangjun Jeon, Jaewook Lee, and Seongmin Heo. Interpretable noninvasive framework for lithium-ion battery degradation diagnosis: Joint prediction of capacity and power fade and mechanism-aware health index classification. Applied Energy, 417:128036, August 2026. ISSN 0306-2619. doi: 10.1016/j.apenergy.2026.128036. URL https://www.sciencedirect.com/science/article/pii/S0306261926006884.

[42] Li Wang, Yujie Wang, Chang Liu, Duo Yang, and Zonghai Chen. A Power Distribution Strategy for Hybrid Energy Storage System Using Adaptive Model Predictive Control. IEEE Transactions on Power Electronics, 35(6):5897–5906, June 2020. ISSN 1941-0107. doi: 10.1109/TPEL.2019.2953050. URL https://ieeexplore.ieee.org/abstract/document/8896907.

[43] Luigi Mattia, Hamzeh Beiranvand, Walter Zamboni, and Marco Liserre. Lithium-ion battery thermal modelling and characterisation: A comprehensive review. Journal of Energy Storage, 129:117114, September 2025. ISSN 2352-152X. doi: 10.1016/j.est.2025.117114. URL https://www.sciencedirect.com/science/article/pii/S2352152X25018274.

[44] Zeyu Liu, Chengfeng Xiong, and Xiaofang Du. Research on the optimization control strategy of a battery thermal management system based on serpentine liquid cooling combined with phase change material. Journal of Power Sources, 630:236127, February 2025. ISSN 0378-7753. doi: 10.1016/j.jpowsour.2024.236127. URL https://www.sciencedirect.com/science/article/pii/S0378775324020809.

[45] Rong Guo, Ziyi Sun, and Maohui Luo. Energy-efficient battery thermal management strategy for range extended electric vehicles based on model predictive control and dynamic programming. Energy, 307:132769, October 2024. ISSN 0360-5442. doi: 10.1016/j.energy.2024.132769. URL https://www.sciencedirect.com/science/article/pii/S036054422402543X.

[46] Peng Qingfeng, Zhao han, Liu xinwen, Fang Yunzhou, and Zeng Xiangbing. Battery thermal management system design and control strategy study for hybrid electric vehicles. In 2014 IEEE Conference and Expo Transportation Electrification Asia-Pacific (ITEC Asia-Pacific), pages 1–4, August 2014. doi: 10.1109/ITEC-AP.2014.6941245. URL https://ieeexplore.ieee.org/document/6941245.

[47] Dittus-Boelter Correlation - an overview | ScienceDirect Topics, n.d.. URL https://www.sciencedirect.com/topics/engineering/dittus-boelter-correlation.

[48] Prashant Singh, Shashank Arora, Sai Santhosh Tota, Lauri Vänttinen, Ari Hentunen, and Mikko Pihlatie. Rule-Based Energy and Thermal Management Strategy for Hybrid Fuel cell-Battery System Powered Heavy Duty Vehicle. In 2025 IEEE Texas Power and Energy Conference (TPEC), pages 1–6, February 2025. doi: 10.1109/TPEC63981.2025.10907070. URL https://ieeexplore.ieee.org/document/10907070.

[49] Bo Feng, Ya Zhang, and Zichen Xu. Research on Thermal Management Control Methods Based on PID Algorithm. In 2024 7th International Conference on Mechatronics and Computer Technology Engineering (MCTE), pages 793–798, August 2024. doi: 10.1109/MCTE62870.2024.11117930. URL https://ieeexplore.ieee.org/document/11117930.

[50] Jorge Lopez-Sanz, Carlos Ocampo-Martinez, Jesus Alvarez-Florez, Manuel Moreno-Eguilaz, Rafael Ruiz-Mansilla, Julian Kalmus, Manuel Gräeber, and Gerhard Lux. Nonlinear Model Predictive Control for Thermal Management in Plug-in Hybrid Electric Vehicles. IEEE Transactions on Vehicular Technology, 66

(5):3632–3644, May 2017. ISSN 1939-9359. doi: 10.1109/TVT.2016.2597242. URL https://ieeexplore.ieee.org/document/7529090.

[51] Seho Park and Changsun Ahn. Computationally Efficient Stochastic Model Predictive Controller for Battery Thermal Management of Electric Vehicle. IEEE Transactions on Vehicular Technology, 69(8): 8407–8419, August 2020. ISSN 1939-9359. doi: 10.1109/TVT.2020.2999939. URL https://ieeexplore.ieee.org/document/9108617.

[52] Rui Wang and Srdjan M. Lukic. Dynamic programming technique in hybrid electric vehicle optimization. In 2012 IEEE International Electric Vehicle Conference, pages 1–8, March 2012. doi: 10.1109/IEVC.2012.6183284. URL https://ieeexplore.ieee.org/document/6183284.

[53] Chinta srikiran. Model Predictive Control and Adaptive Algorithms for Optimizing Battery Thermal Management and State Estimation in Electric Vehicles. Innovative Research Thoughts, 9:191–198, June 2023. doi: 10.36676/irt.v9.i3.1644.

[54] Fei Feng, Sangli Teng, Kailong Liu, Jiale Xie, Yi Xie, Bo Liu, and Kexin Li. Co-estimation of lithium-ion battery state of charge and state of temperature based on a hybrid electrochemical-thermal-neural-network model. Journal of Power Sources, 455:227935, April 2020. doi: 10.1016/j.jpowsour.2020.227935.

[55] IPG Automotive. CarMaker Manual. IPG Automotive GmbH, 2024. Version 12.0.

[56] Min Chen and G.A. Rincon-Mora. Accurate electrical battery model capable of predicting runtime and i-v performance. IEEE Transactions on Energy Conversion, 21(2):504–511, 2006. doi: 10.1109/TEC.2006.874229.

[57] The MathWorks, Inc. Battery state-of-charge estimation. MATLAB & Simulink Example Documentation, 2026. URL https://www.mathworks.com/help/sps/ref/battery-state-of-charge-estimation.html. Accessed: 2026.

[58] DOWTHERM™ SR-1 Heat Transfer Fluid, Dyed, n.d.. URL https://www.dow.com/en-us/pdp.dowtherm-sr-1-heat-transfer-fluid-dyed.25630z.html.

[59] Marcelo M. Morato, Julio E. Normey-Rico, and Olivier Sename. Model predictive control design for linear parameter varying systems: A survey. Annual Reviews in Control, 49:64–80, January 2020. ISSN 1367-5788. doi: 10.1016/j.arcontrol.2020.04.016. URL https://www.sciencedirect.com/science/article/pii/S1367578820300250.